



Publication Year	2015
Acceptance in OA @INAF	2020-05-15T14:03:18Z
Title	A Review of General Physical and Chemical Processes Related to Plasma Sources and Losses for Solar System Magnetospheres
Authors	Seki, K.; Nagy, A.; Jackman, C. M.; Crary, F.; Fontaine, D.; et al.
DOI	10.1007/s11214-015-0170-y
Handle	http://hdl.handle.net/20.500.12386/24879
Journal	SPACE SCIENCE REVIEWS
Number	192

1 Title:

2 A review of general physical and chemical processes related to
3 plasma sources and losses for solar system magnetospheres

4
5 Authors:

6 K. Seki¹, A. Nagy², C. M. Jackman³, F. Crary⁴, D. Fontaine⁵, P. Zarka⁶, P. Wurz⁷, A.
7 Milillo⁸, J. A. Slavin², D. C. Delcourt⁵, M. Wiltberger⁹, R. Ilie², X. Jia², S. A. Ledvina¹⁰,
8 M. W. Liemohn², and R. W. Schunk¹¹.

9
10 *Affiliations:*

- 11 1. *Solar-Terrestrial Environment Laboratory, Nagoya University, Nagoya, Aichi 464-*
12 *8601, Japan.*
- 13 2. *Department of Atmospheric, Oceanic and Space Sciences, University of Michigan,*
14 *Ann Arbor, MI 48109, USA.*
- 15 3. *Department of Physics and Astronomy, University of Southampton, Southampton,*
16 *SO17 1BJ, UK.*
- 17 4. *Laboratory for Atmospheric and Space Physics, University of Colorado, Boulder, CO,*
18 *80303, USA.*
- 19 5. *Laboratoire de Physique des Plasmas (CNRS-EP-UPMC-UPSud), Ecole*
20 *Polytechnique, F-91128 Palaiseau Cedex, France.*
- 21 6. *LESIA, Observatoire de Paris, CNRS, UPMC, Université Paris-Diderot, 5 place Jules*
22 *Janssen, 92195 Meudon, France.*
- 23 7. *Physics Institute, University of Bern, Sidlerstrasse 5, 3012 Bern, Switzerland.*
- 24 8. *Institute of Space Astrophysics and Planetology, INAF, Rome, Italy.*
- 25 9. *High Altitude Observatory, National Center for Atmospheric Research, Boulder, CO*
26 *80212, USA.*
- 27 10. *Space Sciences Lab., University of California, Berkeley, CA 94720, USA.*
- 28 11. *Center for Atmospheric and Space Sciences, Utah State University, 4405 Old Main*
29 *Hill, Logan, UT 84322, USA.*

30
31 **Abstract:**

32 The aim of this paper is to provide a review of general processes related to plasma
33 sources, their transport, energization, and losses in the planetary magnetospheres. We
34 provide background information as well as the most up-to-date knowledge of the
35 comparative studies of planetary magnetospheres, with a focus on the plasma supply to
36 each region of the magnetospheres. This review also includes the basic equations and
37 modeling methods commonly used to simulate the plasma sources of the planetary
38 magnetospheres. In this paper, we will describe basic and common processes related to
39 plasma supply to each region of the planetary magnetospheres in our solar system. First,
40 we will describe source processes in Section 1. Then the transport and energization
41 processes to supply those source plasmas to various regions of the magnetosphere are
42 described in Section 2. Loss processes are also important to understand the plasma

43 population in the magnetosphere and Section 3 is dedicated to the explanation of the loss
44 processes. In Section 4, we also briefly summarize the basic equations and modeling
45 methods with a focus on plasma supply processes for planetary magnetospheres.

46

47

48

49

50 **1. Sources**

51 There are three possible sources of plasma for a planetary magnetosphere. The first one
 52 is the surface of solid bodies (planet and/or its satellites), the second one is the planetary
 53 (or satellite in the unique case of Titan) atmosphere/ionosphere, if any, and the third
 54 source is the plasma from the solar atmosphere, i.e., the solar wind. In this section, we
 55 will review processes related to each the source, i.e., surface in Subsection 1.1,
 56 ionosphere in 1.2, and solar wind in 1.3.

57

58 **1.1. Surface**

59 In this subsection, we will review source and loss processes related to the planetary
 60 or satellite surface as illustrated in Figure 1. Topics to be explained include the ion-
 61 induced sputtering, chemical sputtering, photon stimulated desorption, micro-meteoroid
 62 impact vaporisation, adsorption by surface, ion-sputtering and radiolysis in the icy
 63 surface, sputter yields from water ice, binding energies, sticking and bouncing, and
 64 energy distributions.

65 a) *Ion-induced sputtering*

66 The impact of energetic ions or neutrals (typically of keV/nucleon energies) onto a
 67 solid surface causes the removal of atoms, ions and molecules from the top surface. This
 68 process is referred to in the literature as sputtering, in particular nuclear sputtering when
 69 nuclear interaction between the impacting ion and the surface atoms cause the particle
 70 release, or electronic sputtering when the electronic interaction results in particle release,
 71 as discussed below for icy surfaces. Sputtering is a well-studied phenomenon in material
 72 science (e.g. *Behrisch and Eckstein, 2007*).

73 The energy distribution for particles sputtered from a solid, $f(E_e)$, with the energy
 74 E_e of the sputtered particle, has originally been given by Sigmund (1969) and adapted for
 75 planetary science (*Wurz and Lammer, 2003; Wurz et al., 2007*)

$$76 \quad f(E_e) = \frac{6E_b}{3 - 8\sqrt{E_b/E_c}} \frac{E_e}{(E_e + E_b)^3} \left\{ 1 - \sqrt{\frac{E_e + E_b}{E_c}} \right\} \quad (1)$$

77 where E_b is the surface binding energy of the sputtered particle, typically in the eV range,
 78 and E_c is the cut-off energy. The cut-off energy E_c , which is the maximum energy that
 79 can be imparted to a sputtered particle by a projectile particle with energy E_i , is given by

the limit imposed by a binary collision between a projectile atom or ion, with mass m_1 and the target atom, with mass m_2 (to be sputtered) as

$$E_c = E_i \frac{4m_1m_2}{(m_1 + m_2)^2} \quad (2)$$

An example of energy distributions based on Equation (1) is shown in Figure 2.

The energy imparted to the sputtered atoms and molecules is significant with respect to typical escape energies from planetary objects and a considerable fraction of the sputtered particles do not return to the planetary surface (Wurz *et al.*, 2007, 2010).

The polar angle distribution of sputtered atoms is generally described by a $\cos^k(\varphi_e)$ law (Hofer, 1991), where the exponent k , is usually between 1 and 2, and depends on the structure of the surface and φ_e is the ejection angle relative to the normal. For the rough surfaces typically encountered in planetary application $k = 1$ is usually chosen (Cassidy and Johnson, 2005; Wurz *et al.*, 2007).

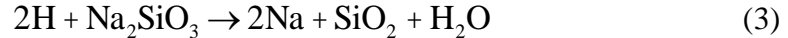
The sputter yield is the average number of atoms or molecules removed from the solid surface per incident particle. Ion sputtering releases all species from the surface into space reproducing more or less the local surface composition on an atomic level. Preferential sputtering of the different elements of a compound will lead to a surface enrichment of those elements with low sputtering yields in the top-most atomic layers. However, the steady-state composition of the flux of sputtered atoms will reflect the average bulk composition. Thus, particle sputtering, when operative, will give us compositional information about the refractory elements of the bulk surface.

Sputter yields for the different species can be obtained using the TRIM.SP simulation software (Biersack and Eckstein, 1984; Ziegler, 1984; Ziegler, 2004); see also the recent review on computer simulation of sputtering by Eckstein and Urbassek (2007). TRIM, like many other simulation programmes for sputtering, assumes that the collisions between atoms can be approximated by elastic binary collisions described by an interaction potential. The energy loss to electrons is handled separately as an inelastic energy loss. For typical rock (regolith) surface compositions, the total sputter yield, i.e., all species sputtered from the surface taken together, is about 0.12 atoms per incoming solar wind ion at 400 km s^{-1} , considering protons and alpha particles only (Wurz *et al.*, 2007). This sputter yield is the integral over all emission angles and all energies of sputtered particles. The 5% alpha particles in the solar wind contribute about 30% to the

sputter yield. Heavier ions in the solar wind do not contribute to the sputtering because of their low abundance in the solar wind (Wurz *et al.*, 2007). CMEs can cause increased sputtering of surface material, because their ion density can be much larger than that of the regular solar wind. In addition, alpha particles are often more abundant in the CME plasma, which increases the sputter yield even more.

b) *Chemical sputtering*

When a surface is bombarded with chemically reactive species, chemical alterations in the surface material have to be considered. Chemical reactions between the rock (or regolith grain) and the surface and impacting ions may form species, which are more loosely bound to the surface and thus more easily sputtered. This causes an increase of the sputtering yield or allows for some other release from the surface. This process is usually referred to as chemical sputtering in the literature. In the context of planetary science Potter (1995) considered chemical sputtering for the first time to explain the Na exosphere on Mercury. When a solar wind proton hits the mineral surface processes like the following



may occur that liberate the Na from the mineral compound. If this happens on the surface, or the liberated Na migrates to the surface, the liberated Na can be released from the surface also by thermal desorption or photon stimulated desorption. This process was successfully implemented in a 3D model to explain the three dimensional structure of the Na exosphere of Mercury with very good agreement with observations for the spatial distribution and the density (Mura *et al.*, 2009).

c) *Photon stimulated desorption*

Photon-stimulated desorption (PSD), sometimes also referred to as photon sputtering, is the removal of an atom or molecule by an ultraviolet photon absorbed at the surface, via an electronic excitation process at the surface. PSD is highly species selective, and works efficiently for the release of Na and K from mineral surfaces. Also water molecules are removed from water ice very efficiently via PSD. PSD is considered the major contributor for the Na and K exospheres of Mercury and the Moon (Killen *et al.*, 2007; Wurz *et al.*, 2010). Since PSD releases only Na and K from the mineral matrix it is

not very important for the overall erosion of the surface since it will cease once the surface is void of Na and K. The situation is different for PSD of water for an icy object, where the PSD process can remove the major surface species.

The flux of material removed by PSD, F_i^{PSD} , of a species i from the surface can be calculated by the convolution of the solar UV photon flux spectrum, $F_{ph}(\lambda)$, with the wavelength-dependent PSD-cross section, $Q_i(\lambda)$,

$$F_i^{\text{PSD}} = f_i N_s \int F_{ph}(\lambda) Q_i(\lambda) d\lambda \quad (4)$$

where N_s is the surface atom density, and f_i is the species fraction on the grain surface. Equation (4) can be approximated as

$$F_i^{\text{PSD}} \approx \frac{1}{4} f_i N_s F_{ph} Q_i \quad (5)$$

where the factor 1/4 gives the surface-averaged value. The experimentally determined PSD-cross section for Na is $Q_{Na} = (1-3) \cdot 10^{-20} \text{ cm}^2$ in the wavelength range of 400 – 250 nm (*Yakshinskiy and Madey, 1999*) and for K the PSD-cross section is $Q_K = (0.19-1.4) \cdot 10^{-20} \text{ cm}^2$ in the same wavelength range (*Yakshinskiy and Madey, 2001*). Equation (4) can also be written in terms of the PSD yield, Y_i^{PSD} , per incoming photon

$$F_i^{\text{PSD}} = \frac{1}{4} f_i F_{ph} Y_i^{\text{PSD}} \quad (6)$$

which has been determined for water by *Westley et al. (1995)* in the laboratory. The PSD-yield of water is found to be temperature dependent

$$Y_{H_2O}^{\text{PSD}} = Y_0 + Y_1 \exp\left(-\frac{E_{\text{PSD}}}{k_B T}\right) \quad (7)$$

with $Y_0 = 0.0035 \pm 0.002$, $Y_1 = 0.13 \pm 0.10$, $E_{\text{PSD}} = (29 \pm 6) \cdot 10^{-3} \text{ eV}$, and k_B is the Boltzmann constant (*Westley et al., 1995*). The temperature dependence is very similar to the one for sputtering of ice (see below), which was found later.

d) *Micro-meteoroid impact vaporisation*

The impact of micro-meteorites on a planetary surface will volatilise a certain volume of the solid surface, which contributes to the exospheric gas at the impact site. At Mercury, for example, about one to two orders of magnitude more material than the impactor is released because of the high impact speed for meteorites (*Cintala, 1992*).

The ratio of the maximum ejecta velocity to the primary impact velocity decreases with increasing impact speed. The measured temperature in the micro-meteorite produced vapour cloud is in the range of 2500 – 5000 K. *Eichhorn* (1978a, 1978b) studied the velocities of impact ejecta during hypervelocity primary impacts and found that the velocity of the ejecta increases with increasing impact velocity and with decreasing ejection angle, with the ejection angle measured with respect to the plane of the target surface. Such ejecta temperatures are significantly higher than typical dayside surface temperatures, but the corresponding characteristic energies are still lower than for particles that result from surface sputtering. In general, the simulated gaseous material from micro-meteorite vaporisation assumes a thermal distribution (e.g. *Wurz and Lammer*, 2003), i.e., a Maxwellian-like energy distribution with an average gas temperature of about 4000 K. For a rocky planetary object in the solar wind the contributions to the exosphere from ion sputtering and from micro-meteorite impact are about the same (*Wurz et al.*, 2007, 2010).

Most of the meteorites falling onto a planetary object are very small, see for example *Bruno et al.* (2007) for the Moon and *Müller et al.* (2002) for Mercury. Micro-meteorite bombardment can be regarded as a continuous flux of small bodies onto the surface, and thus as a steady contribution to the exosphere. However, occasionally larger meteorites may fall onto a surface causing a much larger release of particles into the exosphere. Such a scenario was studied for Mercury by *Mangano et al.* (2007). They found that for a meteorite of 0.1 m radius an increase in the exospheric density by a factor 10 – 100, depending on species, for about an hour over the density from sputtering should be observed.

e) *Adsorption by surface*

Most of the material released from the surface falls back onto it. Depending on the species, the surface, and the surface temperature the particle may stick or may bounce back into the exosphere. Metal atoms, chemical radicals and similar species will stick to the surface because they become chemically bound, i.e., their sticking coefficient is $S = 1$. For example a sputtered oxygen atom will stick, i.e, will form a chemical bond with the atom it lands on. Similarly, metal atoms will bind chemically to the surface site they land on. Exception are the alkali metals, where Na and K are observed often in exospheres, and which are transiently adsorbed on mineral surfaces. The probability adsorption

(sticking) on silicate surface was measured Yakshinskiy and Madey (2005) as function of the surface temperature. For sodium they found $S_{\text{Na}}(100 \text{ K}) = 1.0$, $S_{\text{Na}}(250 \text{ K}) = 0.5$ and $S_{\text{Na}}(500 \text{ K}) = 0.2$, and for potassium they found $S_{\text{K}}(100 \text{ K}) = 1.0$ and $S_{\text{K}}(500 \text{ K}) = 0.9$.

Non-reactive chemical compounds will only stick to the surface when they freeze onto it, which is important mostly for icy moons and planetary objects further out in the solar system. For example O_2 will not freeze onto the surfaces of the icy moons of Jupiter, thus remain in the atmosphere after they have been released from the surface. The same is true for noble gases.

f) *Ion-sputtering and radiolysis in the icy surface*

In the outer solar system it is quite common to encounter icy moons embedded in the planetary magnetosphere, hence, subjected to ion bombardment. The ion impacts onto a water-icy surface can cause sputtering, ionization and excitation of water-ice molecules. Following electronic excitations and ionization water-ice molecules can get dissociated; chemical reactions among the water-dissociation products result in the formation of new molecules (e.g. O_2 , H_2 , OH and minor species) that are finally ejected from the surface to the moon's exosphere in a two-phase process (e.g., *Johnson*, 1990).

g) *Sputter yields from water ice*

These processes have been extensively studied and simulated in laboratory (e.g., *Johnson*, 1990, 2001; *Baragiola et al.*, 2003). The energy deposited to a solid by the impacting ion, called stopping power, has two components: electronic excitation of molecules predominant at higher energies and momentum transfer collisions (elastic sputtering) predominant at lower energies (*Sigmund*, 1969; *Johnson et al.*, 2009). *Famà et al.* (2008) obtained through laboratory data fitting the total sputter yields (i.e., number of neutrals released after the surface impact of one ion) for different incident ions at different energies. They discriminated the contributions due to the two components that produce the release of H_2O (direct ion sputtering) and of O_2 and H_2 (electronic sputtering and radiolysis). The total sputter yield Y depends on the type, j , and energy, E_j , of the impacting ion and the surface temperature, T , and it can be written in the following form:

$$Y_{\text{total}}^j(E_j, T) = Y_{\text{H}_2\text{O}}^j(E_j) + Y_{\text{diss}}^j(E_j, T) \quad (8)$$

where $Y_{\text{H}_2\text{O}}^j(E_j)$ is the sputtering yield of the H_2O molecules, given by:

$$Y_{H_2O}^j(E) = 1/U_o \cdot \left(\frac{3}{4\pi^2 C_0} a S_n^j(E) + \eta (S_e^j(E))^2 \right) \cos^{-f}(\vartheta) \quad (9)$$

where $U_o = 0.45 \text{ eV}$ is the surface sublimation energy, C_0 is the constant of the differential cross section $d\sigma$ for elastic scattering in the binary collision approximation (Sigmund, 1969), a is an energy-independent function of the ratio between the mass of the target molecules and of the projectile (Andersen and Bay, 1981), S_n^j is the nuclear stopping cross section, S_e^j is the electronic stopping cross section, η is a factor that gives the proportionality between electronic sputtering and $(S_e^j(E))^2/U_o$, θ is the incidence angle, and f is an exponent of the angular dependence of the yield (Famà et al., 2008).

$Y_{diss}^j(E_j, T)$ in Equation (8) is the yield associated to the loss of O_2 and H_2 , produced on ice after its irradiation by energetic ions, given by :

$$Y_{diss}^j(E, T) = 1/U_o \cdot \left(\frac{3}{4\pi^2 C_0} a S_n^j(E) + \eta (S_e^j(E))^2 \right) \frac{Y_1}{Y_0} e^{-\frac{E_a}{k_B T(lat, \varphi)}} \cos^{-f}(\vartheta) \quad (10)$$

where Y_1 and Y_0 are fitting parameters obtained by laboratory data elaboration (see Famà et al., 2008). Only this second term is temperature dependent. Laboratory measurements have shown that H_2O molecules dominate the total release yield at lower temperatures ($<120 \text{ K}$) and O_2 and H_2 at higher ($>120 \text{ K}$) temperatures (Johnson, 2001).

Since H_2 is eventually lost from ice stoichiometrically, and since the measurements used by Famà et al. (2008) referred to water-equivalent molecules, the total yield for the O_2 ejection can be expressed as follows:

$$Y_{O_2}^j = [m_{H_2O}/(m_{O_2} + 2m_{H_2})] \cdot Y_{diss}^j(E_j, T) = 0.5 \cdot Y_{diss}^j(E_j, T) \quad (11)$$

where m_{H_2O} , m_{O_2} and m_{H_2} are the molecular masses of a water, oxygen and hydrogen, respectively (Plainaki et al., 2014). The total number, N_i , of the released molecules of type i depends on the product of the energy spectrum of the ion fluxes impacting the surface with the energy dependent yield:

$$N_i = \int_E \sum_j dF^j/dE_j \cdot Y_i^j dE_j \quad (12)$$

Some example of laboratory measured sputtering yields (see website <http://people.virginia.edu/~rej/h2o.html>) as a function of energy and impact ion species are shown in Figure 3 together with the Famà et al. (2008) function (blue) and the Johnson et al. (2009) function (red).

The yields obtained by laboratory simulations could be different (lower or higher) in

the planetary environments since the aggregation status and the purity of the surface material could be different from the sample. Also important is the radiative history of the ice, in fact, the irradiation enhances the sputter yield (*Teolis et al.*, 2005)

h) *Binding energies, sticking and bouncing*

The kinetic energy of a water molecule ejected from the surface is affected mainly by the surface binding energy and secondarily by the energy or mass of the impacting ion (*Johnson*, 1990; 1998). Although the sublimation energy of H₂O is 0.45 eV/molecule, the sputtered particle energy distributions for molecular ices tend to have maxima at lower energies than a collision cascade prediction with surface binding energy equal to the normal sublimation energy (*Brown and Johnson*, 1986; *Boring et al.*, 1984; *Brown et al.*, 1984; *Haring et al.*, 1984). Several explanations for this phenomenon have been proposed; the surface may be strongly disrupted with many atoms or molecules leaving at once without experiencing the same binding energy as a single atom leaving a planar surface (*Roosendaal et al.*, 1982; *Reimann et al.*, 1984). In addition, the surface region may be electronically and collisionally excited and the interatomic or intermolecular forces are lower as a result of that excitation (*Reimann et al.*, 1984). The assumption of an ‘effective’ binding energy for the H₂O molecules equal to $E_b = 0.054$ eV, which was experimentally obtained in the past (*Boring et al.*, 1984, *Haring et al.*, 1984) seems appropriate.

The H₂O and the O₂ molecules released from the surface are set up to ballistic trajectories until they either return to the surface of the body or they escape. Upon return to the surface, the H₂O molecules stick, while the O₂ molecules get thermalized and bounce back to continue their ballistic travel until electron-impact (see next section) ionizes them (*Plainaki et al.*, 2012; 2013). The average kinetic energy that the O₂ molecules have after impacting the surface is about $k_B T$, where k_B is the Boltzmann constant and T is the surface temperature.

i) *Energy distributions*

The emitted O₂ molecules have a complex energy distribution consisting of two components. The distribution of the O₂ molecules that escape the gravity of an icy moon (e.g., Ganymede) is assumed to be described by an empirical function (*Johnson et al.*,

1983; *Brown et al.*, 1984) used also in earlier modelling (*Plainaki et al.*, 2012; 2013; *Cassidy et al.*, 2007, *Shematovich et al.*, 2005):

$$\frac{dF}{dE_e} = a_n E_{O_2} / (E_e + E_{O_2})^2 \quad (13)$$

where $E_{O_2} = 0.015 \text{ eV}$ (*Shematovich et al.*, 2005), a_n is the normalization factor and E_e is the energy of the ejected O_2 molecules.

The O_2 molecules that have had at least one contact with the surface form a Maxwellian velocity distribution function with a temperature equal to the surface temperature. On the basis of the above, the overall energy distribution of the exospheric O_2 can be considered to be mainly thermal exhibiting however the high energy tail in Equation (13) (*De Vries et al.*, 1984).

The energy distribution of the sputtered water molecules is similar to the regolith ion sputtering distribution, given by Sigmund (1969) as discussed in (Equation (1)). The major difference to sputtering of rock is that the ‘effective’ binding energy, E_b , is equal to 0.054 eV (*Johnson et al.*, 2002). The binding energy E_b influences significantly the energy spectrum at low energies, while the high energy tail of the distribution is affected mainly by $E_c(E_i)$ (see Equation (2)).

Finally, since the energetic and heavy ions of giant planets’ magnetospheres can produce a release of up to 1000 water molecules per impacting ion after the interaction with the icy moon surfaces (see Figure 3), the ion sputtering process is often a major contributor to the exosphere population for the outer solar system moons, where surface temperatures are generally around 80–150 K and the solar illumination is low. The spatial distributions of the exospheres are expected to depend mainly on the illumination of the moon's surface, which determines the moon’s surface temperature responsible for the efficiency of radiolysis (*Famà et al.*, 2008). At these low temperatures, in fact, the averaged expected contribution of sublimated water-ice to the moon’s exospheric density is important only locally, i.e., at small altitudes above the subsolar point (*Smyth and Marconi*, 2006; *Marconi*, 2007; *Plainaki et al.*, 2010). The high rate of release of particles at relatively high energy, produce a net escape from the moon and high surface erosion rates; for example, the erosion rate of the icy moons embedded in the Jupiter magnetospheric plasma radiation is estimated in the range of $0.01\text{--}0.1 \text{ } \mu\text{m}$ per year (*Cooper et al.*, 2001; *Paranicas et al.*, 2002). Usually, H_2 formed in ice diffuses and escapes much more efficiently than O_2 at the relevant temperatures in the outer solar

system, and, in turn, escapes from the icy moons because of their relatively weak gravitational fields (*Cassidy et al.*, 2010). Therefore, the irradiation of icy surfaces can preferentially populate the magnetosphere with hydrogen (*Lagg et al.*, 2003; *Mauk et al.*, 2003), leaving behind an oxygen-rich satellite surface (e.g., *Johnson et al.*, 2009).

1.2. Ionosphere

a) Ionization processes

Solar extreme ultraviolet (EUV) radiation and particle, mostly electron, precipitation are the two major sources of energy input and ionization in solar system ionospheres (for details see *Schunk and Nagy*, 2009). Relatively long wavelength photons (> 90 nm) generally cause dissociation, while shorter wavelengths cause ionization; the exact distribution of these different outcomes depends on the relevant cross sections and the atmospheric species.

Radiative transfer calculations of the solar EUV energy deposition into the thermospheres are relatively simple, because absorption is the only dominant process. Taking into account the fact that the incoming photon flux and absorption cross sections depend on the wavelength and the different absorbing neutral species have different altitude variations, the decrease in the intensity of the incoming flux after it travels an incremental distance ds_λ is:

$$d\mathcal{I}(z, \lambda, \chi) = - \sum_s n_s(z) \sigma_s^a(\lambda) \mathcal{I}(z, \lambda) ds_\lambda \quad (14)$$

where $\mathcal{I}(z, \lambda, \chi)$ is the intensity of the solar photon flux at wavelength λ and altitude z , $n_s(z)$ is the number density of the absorbing neutral gas, s , $\sigma_s^a(\lambda)$ is the wavelength dependent absorption cross section of species s and ds_λ is the incremental path length in the direction of the flux. Integration of Equation (14) leads to the following expression for the solar flux as a function of altitude and wavelength:

$$\mathcal{I}(z, \lambda, \chi) = \mathcal{I}_\infty(\lambda) \exp \left[- \int_\infty^z \sum_s n_s(z) \sigma_s^a(\lambda) ds_\lambda \right] \quad (15)$$

where, $\mathcal{I}_\infty(\lambda)$ is the flux at the top of the atmosphere and the integration is to be carried out along the optical path. The argument of the exponential in Equation (15) is defined as the optical depth sometimes also called optical thickness, t , thus:

358

$$359 \quad t(z, l, c) = \int_0^z \hat{\sigma}_s n_s(z) S_s^a(l) ds_l \quad (16)$$

360 and thus Equation (15) can be written as:

$$361 \quad \mathcal{I}(z, \lambda, \chi) = \mathcal{I}_\infty(\lambda) \exp[-\tau(z, \lambda, \chi)] \quad (17)$$

362 Once the ionizing solar photon flux is known, the photoionization rate for a given ion
363 species $P_s(z, c)$ can be written as:

$$364 \quad P_s(z, \chi) = n_s(z) \int_0^{\lambda_z} \mathcal{I}_\infty(\lambda) \exp[-\tau(z, \lambda, \chi)] \sigma_s^i(\lambda) d\lambda \quad (18)$$

365 where λ_{si} is the ionization wavelength threshold and $S_s^i(l)$ is the wavelength dependent
366 ionization cross section for species s. Figure 4 shows an example of the production rate
367 calculated for Saturn.

368

369 b) *Electron transport*

370 The transport calculations for electrons in an atmosphere are more difficult than those
371 for EUV radiation because scattering and local sources play an important role. In a
372 collisionless plasma the motion of charged particles in a magnetic field can be considered
373 to consist of a combination of a gyrating motion around the field line and the motion of
374 the instantaneous center of this gyration called the guiding center. When the radius of
375 gyration is small compared to the characteristic dimensions of the field line (the case in
376 many ionospheres), one can just concentrate on the motion of the guiding center.
377 Furthermore in most ionospheric applications steady state condition can be assumed; if
378 one further neglects the presence of external electric fields and the divergence of the
379 magnetic field, the equation for the electron flux F simplifies down to:

$$380 \quad \alpha \frac{\partial \Phi}{\partial x} = \sqrt{\frac{m}{2\varepsilon}} \frac{\delta \Phi}{\delta t} \quad (19)$$

381 where α is the pitch angle with respect to the magnetic field, r the distance along the
382 field line, m_e is the mass of the electron, ϵ is the energy of the electron and $\frac{dF}{dt}$ denotes
383 collision induced changes in the flux. This equation is usually solved by dividing the flux
384 into a number of equal angular components or streams. The so called two stream

approach is the most commonly used approach and it has been shown, using Monte Carlo calculations (Solomon, 1993), that given all the uncertainties associated with differential scattering cross sections, it is generally sufficient to consider only two streams.

Once the electron flux is established, as a function of altitude, the electron impact ionization rate P_s of ion species, s , is given by the following relation:

$$P_s(z) = n_s(z) \int_{e_{sl}}^{\infty} F(z, e) S_s^i(e) de \quad (20)$$

where e_{sl} is the ionization energy threshold for species s .

The transport of superthermal ions and neutral gas particles is even more complicated than that of electrons because additional processes, such as charge exchange and ionization are involved. Recent approaches to obtain 3D values of these ion and/or neutral fluxes have used the so-called direct simulation Monte Carlo (DSMC) method (Bird, 1994). This approach is well suited to address this problem and as increasing computing resources become available good, comprehensive and accurate solutions are becoming available. Here again once the ion/neutral fluxes are obtained, the impact ionization rate can be directly calculated using an equation analogous to Equation (20) above.

c) *Loss processes and ion chemistry*

The area of science concerned with the study of chemical reactions is known as chemical kinetics. A chemical reaction in which the phase of the reactants does not change is called a homogeneous reaction and in the solar system upper atmospheres and ionospheres these reactions dominate. Dissociative recombination of O_2^+ with an electron is a typical, so called stoichiometric, reaction:



Reactions that can proceed in both directions are called reversible. Charge exchange between an ion and parent atom and accidentally resonant charge exchange between H and O are such reactions:

416

417



418

419



420

421 The reactions indicated by Equations (21), (22), and (23) are called elementary
 422 reactions, because the products are formed directly from the reactants. O^+ , for example
 423 can recombine with an electron directly, via radiative recombination, but this process is
 424 very slow. In most cases atomic ions recombine via a multi-step process. Two examples
 425 of such recombination, via multiple-step processes, are:

426

427

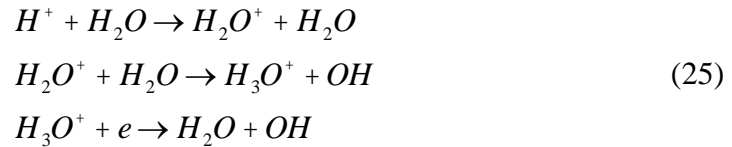


428

and:

429

430



431

432 The two-step process indicated in Equation (24) is important in the terrestrial E-region,
 433 and the multi-step one indicated by Equation (25) is very important in the ionospheres of
 434 Jupiter and Saturn.

435 Given the typical thermospheric and ionospheric temperatures the only chemical
 436 reactions likely to occur are the so-called exothermic ones. These are reactions that result
 437 in zero or positive energy release. Thus, for example, the reaction of H^+ in the
 438 ionospheres of Saturn or Jupiter does not take place with ground state H_2 , because the
 439 ionization potential of H_2 is larger than that of H. However, if H_2 is in a vibrational state
 440 of 4 or higher, the reaction becomes exothermic and can proceed. This is potentially very
 441 important in the ionospheres of Jupiter and Saturn (*McElroy, 1973; Majeed and*
 442 *McConnell, 1996*). Similarly, in the terrestrial thermosphere the reaction between ground
 443 state N and O_2 is very slow, because of the high activation energy that is needed, but the
 444 reaction with the excited atomic nitrogen, in the 2D state is rapid and important. For
 445 concrete values for chemical reaction reference data can be found in literature (e.g.,

Schunk and Nagy, 1980; Nagy et al., 1980; Anicich, 1993; Fox and Sung, 2001; Schunk and Nagy, 2009; Terada et al., 2009).

d) *Ionospheric outflows*

When a planet has a global intrinsic field, the ions originating in the ionosphere can escape to space from high-latitude regions such as the cusp/cleft, auroral zone, and polar cap. It is observationally known that ions of ionospheric origin can be one of the most important sources of the plasma in the terrestrial magnetosphere especially in the near-Earth regions (see *Chappell*, 2015 for more details). The outflowing ions along the magnetic field can be categorized into several types of ion outflows, i.e., the polar wind, bulk ion upflow, ion conics, and beams. Detailed reviews of observational aspects and theories of ionospheric outflows can be found in the literature (e.g., *Yau and Andre*, 1997; *Andre and Yau*, 1997; *Moore and Horwitz*, 2007; *Chappell*, 2015). Here we briefly summarize important types of ionospheric ion outflows from a magnetized planet or satellite with atmosphere. A good schematic illustration of these outflows can be found in Figure 1 of *Moore and Horwitz* (2007).

c.i) Polar wind

The polar wind refers to low-energy ion outflows along the open magnetic field lines in the polar ionosphere, mainly caused by an ambipolar electric field formed by the separation of ions and electrons. To achieve charge neutrality with the lighter and faster upflowing electrons, ambient ions are accelerated by the ambipolar electric field. The polar wind has larger flux in the dayside region, where the outflowing photoelectrons can contribute to the ambipolar electric field. However, the controlling factor of the polar wind outflow rate is still under debate (e.g., *Kitamura et al.*, 2012). A variety of modeling efforts have been made for the polar wind (e.g., *Banks and Holzer*, 1969; *Ganguli*, 1996; *Schunk and Sojka*, 1997; *Tam et al.*, 2007). Observations showed a large flux of O⁺ polar wind, which was not expected by classical theories (e.g., *Abe et al.*, 1996, *Yau et al.*, 2007). Possible additional acceleration mechanisms include the mirror force, pressure gradient, and centrifugal acceleration by plasma convection in the curved magnetic field. The acceleration mechanisms of the polar wind ions can be ubiquitous in the ionospheres of magnetized planets or satellites.

479 c.ii) Bulk ion upflow

480 The bulk ion upflows refer to the upward ion flow in the low-altitude ionosphere
481 around the F region, which is observed in the auroral zone and cusp (e.g., *Ogawa et al.*,
482 2008). The bulk ion upflows do not significantly contribute to the outflow flux from the
483 ionosphere, since their energy is usually less than 1eV and well below the escape energy
484 of heavy ions such as O^+ , O_2^+ , and NO^+ . On the other hand, they are considered important
485 to transport these heavy ions to the high-altitude ionosphere to enable them to undergo
486 additional acceleration in the auroral region and cusp. The mechanisms that cause the
487 bulk ion upflow include the electron heating driven by soft electron precipitation, Joule
488 heating of ions, and frictional ion heating.

489
490 c.iii) Ion conics

491 Ion conics are named after the typical shape of the velocity distribution function of
492 ion outflows caused by transverse acceleration in terms of the local magnetic field. The
493 transverse ion heating with typical energies from thermal to a few keV are often seen in
494 the cusp region and the auroral zone. The resultant heated ions are called TAIs (TAIs
495 (transversely accelerated ions). They are often accompanied by electron precipitation,
496 electron density depletions, and a variety of different resonant waves, such as lower
497 hybrid (LH) waves or broadband extremely low frequency (BBELF) waves (*Norqvist et*
498 *al.*, 1996; *Frederick-Frost et al.*, 2007). Once the ions are heated transversely to the
499 magnetic field, the mirror force can accelerate them further upward by conserving kinetic
500 energy. Thus the resultant ion velocity distribution functions at high altitudes show
501 conical shapes. Various types of ion conics have been observed in the terrestrial
502 ionosphere (e.g., *Øieroset et al.*, 1999). This same process can occur and create ion
503 conics, when there is an energy input, such as electron precipitation, into a planetary
504 ionosphere under an open magnetic field line geometry.

505
506 c.iv) Ion beam

507 It has been observationally shown that there exist parallel electric fields in the auroral
508 region in both the upward and downward current regions. Their significance for auroral
509 acceleration had been widely discussed (e.g., *Mozer et al.*, 1977; *McFadden et al.*, 1999).
510 The formation of parallel electric field has been also studied theoretically (e.g., *Brown et*
511 *al.*, 1995; *Wu et al.*, 2002). The static electric potential drop typically up to several kV

accelerates electrons downward and cause discrete auroras. The same parallel electric field can accelerate ions upward. The resultant ion outflows become mostly field-aligned energetic beams. It is suggested that a distributed field-aligned potential drop produced self-consistently from a balance between magnetospheric hot ion and electron populations, soft electron precipitations, and transverse heating of ionospheric ions. When the magnetospheric population has significant differential anisotropy between the ion distribution and the electron distribution, significant parallel potential drops can develop (*Wu et al.*, 2002).

1.3. Solar wind

In addition to the sources detailed above, the solar wind can act as a plasma source for magnetospheres. The character of the solar wind changes significantly with increasing radial distance from the Sun, and this, combined with the contrasting obstacles presented by various planetary magnetospheres, leads to a large variation in solar wind-magnetosphere dynamics and in the degree to which the solar wind can act as a plasma source for a given magnetosphere. The electron density, flow speed, and magnetic field strength in the solar wind near the orbit of the Earth are known to be about 7 cm^{-3} , 450 km/s, and 7 nT, respectively. The solar wind mostly consists of protons, while it contains about 3-4 % of He^{2+} .

It is well known that interplanetary magnetic field (IMF) lines become increasingly tightly wound with distance from the Sun, as modelled by Parker (1958). The average angle that the interplanetary field lines make with respect to the radial direction increases from $\sim 20^\circ$ at Mercury's orbital distance of $\sim 0.4 \text{ AU}$ (*Kabin et al.*, 2000) through $\sim 45^\circ$ at Earth (*Thomas and Smith*, 1980), $\sim 80^\circ$ at Jupiter (*Forsyth et al.*, 1996) to $\sim 83^\circ$ at Saturn's orbital distance of $\sim 9.5 \text{ AU}$ (*Jackman et al.*, 2008). The IMF strength also changes with radial distance, with the strength of the B_R component decreasing approximately as r^{-2} . For example, the IMF at Mercury is much stronger than at Saturn (*Burlaga*, 2001), and this has implications for solar wind-magnetosphere coupling.

The form of interaction between the solar wind and magnetosphere changes with the IMF orientation depending on whether the IMF has a parallel or anti-parallel component to the planetary magnetic field at the subsolar magnetopause. The parallel (anti-parallel) case corresponds to the northward (southward) IMF condition at Earth and vice versa at Jupiter and Saturn where the planetary dipoles are oppositely directed to Earth. In

addition to magnetic reconnection between the planetary field and IMF, other important physical processes in terms of the solar wind entry into the magnetosphere include the magnetic reconnection, anomalous diffusion across the magnetopause caused by the Kelvin-Helmholtz instability (KHI), and kinetic Alfvén waves.

a) *Magnetic reconnection*

The solar wind is thought to enter planetary magnetospheres primarily through magnetic reconnection at the magnetopause (Dungey, 1961). Reconnection at the magnetopause accelerates and directs a mixture of magnetosheath and magnetospheric plasma along newly opened magnetic flux tubes down into the cusp (see review by Paschmann, 2013). The anti-sunward flow in the magnetosheath carries these open flux tubes downstream where they are assimilated into the lobes of the magnetotail (Caan *et al.*, 1977). Much of the plasma injected down into the cusp mirrors and flows upward into the high latitude magnetotail to form the plasma mantle (Rosenbauer *et al.*, 1975; Pilip and Morfill, 1978). The plasma in this region then $\mathbf{E} \times \mathbf{B}$ drifts down into the equatorial plasma sheet. In this manner magnetic reconnection between the IMF and planetary magnetic field transfers mass, energy and momentum from the solar wind into the magnetosphere. This dayside reconnection at the Earth (Gosling *et al.*, 1990; McAndrews *et al.*, 2008) is illustrated schematically in Figure 5.

The rate of magnetopause reconnection is modulated strongly by the magnitude and orientation of the IMF relative to the planetary field and plasma conditions in the magnetosheath adjacent to the magnetopause. More specifically, low-latitude reconnection at Earth's magnetopause is strongly controlled by the magnetic shear angle across the magnetopause with the highest rates being observed for the largest shear angles when the interplanetary magnetic field (IMF) has a strong southward component (Sonnerup, 1974; Fuselier and Lewis, 2011). This is called the “half-wave rectifier effect” (Burton *et al.*, 1975). The ultimate reason that reconnection at Earth requires large shear angles, ~ 90 to 270° , is the high average Alfvénic Mach number at 1 AU, i.e., $\sim 6 - 8$ (Slavin *et al.*, 1984). These high Mach numbers result in a high- β magnetosheath and, generally, thin, weak plasma depletion layers (PDLs) adjacent to the magnetopause (Zwan and Wolf, 1976). The typically high- β magnetosheaths at the Earth and the outer planets cause the magnetic fields on either side of the magnetopause to differ largely in magnitude. Under these circumstances, reconnection is only possible for large shear

angles, typically larger than 90° (Sonnerup, 1974). In contrast, the presence of a strong PDL in the inner magnetosheath naturally leads to magnetic fields of similar magnitude on either side of the magnetopause. For low- β magnetosheaths and well developed PDLs observed at Mercury (Gershman *et al.*, 2013a), the near equality of the magnetic field on either side of the magnetopause will allow reconnection to occur for arbitrarily low shear angles (DiBraccio *et al.*, 2013; Slavin *et al.*, 2014) such as observed, for example, across heliospheric current sheets where the magnetic fields are also nearly equal on both sides (Gosling *et al.*, 2005; Phan *et al.*, 2005).

At Earth an extensive literature exists describing the empirical relationships between the upstream solar wind and IMF (e.g. Perreault and Akasofu, 1978; Bargatze *et al.*, 1984; Burton *et al.*, 1976). These relationships are all based upon the general formula to calculate the magnetopause reconnection voltage which is:

$$F = v_{sw} B_{perp} L \quad (26)$$

where v_{sw} is the solar wind velocity, B_{perp} is the magnitude of the perpendicular component of the IMF (such that $V_{sw}B_{perp}$ is the motional solar wind electric field), and L is the width of the solar wind channel perpendicular to B_{perp} , in which the IMF can reconnect with closed planetary field lines.

The length, L , depends in some way on the properties of the interplanetary medium, and is most frequently taken as some function of the “clock angle” of the IMF. Studies have shown that while dayside reconnection (at Earth) is certainly much weaker for northward than for southward IMF, it does not switch off entirely until the clock angle falls below $\sim 30^\circ$ (Sandholt *et al.*, 1998; Grocott *et al.*, 2003). Such empirical functions to quantify the rate of dayside reconnection have in turn been applied at Saturn (Jackman *et al.*, 2004) and Jupiter (Nichols *et al.*, 2006) and integrated over time to estimate the amount of flux opened through reconnection at the dayside.

In recent years, the debate about what determines the reconnection rate at the dayside has intensified, in part due to the wealth of spacecraft data at planets such as Mercury, Jupiter and Saturn, which all represent vastly different parameter spaces and thus are likely to differ from the terrestrial magnetosphere in terms of their level of solar wind-magnetosphere coupling (Slavin *et al.*, 2014). A comprehensive study by Borovsky *et al.* (2008) for Earth found that the reconnection rate is controlled by four local plasma parameters: B_s (the magnetic field strength in the magnetosheath), B_m (the magnetic field

strength in the magnetosphere), ρ_s (the plasma mass density in the magnetosheath), and ρ_m (the plasma mass density in the magnetosphere).

Scurry and Russell (1991) argued that dayside reconnection at the outer planets should have a negligible influence as it would be impeded by the high Mach number regimes there. This argument was countered by the observations of McAndrews et al. (2008) for Saturn and Grocott et al. (2009) for Earth. Subsequently Lai et al. (2012) interpreted a lack of observation of FTEs at Saturn as lack of reconnection. Most recently, Masters et al., (2012) proposed that the plasma beta conditions adjacent to Saturn's magnetopause can restrict the regions over which reconnection can operate. By way of contrast, reconnection at Mercury's dayside has been found to be much more intense than Earth, is independent of the magnetic field shear angle, and varies inversely with magnetosheath plasma β (DiBraccio et al., 2013). Furthermore, large flux transfer events, relative to Mercury's small magnetosphere, occur at Mercury's magnetopause with typical frequencies of 1 every 8 to 10 s (Slavin et al., 2012b; Imber et al., 2014).

MESSENGER observations at Mercury have found that the rate of magnetic reconnection at the dayside magnetopause is on average three times larger than at Earth (Slavin et al., 2009; DiBraccio et al., 2013). A schematic illustration of Mercury's magnetosphere based on MESSENGER observations can be found in Figure 1 of Slavin et al. (2009). Further, the rate of reconnection at the magnetopause appears independent of IMF direction with high reconnection rates being measured even for small shear angles (DiBraccio et al., 2013; Slavin et al., 2014). These results at Mercury regarding the relationship between low upstream M_A , plasma- β , magnetic shear angle, and reconnection rate parallel the recent developments regarding PDL formation under low M_A (Farrugia et al., 1995) and reconnection as a function of plasma- β (Phan et al., 2013) at Earth. At Earth the typically high- β magnetosheath limits fast reconnection to IMF orientations that have a southward component, i.e. magnetic shear angles across the magnetopause larger than 90° (i.e. the half-wave rectifier effect). However, during encounters with coronal mass ejections at Earth, the upstream M_A approaches values typical of what is seen at Mercury and similar effects are seen; i.e. low-beta magnetosheaths and high reconnection rates even for small magnetic shears across the magnetopause (Lavraud et al., 2013).

b) *Kelvin-Helmholtz instability (KHI)*

Another important mechanism of plasma entry from the solar wind to the magnetosphere is anomalous diffusion across the magnetopause at low latitudes, i.e., around the equatorial plane. The solar wind plasma needs to be transported in the direction perpendicular to the local magnetic field to realize the diffusion. It is observationally known that the flank plasma sheet of Earth's magnetosphere becomes colder and denser than usual during prolonged periods of northward IMF (e.g., *Terasawa et al.*, 1997; *Borovsky et al.*, 1998). One mechanism to cause the anomalous diffusion can be represented by the Kelvin-Helmholtz instability (KHI), which is driven by a flow shear between the magnetosheath (shocked solar wind) and the magnetosphere. KHI itself is basically an MHD instability, while the non-linear evolution of KHI vortex can facilitate the cross field diffusion and the mixing of the solar wind and magnetospheric plasmas inside the rolled-up vortex.

A number of mechanisms have been proposed that would cause the plasma mixing inside the vortex. One of the candidate mechanisms is magnetic reconnection inside the vortex triggered by vortex roll-up in the presence of finite in-plane component of the magnetic field (e.g., *Nykyri and Otto*, 2001; *Nakamura et al.*, 2008). Once the magnetosheath and magnetospheric field lines are reconnected, the detached plasma from the solar wind can be transported inside the magnetosphere. Another idea to realize the mixing is turbulent transport of solar wind plasma across the field line for the inhomogeneous density case of KHI (e.g., *Matsumoto and Hoshino*, 2006). When the density gradient between the magnetosheath and magnetosphere sides is large, the secondary instability is excited at the density interface inside the vortex and the laminar flow is changed to turbulence. The secondary instability is a kind of Rayleigh-Taylor instability (RTI) where the centrifugal force by the rotation motion inside the vortex acts as a gravitational force in the regular RTI. Development of the secondary instability creates a thin, winding, and elongated interface of the solar wind and magnetospheric plasmas. PIC simulation results show that the turbulent electrostatic fields excited by the secondary RTI facilitate an efficient mixing of collisionless plasmas across the field lines. **Figure 6a** and **Figure 6b** show an example of such an elongated mixing interface for electrons and ions, respectively (adopted from *Matsumoto and Seki*, 2010).

These proposed nonlinear theories of KHI provide plausible mechanisms for solar wind transport across the magnetopause. On one hand, a remaining problem has been to

explain the cold dense plasma sheet formation with KHI. Another question has been how to form a broad mixing layer of several Earth radii observed at Earth (*Wing and Newell, 2002*), since the proposed mixing is basically limited inside the vortex whose size is expected to be much smaller if one considers a simple KHI vortex without nonlinear vortex pairing. Based on large-scale MHD and PIC simulations, *Matsumoto and Seki (2010)* showed that rapid formation of a broad plasma turbulent layer can be achieved by forward and inverse energy cascades of the KHI. **Figure 6** shows an example of the full particle simulations. The forward cascade is triggered by growth of the secondary Rayleigh-Taylor instability excited during the nonlinear evolution of the KHI, while the inverse cascade is accomplished by nonlinear mode couplings between the fastest growing mode of the KHI and other KH unstable modes. As a result of the energy transport by the inverse cascade, the growth rate of the largest vortex allowed in the system reaches a value of 3.7 times greater than that of the linear growth rate and it can create the boundary layer extended over several Earth radii (**Figure 6c**).

The KHI is also considered important in Saturn's magnetosphere (e.g., *Masters et al., 2009; 2010; Delamere et al., 2013*). Given that the corotating flows in the magnetosphere have the opposite (same) directions compared to the shocked solar wind flow in the dawn (dusk) side dayside magnetopause, the occurrence of KHI is expected to be highly asymmetrical, i.e., the dawn side magnetopause has a favorable condition to KHI excitation. Observations of kilometric radiation suggested that the KHI at Saturn's magnetopause tends to occur in the morning sector (*Galopeau et al., 1995*). Based on the 3-D MHD simulations, *Fukazawa et al. (2007a)* show that the KHI vortex is more pronounced for the northward IMF case than the southward case. However, the effects of KHI on the plasma mixing and transport in Saturn's magnetosphere are still far from understood.

2. Transport and energization of plasma

There are a number of methods by which plasma can be transported and energized within magnetospheres. We refer the reader to *Jackman et al. (2014a)* for a comprehensive review of transport and loss processes in the magnetospheres of Mercury, Earth, Jupiter and Saturn. In this section we describe major transport and energization

processes which are important to understand how to populate various parts of planetary magnetospheres.

2.1. Axford/Hines cycle

A key transport mechanism, thought to be at work in slowly-rotating magnetospheres, is the so-called viscous interaction driven model (Axford and Hines, 1961; Axford, 1964). This involves momentum transfer from the solar wind to the magnetotail via quasi-viscous interaction, particularly at the low-latitude magnetopause. It is illustrated schematically in Figure 7. This cycle can drive circulation within a closed magnetosphere, provided an appropriate tangential-drag mechanism exists. A major mechanism to enable this interaction is the Kelvin-Helmholtz instability described in subsection 2.1.3, driven by flow shear at the magnetopause, which may also be coupled with magnetic reconnection (e.g. Hasegawa *et al.*, 2004; Nykyri *et al.*, 2006).

2.2. Dungey cycle

A second transport mechanism driven by solar wind interaction is the Dungey cycle. In this cycle, dayside reconnection opens magnetic flux, and the solar wind interaction carries these open magnetic field lines from dayside to nightside, where they are stretched out to form the tail lobes (defined here as the open field line region, while noting that centrifugal confinement of plasma to the equator in rapidly rotating systems can alter this picture somewhat (e.g. Hill and Michel, 1976; Ray *et al.*, 2009)). As they are stretched out down-tail, open field lines sink in towards the center plane of the tail, where they reconnect again, closing the flux that was opened on the dayside. The “Dungey cycle timescale” refers to the length of time from the opening of the field lines at the dayside to the closing of the field lines on the nightside. Figure 8 shows the stages involved in the Dungey cycle for the case of Earth, where the timescale is ~1 hour (Cowley, 1982). The Dungey cycle is also known to operate strongly in the slowly rotating magnetosphere of Mercury, with a timescale of just ~1-2 minutes (Siscoe *et al.*, 1975; Slavin *et al.*, 2012a). The relative importance of the Dungey cycle at the rapidly rotating magnetospheres of Jupiter and Saturn is a topic of some debate. Badman and Cowley (2007) estimated that when active, the Dungey cycle timescale at Jupiter is of order several weeks, whereas at

Saturn the timescale is ~ 1 week or more (*Jackman et al.*, 2004). Figure 9 illustrates the combination of the Dungey and viscous-cycle flows in the Earth's ionosphere.

2.3. Rotational Driven Transport and Vasyliunas cycle

The role of rotation in a planetary magnetosphere may be estimated by considering the superposition of dawn-dusk electric field resulting from the solar wind flow and the radial electric field imposed by the planetary ionosphere (*Brice and Ioannidis*, 1970). The resulting potential is

$$\Phi = -\eta v_{sw} B_{sw} r \sin j - \frac{\Omega B_0 R^3}{r} \quad (27)$$

where v_{sw} and B_{sw} are the solar wind speed and magnetic field, η the efficiency with which the solar wind field penetrates into the magnetosphere, and B_0 , R and Ω the planetary equatorial magnetic field, radius and rotation rate. This implies that the plasma will $\mathbf{E} \times \mathbf{B}$ drift along closed paths and in the sense of planetary rotation within a distance

$$r_0 = \sqrt{\frac{\Omega B_0 R^3}{\eta v_{sw} B_{sw}}} \quad (28)$$

For the Earth, this approximation suggests a corotating region inside of $4 R_E$, reasonably consistent with the observed size of the Earth's plasmasphere. For Jupiter and Saturn, however, the same calculation suggests a size of over 150 and 50 planetary radii, respectively. This would be larger than the actual size of these planetary magnetospheres. In practice, the observed corotating region occupies most, but not all, of these planetary magnetospheres. Nor are the flows at a rigid corotation speed. At Jupiter they begin to depart from corotation somewhere near the orbit of Europa ($10 R_J$) (*McNutt et al.*, 1979; *Krupp et al.*, 2002) and at Saturn the flows are 10-20% of full corotation as close to the planet as $4 R_S$ (*Wilson et al.*, 2009). An example of application of Equation (27) to Jupiter's case can be found in Figure 5 of *Delamere and Bagenal* (2010).

This corotational flow results in a dramatically different distribution of plasma along magnetic field lines and allows internal plasma sources to drive magnetospheric dynamics. The distribution of plasma along a magnetic field line is determined by the gravitational, centrifugal and ambipolar electric potentials (*Siscoe*, 1977; *Bagenal and Sullivan*, 1981)

$$n_a = n_{a,0} \exp \left(- \frac{U(l) + q_a F(l)}{kT_a} \right) \quad (29)$$

$$U(l) = - \frac{GMm_a}{LR \cos^2 l} + \frac{m_a}{2} \omega^2 L^2 R^2 \cos^6 l$$

and the requirement of charge neutrality $\sum q_\alpha n_\alpha = 0$. The above equations assume a dipole magnetic field and isotropic Maxwellian velocity distributions, but can be appropriately modified to treat any magnetic field geometry, as well as non-Maxwellian distributions (e.g. anisotropic Maxwellians (*Huang and Birmingham, 1992*), kappa distributions (*Meyer-Vernet, et al., 1995*), etc.)

When we consider the electric potential inside the synchronous orbit:

$$\left(\frac{2GM}{3\omega^2} \right)^{1/3} = \left(\frac{2}{3} \right)^{1/3} R_{sync} \quad (30)$$

where R_{sync} is the radius of synchronous orbit, the potential has a maximum at the equator. Outside this distance, there is a potential minimum at the equator and a local maximum at a latitude:

$$\cos^8 l = \frac{2}{3} \frac{R_{sync}^3}{LR} \quad (31)$$

As a result, ions produced in the equatorial magnetosphere and inside this “critical distance” will freely precipitate into the planetary atmosphere, while those produced farther from the planet are equatorially trapped. In the case of the Earth, the critical distance would be 5.75 R_E . Since this is outside the corotating plasmasphere, no such equatorial trapping occurs in the Earth’s magnetosphere. In contrast, trapping may occur outside 1.96 R_J at Jupiter and 1.62 R_S at Saturn. Thus, the plasma in virtually all of these magnetospheres is equatorially trapped. This “critical distance” has also been identified as a limit for stable orbits of charged dust particles, in the limit $m/q \rightarrow 0$ (*Northrop and Hill, 1982*) and in simulations of ions produced over Saturn’s ring plane (*Luhmann et al., 2006*).

In addition to allowing equatorial trapping, the mid-latitude potential minimum also results in a minimum in electron density. While the exact location of this minimum depends on the ambipolar field, and therefore on the abundance and temperature of the various species, calculations using typical, observed values place it close to the latitude given in Equation (31). At these latitudes, due to their lower mass, protons are expected

to be the most abundant species even though they are not at the equator. An increase in proton abundance with latitude has been observed by the Cassini spacecraft at Saturn (Thomsen *et al.*, 2010), but no clear minimum has been reported, probably due to the very low densities present at these latitudes. At Jupiter, protons represent only a few percent of the equatorial ions and mass-resolved observations are unavailable.

This mid-latitude density minimum and the predominance of protons have strong implications for magnetosphere-ionosphere coupling. The dynamical processes of the low-latitude magnetosphere are connected to the planetary ionosphere through field-aligned currents. These currents are limited by the availability of charge carriers and are therefore sensitive to the electron density profile along a field line. By finding solutions to a one-dimensional Vlasov equation, Ray *et al.* (2009) showed that the current-voltage relation along a Jovian field line differs significantly from the traditional Knight relation (Knight, 1973) (see Equations (39) and (40)). The saturation current may be one to two orders of magnitude lower and depends on the conditions at the electron density minimum rather than the equator. Other aspects of magnetosphere-ionosphere coupling are mediated by MHD waves. Wave velocities and propagation times are sensitive to the plasma properties along the field lines. As a result, many aspects of magnetosphere-ionosphere coupling at Jupiter and Saturn depend on the poorly measured mid-latitude plasma.

In the presence of equatorial trapping, any plasma sources in the magnetosphere must be balanced by some loss process. In the case of Jupiter and Saturn, plasma is produced by the ionization of neutrals from satellites (primarily Io and Enceladus), rings and the planetary exospheres. Recombination is not an efficient loss process, and charge exchange does not result in a net removal of ions. The main loss process balancing these plasma sources is centrifugally-driven, radial transport. The corotating plasma experiences an outward, centrifugal force. To first order, this is balanced by magnetic tension. Field lines are stretched under the condition:

$$\frac{1}{m_0} \left(\vec{\nabla} \times \vec{B} \right) \times \vec{B} = r \omega^2 \vec{r}. \quad (32)$$

This result in a current sheet which resembles that of the Earth's magnetotail in some ways, but which is present at all local times. The stretching of the field lines can be roughly approximated by

$$\frac{B_r}{B_z} \sim \frac{H}{r} \frac{\Omega^2 r^2}{2V_A^2} \quad (33)$$

where V_A is the Alfvén speed, H the thickness of the current sheet and B_r the radial field immediately above or below the sheet.

This balance of centrifugal force and magnetic tension is unstable. The situation is analogous to the magnetized Rayleigh-Taylor instability, where a denser fluid is above a less dense one. In this case, the centrifugal force replaces gravity, and radial transport is driven by a denser plasma inside a less dense plasma (*Krupp*, 2004 and references therein). Time scales for this instability are of order the rotation period of the planet, but may be partially stabilized by considerations such as the Coriolis force and coupling to the ionosphere (*Pontius*, 1997).

In the inner and middle magnetosphere, interchange appears to be the key method by which mass can be transported within magnetospheres. It is a process whereby cool, dense plasma can move outward, to be replaced by hotter, more tenuous plasma moving inward, resulting in a net outward transport of mass. This has been observed both at Jupiter (*Thorne et al.*, 1997; *Kivelson et al.*, 1997; *Krupp et al.*, 2004 and references therein) and Saturn (*Hill et al.*, 2005; *Burch et al.*, 2005). The phenomena are less well-measured at Jupiter, since their typical duration there is shorter and below the 80-s time resolution of the Galileo plasma instrument in almost all cases. Typically, the inward-moving flux tubes are characterized by an abrupt increase in magnetic pressure, the disappearance of thermal plasma, and the presence of a hot, energetic particle population. In the case of older (or more inward transported flux tube) events, flux tubes may contain a mixture of low energy plasma diffusing in and energetic particles curvature-gradient drifting out. Much older events are surrounded by a time-dispersed signature in keV and higher energy particles. This is a result of the superposition of the corotating flow and the particles' curvature-gradient drift (in the direction of corotation for ions and opposite it for electrons). The corresponding outward motion of cold, dense plasma has not been reported.

For the rapidly rotating magnetospheres of the outer planets with their large moon-derived plasma sources, the “planetary wind” or “Vasyliunas cycle” is of critical importance (*Hill et al.*, 1974; *Michel and Sturrock*, 1974; *Vasyliunas*, 1983). This Vasyliunas cycle is driven not by the solar wind, but by the energy transferred to internally generated plasma by the fast rotation of these planets. The plasma created deep

inside the magnetosphere is accelerated by magnetic stresses from the ionosphere, gains energy, and moves outward from the planet. Centrifugal forces cause the field lines to stretch. These stretched field lines can form a thin current sheet, across which the closed field lines reconnect. This reconnection simultaneously shortens the field line and (like the Dungey cycle), releases plasma down the tail in the form of a “plasmoid”. The stages of this cycle, as viewed in an inertial frame of reference, are illustrated in Figure 10, the picture originally put forward by Vasyliunas (1983).

2.4. Field-aligned potential drop

Many efforts in theories, simulations and observations showed the role played by magnetic-field-aligned electric fields at different locations in the Heliosphere. Significant insights of field-aligned processes, such as particle acceleration, parallel electric fields and currents and their relationships come from numerous observations in the terrestrial magnetosphere at different altitudes along magnetic field lines during the last 50 years. To give examples among others, a few missions that contributed to this field after some of the pioneering spacecraft have flown (see the review by Mozer et al., 1980) are listed hereafter. The long-term US program “Defense Meteorological Satellite Program” (DMSP) maintains satellites orbiting at low altitude (830 km) since 1971. In the decades 1980-2000, the Swedish missions VIKING, FREJA and the NASA mission “Fast Auroral Snapshot Explorer” (FAST) were designed to achieve measurements with excellent time and space resolutions at mid-altitudes (from about 400 to 4000 km altitude). The ESA multi-spacecraft pioneering mission CLUSTER has been exploring all latitudes and longitudes between typically 4 and 20 Earth radii since 2000 over a time period of more than 15 years. The signatures identified in the terrestrial case provide guidelines to interpret observations in other magnetospheres.

In planetary magnetospheres, where plasmas are collisionless in most regions, the mobility of electrons along magnetic field lines is very high as compared to perpendicular motions mostly driven by large-scale electric fields, magnetic or pressure gradients. Therefore, this high field-aligned mobility contributes to cancel out any potential drop that would appear along magnetic field lines. However, from the mid-70s, observations revealed a secondary peak in the energy spectrum of precipitating electrons in the terrestrial auroral region. Evans et al. (1974) interpreted it as the acceleration by a field-

aligned potential difference. Numerous observations have then provided evidence of particle acceleration by parallel electric fields and different processes have been invoked. We first recall that field-aligned particle acceleration does not necessarily imply parallel electric fields, an example being the Fermi acceleration. We then present some of the main classes of processes involving quasi-static and transient parallel electric fields.

a) *Fermi acceleration*

The Lagrangian formulation of mechanics describes the particle motion through “generalized coordinates” and associated “generalized momentum”. It allows in particular an easy derivation of the conservation laws for cyclic motions. In magnetized environments, particles are rotating around the magnetic field. The first adiabatic invariant associated to this cyclotron motion is μ :

$$\mu = \frac{1}{2} \frac{mv_{\perp}^2}{B} \quad (34)$$

where m is the particle mass and v_{\perp} its velocity in the direction perpendicular to the magnetic field B . μ shows that the perpendicular velocity increases with the magnetic field. It is conserved if the magnetic field does not vary in time or evolves slowly relative to the gyration period. At time scales much larger than the cyclotron motion, the particle motion is represented by the guiding center of this cyclotron motion. In an approximately dipolar planetary magnetic field, the magnetic field magnitude increases along magnetic field lines from the apex towards the planet. The conservation of the first adiabatic invariant μ shows that the mirror points are located at the points where the magnetic field is equal to B_m , such that:

$$\frac{1}{B_m} = \frac{(\sin \alpha_0)^2}{B_0} \quad (35)$$

where α_0 and B_0 are the particle pitch-angle and magnetic field magnitude at a given point along the magnetic field line, for example at the apex. The pitch-angle, α , is the angle between the particle velocity and the magnetic field. The location of the mirror points does not depend on the particle energy but only on its pitch-angle. If the particles do not cross another medium with different properties before reaching their mirror points, they remain trapped in the magnetosphere describing this bouncing motion along magnetic field lines.

The Fermi acceleration along magnetic field lines is related to the second adiabatic invariant. The second adiabatic invariant, also called longitudinal invariant, associated with this bounce motion is I:

$$I = \int_{M_S}^{M_N} p_{\parallel} dl \quad (36)$$

where p_{\parallel} is the particle momentum ($m v_{\parallel}$) in the direction parallel to the magnetic field, dl an elementary distance along the curved magnetic field line, M_N and M_S , the magnetic mirror points in each hemisphere, and the integral is taken along the bounce motion. If the magnetic field does not vary in time or evolves slowly relative to the particle bounce motion, the second adiabatic invariant is conserved. An order of magnitude is given by

$$I \approx m v_{\parallel} L_{SN} \quad (37)$$

where $\langle v_{\parallel} \rangle$ is the average velocity in the direction parallel to the magnetic field and L_{SN} , the total length along the magnetic field line between the two mirror points. If for an external cause, the distance between the two mirror points decreases, the conservation of I implies that v_{\parallel} increases: this is the so-called Fermi acceleration along magnetic field lines and it does not involve any parallel electric fields. In planetary magnetosphere, this occurs for example during compression events or substorms. More generally, the Fermi acceleration is considered as an efficient process to explain particle acceleration at shocks or the acceleration of cosmic rays.

b) *Parallel electric fields, currents and particle acceleration*

While most magnetospheric particles remain bouncing back and forth along magnetic field lines between their mirror points, only particles with mirror points located at ionospheric altitudes or below will reach the ionosphere. Their pitch-angle at the field line apex (see Equation (33)) will be smaller than a maximum pitch-angle α_c , half-angle of the so-called loss cone:

$$(\sin \alpha_c)^2 = \frac{B_0}{B_I} \quad (38)$$

where B_I and B_0 are the magnetic field magnitude at the ionospheric end and at the apex of the magnetic field line. The loss cone is small: for a dipolar magnetic field decreasing

with the cube of the distance, the loss-cone angle is of the order of a few degrees at a distance of 10 planetary radii. In planetary magnetospheres, particles within the loss cone are lost from the magnetosphere due to collisions with the upper atmosphere. These precipitating particles also have the fundamental property to be the only magnetospheric particles capable of carrying field-aligned currents between the magnetosphere and the ionosphere. Conversely, the mirror force is favorable for ionospheric particles. All ionospheric particles that could be extracted from the ionosphere reach the magnetosphere and contribute to carry currents.

Highly conductive magnetic field lines provide an electrodynamic coupling between magnetosphere and ionosphere by connecting both plasmas, by transmitting perpendicular electric fields and by circulating field-aligned currents. Both media, ionosphere and magnetosphere, permanently undergo independent large-scale or local processes that modify their electric field and current distribution at a given time. These modifications are transmitted in the conjugate medium through field-aligned currents where they cause a modification of the electrodynamic parameter distribution, which is transmitted to the conjugate medium through field-aligned currents in a self-consistent feed-back process. If the required current density is larger than the density available from magnetospheric current carriers, then the coupling is imperfectly achieved and both media are partially disconnected. In this case, the generation of parallel electric fields represents a way to achieve the required current circulation given that the particle acceleration contributes to the increase in the field-aligned current density to the required value. Such parallel electric fields can be associated with quasi-static structures or with transient processes such as waves.

c) *Quasi-static parallel electric fields*

All developed magnetospheres show evidence of accelerated particles, as for example accelerated electrons precipitating into ionosphere and responsible for auroral light emissions. In the terrestrial magnetosphere, observations show auroral electrons accelerated to keV energies; they move faster than the local Alfvén speed, so that they cannot stay in phase with Alfvén waves. This result led Knight (1973) to consider a simple quasi-static model for field-aligned currents carried by ionospheric and magnetospheric electrons accelerated by a quasi-steady parallel electric potential. From

the conservation of the energy and of the first adiabatic invariant, he derived a general current – voltage relationship. For applications to auroral magnetic field lines, where:

$$\frac{e\Delta V}{kT_I} \gg 1 \quad \text{and} \quad \frac{e\Delta V}{kT_0} \ll \frac{B_I}{B_0}$$

it simplifies to:

$$j_{\parallel} \sim -en_0 \sqrt{\frac{kT_0}{2\pi m_0}} \left(1 + \frac{e\Delta V}{kT_0} \right) \quad (39)$$

and, if $\frac{e\Delta V}{kT_0} \gg 1$, it becomes:

$$j_{\parallel} \sim -en_0 \sqrt{\frac{kT_0}{2\pi m_0}} \left(\frac{e\Delta V}{kT_0} \right) \quad (40)$$

where k is the Boltzmann's constant, e and m_e the electron mass and charge, n_0 and T_0 respectively the magnetospheric electron density and temperature, T_I is the ionospheric temperature, ΔV is the total potential drop between the ionosphere and the magnetosphere: $\Delta V = E_I - E_0$, B_I and B_0 respectively the ionospheric and magnetospheric magnetic fields.

This relation provides an estimate of the field-aligned current density that the plasma can carry between the ionosphere and the magnetosphere without any parallel electric fields ($\Delta V=0$). It also shows that the presence of a potential drop allows increasing this threshold value to much larger current densities if required for other reasons (e.g., current continuity, mismatch between the ionosphere and the magnetosphere). Field-aligned currents associated with a positive potential drop are directed upward, which corresponds to auroral observations. Improvements were presented by Chiu and Schulz (1978), who took into account the motion of the ions in such a potential structure and their contribution to field-aligned currents.

Following similar steps, Lyons (1980) demonstrated that discontinuities with $\text{div } \mathbf{E} \neq 0$ in the large-scale electric field pattern could generate large-scale regions of field-aligned currents, associated with parallel electric fields and electron acceleration. Such

discontinuities are known to exist near magnetospheric boundaries (boundaries of the plasma sheets, boundary layers, etc) in large-scale plasma flow inhomogeneities. A discontinuity with: $\text{div } \mathbf{E} < 0$ (>0) would account for upward (downward) field-aligned currents. A typical width of such structures would be of the order of 100 km in the terrestrial ionosphere, i. e. about 0.01 Earth radius.

Acceleration structures are observed at smaller scales in the auroral zone. For instance, accelerated electron precipitations are observed with a typical shape of inverted V and with widths about ten times smaller (~ 0.001 Earth radius in the terrestrial ionosphere) than the preceding effect. Such acceleration structures are interpreted as the acceleration due to a U-shaped field-aligned upward potential structure, as illustrated in **Figure 11** adapted from Carlson et al. (1998). The magnetic field near the planet is highly incompressible, resulting in nearly electrostatic structures. Downgoing field-aligned electrons crossing the middle of the structure will gain an energy corresponding to the total upward potential drop, but only a fraction of it if they cross the sides. This effect produces the well-known inverted-V shape for the acceleration structure observed by spacecraft flying below it. Spacecraft crossing at higher altitudes (near the top of **Figure 11**) will detect outflowing ions accelerated at energies corresponding to the potential drop below the spacecraft and thus with the typical inverted V shape for the same reasons. They will also observe large convergent electric fields near the edges of the structure, as shown in **Figure 11**. These electric structures are not detected below the spacecraft, implying the presence of an electrostatic shock associated with parallel electric fields at intermediate altitudes as shown in **Figure 11** (see a review by Mozer and Hull, 2001). Precipitating electrons and outflowing ions carry upward currents.

Diverging electrostatic shocks are also observed and produce the opposite effects with up-going electrons accelerated to somewhat lower energies than the preceding case, and carrying downward currents. More details can be found in a review by Marklund (2009).

De Keyser et al. (2010) proposed a different mechanism to explain the existence of small-scale quasi-static bipolar (convergent or divergent) electric fields. They considered the case of the field-aligned boundary between a dense region of hotter particles and a diluted region of colder particles, as for example the boundary between the plamasheet and the lobes. This boundary is approximated as a tangential discontinuity which has a finite thickness of the order of the largest Larmor radius, i. e. that of the hotter ions. The

transition width differs for each species and is related to their Larmor radius. The difference between the Larmor radii of the hot ions and the hot electrons will produce a charge separation and thus a polarization electric field perpendicular to the interface. The same occurs for the cold ions and electrons, but their Larmor radii are much shorter. In the absence of any potential structure across the interface, this polarization electric field displays a wider region (related to the hot ion Larmor radius) of smaller magnitude and a smaller region (related to the hot electron Larmor radius) of larger magnitude directed in the opposite direction, so that the integrated electric field over the interface cancels out. This produces the bipolar electric field structure. The presence of a potential across the interface attracts or repels ions and electrons depending on its sign, which in both cases results in a monopolar electric field structure, also observed. The mapping in the ionosphere of this magnetospheric electric field distribution and the closure of the currents in the ionosphere lead to the generation of parallel electric fields and currents.

These quasi-static models are very useful in explaining the observed particle acceleration, field and current signatures related to quasi-static structures. However, they cannot explain observations of transient or highly time-dependent features in the distribution of electric fields and currents.

d) *Transient acceleration*

Accelerated particles and large currents are factors capable of triggering instabilities and of generating waves through wave-particle interactions. These waves contribute to modify in turn the initial particle distribution by energy and pitch-angle scattering of the resonant particles, or by energy and momentum propagation to other regions. As a result, the initial electric currents and fields are modified.

d.i) Wave-particle interactions and radiation

In ideal MHD, shear Alfvén waves propagate with perpendicular electric fields. They have the property to carry field-aligned currents. When perpendicular scales become too small, the ideal MHD approximation is no longer fulfilled, the waves become dispersive and a parallel electric field appears in so-called kinetic Alfvén waves. In the topside terrestrial ionosphere, parallel electric fields can become very important at altitude below a few Earth's radii (Alfvén resonator). The same is true above Jupiter's ionosphere (Ergun *et al.*, 2006). Numerical simulations suggest that Alfvén waves should evolve towards small scales, with the appearance of a filamentary structure resulting in

electrostatic structures such as strong Double Layers (DLs) (*Mottez and Génot, 2011*). High resolution remote sensing of the Io-Jupiter magnetic flux tube based on radio waves observations have demonstrated the existence of strong DLs (up to ~ 1.5 keV amplitude), which were found to move upwards along the magnetic flux tube at the plasma sound velocity (*Hess et al., 2007, 2009*).

Paschmann et al. (2003) reviewed typical effects at different frequencies occurring in regions of upward and downward currents of the terrestrial auroral zone. Briefly, electron solitary waves or ELF electric field turbulence are found in downward field-aligned region, associated with divergent electric fields and up-going field-aligned electrons. This is the source region of VLF saucers (whistler emissions) and among the first radio emissions observed in the auroral zone. Large-amplitude ion cyclotron waves and electric field turbulence are found in upward current regions, associated with convergent electric fields and precipitating “inverted-V” events. This is also the source region of auroral radiation, powerful emissions observed in the auroral zones of magnetized planets.

One of the most powerful emissions is the auroral radiation observed above the auroral zone of the magnetized planets. These emissions are primarily driven by precipitating electrons accelerated to keV energies. The generation mechanism is well identified as the Cyclotron Maser Instability (*Wu and Lee, 1979*) and has been extensively studied (see review by Treumann, 2006). In situ observations, especially by Viking and FAST, have shown that the source regions are the acceleration regions described in Figure 11, which are strongly depleted in cold plasma ($f_{pe} / f_{ce} < 0.1$ to 0.3) due to the parallel electric field structure (*Roux et al., 1993*). The instability appears to be most efficiently driven by quasi-trapped energetic electrons, i.e. keV electrons with velocity mostly perpendicular to the magnetic field. However, this quasi-trapped electron population lies in a region of velocity space which should be empty in a simple adiabatic theory, thus its presence in the auroral zone was suggested to be due to time-varying (or space-varying) parallel electric fields (*Louarn et al., 1990*). The above filamented Alfvén waves are good candidates, consistent with the filamentary structure of the depleted sources of auroral radio radiation.

d.ii) Reconnection acceleration

Magnetic reconnection is a well-known example of transient situations. The simplest concept involves a configuration with a “X-point” in a 2D geometry, where the magnetic field vanishes. More complicated configurations are considered with 3D geometries, with

guide field. In the “frozen-in” conditions where $\mathbf{E} + \mathbf{V} \times \mathbf{B} = 0$, all points of a given magnetic field line will remain magnetically connected during their motion at the velocity \mathbf{V} . The magnetic reconnection implies that the magnetic field line has been modified or broken and the existing connection region reconnected with another one. This leads to a global reconfiguration of the magnetic structure. Reconnection is generally considered as the result of a local departure from the “frozen-in” conditions and involves parallel electric fields. The triggering factors differ on the plasma types, near the Sun or in planetary magnetospheres; it is generally difficult to predict the time and location where they occur. One of the distant signatures, well-identified onboard spacecraft, is again the particle acceleration. It is observed in the perpendicular direction mainly near the central part of the plasmashet or in the parallel direction along the separatrices (*Paschmann, 2008*).

On the magnetopause, reconnection can be accompanied by the development of vortices due to the Kelvin-Helmholtz instability. This process is known to occur at Earth (see e.g. *Hasegawa et al., 2009*), Mercury (*Sundberg et al., 2011*), and Saturn (*Delamere et al., 2013*). Parallel acceleration of electrons is caused by K-H waves, as strongly suggested at Saturn by the observation of Cyclotron Maser radio emission from the morningside sector of the magnetosphere (*Galopeau et al., 1995*).

2.5. Non-adiabatic acceleration

It is sometimes said that the motion of charged particles is nonadiabatic when the second adiabatic invariant (viz., the action integral $I \equiv m \int V_{\parallel} ds$ associated with the particle bounce motion; see Equation (33)) is not conserved. This may be the case for instance during substorm dipolarization of the magnetic field lines that can lead to different particle energization depending upon their bounce phase ; hence, the formation of bouncing ion clusters (e.g., *Mauk, 1986*). However, in the most general case, the motion of charged particles is defined as being nonadiabatic when the first adiabatic invariant (i.e., the magnetic moment associated with the particle gyromotion Equation (34)) is not conserved. This may occur either when the length scale of the field variation is comparable to or smaller than the ion Larmor radius (spatial nonadiabaticity) or when the time scale of the field variation is comparable to or smaller than the ion cyclotron

period, i.e., temporal nonadiabaticity (e.g., *Northrop*, 1963). Under such conditions, the guiding center approximation is not appropriate to investigate the motion of charged particles and a description based on the full equation of motion is necessary. In the steady state terrestrial magnetosphere, the guiding center approximation may be used to characterize the transport of charged particles in the lobes where substantial centrifugal acceleration (up to a few tens of eV) due to $\mathbf{E} \times \mathbf{B}$ convection of the magnetic field lines may be obtained (e.g., *Cladis*, 1986). The guiding center approximation also is appropriate in the nearly dipolar region of the inner magnetosphere. As a matter of fact, in this region of space, the second adiabatic invariant often is conserved as well so that an adiabatic bounce-averaged description may be adopted to explore the dynamics of, e.g., ring current and radiation belt particles (e.g., *Fok et al.*, 2006). As for the third adiabatic invariant associated with the particle azimuthal drift about the planet, it is often violated ; hence, prominent radial diffusion of the particles takes place.

a) *Spatial nonadiabaticity*

At large distances in the equatorial magnetotail, the magnetic field significantly varies on the length scale of the particle Larmor radius and a gyro-averaged description such as that of the guiding center cannot be applied. To characterize the particle behavior, *Sergeev et al.* (1983) introduced a scaling parameter K defined as the minimum field line curvature radius-to-maximum particle Larmor radius ratio. *Sergeev et al.* (1983) demonstrated that, as K becomes smaller than ~ 8 , deviations from an adiabatic behavior gradually develop as identified by, e.g., the injection of trapped particles into the loss cone. In a subsequent study, *Sergeev et al.* (1993) identified the latitude in the auroral zone where the parallel flux becomes comparable to the perpendicular one, as the projection at low altitudes of the nonadiabaticity threshold in the magnetotail (for given particle species and energy). This latitudinal boundary that is referred to as "Isotropy Boundary" forms a convenient proxy to remotely probe the distant tail topology from low-altitude measurements, as shown for instance by *Newell et al.* (1998).

The fact that particles may not perform a regular helical motion and actually behave in a nonadiabatic manner in the distended Earth's magnetotail was already uncovered in the pioneering work of *Speiser* (1965). In the case of a pure neutral sheet such as the self-consistent one of *Harris* (1962) with opposite magnetic field orientations on either side of

the midplane, Speiser (1965) showed that particles execute rapid oscillations about the midplane and are subsequently lost into the flanks. In the case of a quasi-neutral sheet with a small magnetic field component normal to the midplane, such as that due to the Earth's dipole field, Speiser (1965) showed that the above oscillations are coupled with a slow rotation of the oscillation plane so that particles may be turned back toward the planet instead of traveling into the flanks. Sonnerup (1971) considered the action integral $I_z \equiv m \int V_z dZ$ (see Equation (36)) to characterize the behavior put forward by *Speiser* (1965) since particle orbits do have some regularity (although not in an adiabatic sense).

Using Poincaré surfaces of section or, equivalently, phase space mapping upon crossing of the midplane, Chen and Palmadesso (1986) examined the dynamics of charged particles in the magnetotail in a more systematic manner. In this latter study, it was shown that the above Speiser orbits actually form one of three distinct classes of nonadiabatic orbits. That is, in the Speiser regime, particles do not experience significant pitch angle scattering upon crossing the neutral sheet and those originating from regions of strong magnetic field may return to such regions after neutral sheet crossing ; hence, their denomination as "transient" particles. In the second class of orbits, particles experience prominent pitch angle scattering upon crossing of the neutral sheet. Accordingly, particles originating from regions of strong magnetic fields may remain temporarily trapped near the midplane, while those trapped near the midplane may escape after crossing of the neutral sheet ; hence, their denomination as "quasi-trapped" particles. Finally, a third class of orbits consists of particles that remain trapped near the midplane, an example of them being the ideal case of particles with 90° pitch angle at equator (see Figure 4 of Chen and Palmadesso (1986)). Chen and Palmadesso (1986) showed that the phase space is systematically partitioned according to these three distinct orbit classes and that the Speiser regime becomes predominant for specific values of the (normalized) Hamiltonian.

Following the approach of Sonnerup (1971), Büchner and Zelenyi (1989) developed a comprehensive interpretation framework of the particle dynamical behaviors. The formalism put forward in this latter study relies on a piecewise description of the particle motion, considering that it can be viewed as a succession of $I_z \equiv m \int V_z dZ$ conserving sequences (see Equation (36)). In this interpretation framework, at some point during transport toward the neutral sheet, particles cross a phase space separatrix that delineates

two different dynamical regimes (viz., crossing and non-crossing of the midplane). In the course of these separatrix crossings, small quasi-random jumps of the invariant I_z occur as put forward by Neishtadt (1987) (see Figure 14 of Büchner and Zelenyi (1989)). In this approach, the Speiser regime (also referred to as “transient”) corresponds to a negligible net change of I_z ; hence, its denomination as “quasi-adiabatic”. In contrast, in the above quasi-trapped regime (also referred to as “cucumber-like” in Büchner and Zelenyi (1989)), particles are subjected to significant net changes of I_z . To describe these I_z changes, Büchner and Zelenyi (1989) introduced a parameter κ defined as the square root of the minimum field line curvature radius-to-maximum Larmor radius ratio (see, e.g., Equation (41) of Büchner and Zelenyi (1989)). This latter κ parameter, that is now commonly used to characterize the adiabatic character of the particle motion, is the square root of the K parameter of Sergeev et al. (1983). It is also comparable with the dimensionless Hamiltonian used by Chen and Palmadesso (1986) since one has $2H \equiv \kappa^4$. According to the analysis of Büchner and Zelenyi (1989), the particle motion turns nonadiabatic for $\kappa < 3$ (equivalently, $K < 8$ in Sergeev et al. (1983)), and the above regimes with transient (Speiser) and quasi-trapped behaviors are obtained for $\kappa < 1$ (a κ regime that is also referred to as the current sheet limit). Between $\kappa > 3$ and $\kappa < 1$, there exists an intermediate regime where particles do not oscillate about the midplane (because of Larmor radii smaller than the field reversal length scale) but their motion is chaotic.

Delcourt et al. (1994) further explored this intermediate $1 < \kappa < 3$ regime, considering a centrifugal perturbation of the particle motion near the magnetotail midplane. The interpretation framework developed in this latter study is that the adiabatic (magnetic moment conserving) sequences upon approach and exit of the neutral sheet are separated by a critical cyclotron turn during which an impulsive centrifugal force (due to the enhanced field line elongation) perturbs the cyclotron motion of the particles. This so-called Centrifugal Impulse Model that describes a single (prototypical) crossing of the field reversal leads to a characteristic three-branch pattern of magnetic moment variations, viz., (i) at small pitch angles, large magnetic moment enhancements regardless of the particle gyration phase, (ii) at large pitch angles, negligible magnetic moment changes and (iii) at intermediate pitch angles, either magnetic moment enhancement or damping depending upon gyration phase. As κ decreases from 3 toward 1, this three-branch pattern gradually expands in velocity space, consistently with the results of *Sergeev et al.* (1983)

(see Figure 1 of Delcourt et al. (1996)). Repeated crossings of the field reversal (equivalently, repeated applications of the three-branch pattern of magnetic moment variations) lead to a chaotic behavior with prominent dependence upon initial phase of gyration since magnetic moment enhancement and damping are obtained at small and intermediate pitch angles, respectively.

In this respect, using single-particle simulations in a model magnetic field of the magnetotail, Ashour-Abdalla et al. (1992) suggested that the $\kappa \approx 1$ regime leads to enhanced particle trapping and duskward drift, a feature referred to as the "wall" region. This $\kappa \approx 1$ regime lies in the mid-tail at the transition between the nearly dipolar region where the particle motion is adiabatic ($\kappa > 3$) and the distant tail where one has $\kappa < 1$. It corresponds to the onset ($K = 8$) of nonadiabaticity examined by Sergeev et al. (1983) and the "wall" feature is thus at odds with the "Isotropy Boundary" interpretation framework discussed above with particle injection into the loss cone and subsequent precipitation. However, the three-branch pattern obtained with the Centrifugal Impulse Model suggests that the two behaviors coexist, the "wall" feature corresponding to large magnetic moment enhancements at (relatively) small pitch angles while the "Isotropy Boundary" follows from damping of the magnetic moment at intermediate pitch angles.

The nonadiabatic features discussed above are of paramount importance for the development of thin current sheets that are essential magnetotail elements at Earth and at other planets. In the terrestrial magnetosphere, in situ observations from GEOTAIL, CLUSTER and THEMIS have revealed a number of magnetic field features in the tail current sheet such as flapping, flattening, tilting, waving, twisting and bifurcation. This current sheet can become very thin (with a thickness comparable to the ion inertial length), yielding a metastable state that can lead to current sheet disruption as observed during the expansion phase of substorms (e.g., Mitchell et al., 1990). The formation of nongyrotropic distribution functions in these nonadiabatic regimes also leads to nonzero off-diagonal terms in the pressure tensor and allows for a current sheet equilibrium that does not require a prominent pressure gradient along the tail axis (e.g., Ashour-Abdalla et al., 1994). As for the predominant Speiser regimes obtained within specific $\kappa < 1$ intervals, they follow from resonance between the fast particle oscillation about the midplane (imposed by the opposite orientations of the magnetic field above and below the midplane) and the slow gyromotion (imposed by the small magnetic field component

normal to the midplane). In this Speiser regime, particles are subjected to prominent energization owing to large displacement along the dawn-to-dusk convection electric field. This efficient Speiser acceleration can thus lead to large particle flux within limited intervals at high energies (small κ) ; hence, the formation of "beamlets" traveling down to low altitudes as reported in CLUSTER observations (see, *Keiling et al.*, 2004).

b) *Temporal nonadiabaticity*

It was mentioned above that during the expansion phase of substorms, the second adiabatic invariant may not be conserved (*Mauk*, 1986). Indeed, the short-lived electric field induced by dipolarization of the magnetic field lines can lead to significant energization of particles that are located in the equatorial vicinity while those located at low altitudes may remain unaffected. Here, violation of the second adiabatic invariant is due to temporal variations of the magnetic field on the time scale of the particle bounce period. Note that this second adiabatic invariant may be violated because of spatial variations of the magnetic field as well, as is the case for instance near the frontside magnetopause where particles evolve from bouncing about the equatorial plane to bouncing about the field minimum in the outer cusp region (*Shabansky*, 1971 ; *Delcourt and Sauvaud*, 1999).

Still, temporal variations of the magnetic field can also lead to violation of the first adiabatic invariant, a behavior that is obtained whenever the magnetic field varies significantly on a time scale comparable to the particle gyro-period. In this regard, it was shown by Delcourt et al. (1990) that, during dipolarization of the magnetic field lines, violation of the first adiabatic invariant may be obtained for heavy ions (O^+) that have cyclotron periods of a minute or so in the terrestrial mid-tail. As a result, while protons with small gyro-periods behave in an adiabatic manner (with respect to the first invariant), O^+ may experience prominent nonadiabatic energization, in a like manner to spatial nonadiabaticity, where protons and O^+ ions may exhibit $\kappa > 3$ and $\kappa \leq 1$, respectively.

Unlike the energization by the large-scale convection electric field that is constrained by the magnitude of the cross-polar cap potential drop (typically, in the 50 kV - 150 kV range) so that ions drifting over a few R_E across the steady state magnetotail can gain at most a few tens of keV, there is no well defined limit for the energization that can be achieved from the induced electric field (*Heikkila and Pellinen*, 1977 ; *Pellinen and*

1299 *Heikkila*, 1978). Delcourt et al. (1990) actually showed that O⁺ energization up to the 100
1300 keV range is readily obtained during substorm reconfiguration of the magnetic field lines.
1301 Since this energization occurs in a nonadiabatic manner and goes together with prominent
1302 enhancement of the particle magnetic moment, it radically changes the long-term
1303 behavior of the particles that may evolve from an open drift path (i.e., connected to the
1304 dayside magnetopause) to injection into the ring current and rapid gradient drift around
1305 the planet owing to the large energy gain realized (see Figure 5 of *Delcourt* (2002)).

1306 At Earth, a variety of in situ measurements suggest that such a mass-to-charge
1307 dependent energization is at work during substorm dipolarization. Post-dipolarization
1308 spectra obtained for O⁺ can be significantly harder than those of protons (*Ipavich et al.*,
1309 1984 ; *Nosé et al.*, 2000). Observations of energetic neutral atoms by Mitchell et al.
1310 (2003) also reveal repeated injections of energetic (above 100 keV) O⁺ in conjunction
1311 with auroral break-ups, while no similar injections are obtained for protons. The
1312 (temporally) nonadiabatic heating at work here increases when the inductive electric field
1313 increases or if the ions are located further away from the inner dipolar region in the
1314 equatorial magnetotail, and it may actually occur in regions where spatial adiabaticity is
1315 achieved (viz., $\kappa > 3$). Note also that prominent fluctuations of the magnetic field on short
1316 time scales may somewhat alter this description and lead to significant nonadiabatic
1317 heating of protons as well, as displayed in the GEOTAIL data analysis of Ono et al.
1318 (2009). From a general viewpoint, temporal nonadiabaticity critically depends upon the
1319 characteristics of the magnetic field transition and one may expect that Mercury's
1320 environment with small temporal scales as compared to those at Earth is characterized by
1321 specific nonadiabatic responses.

1324 2.6. Pick-up acceleration and mass loading

1325 Ions produced within a flowing plasma are a significant source of energy and a sink
1326 of momentum, as well as being a source of plasma. Although sometimes used more
1327 generally, the classical pick-up process occurs when the parent neutrals have a velocity
1328 different from the $(\vec{E} \times \vec{B})/B^2$ drift of the local plasma. The new ions are then accelerated
1329 by the convection electric field and form a ring-beam distribution in velocity space. This

distribution is unstable to the cyclotron maser instability and may result in the generation of electromagnetic ion cyclotron waves.

Neglecting the energy lost to these waves, the ions have an energy, in the plasma frame, of $2 m v_{\text{rel}}^2$ (where v_{rel} is relative velocity between the source neutrals and local plasma) or four times the ram energy of a background ions of the same mass. In many cases, this can be a significant source of plasma heating. In addition, acceleration by the convection electric field initially causes the newly created ion and electron to move in opposite directions, and their guiding centers become separated by a gyroradius. The

resulting “pick-up current” is $\vec{J} = \frac{v_{\text{rel}} m}{B} \frac{dn}{dt} = \frac{m}{B^2} \frac{dn}{dt} \vec{E}$. This is often treated as a “pick-up” conductivity (*Thomas et al.*, 2004 and references therein). The pick-up current, flowing across the background magnetic field, also acts to slow, or mass-load the plasma.

In one common case, pick-up acceleration, heating and mass-loading may occur without producing a net source of mass or plasma. If the ions are produced through symmetric charge exchange, $X^+ + X \rightarrow X + X^+$, then the newly ionized particle will be accelerated as any other pick-up ion, producing a ring-beam distribution, heating and mass-loading. However, the reaction will also generate a fast neutral which escapes the system. As a result, there is no net change in the ion density.

3. Losses

In previous sections, we have considered the various sources of plasma and their transport and energization processes to supply magnetospheric plasmas. We next consider the ways in which this material can be lost from the system, to “balance” the mass budget. There are a number of methods by which plasma can be lost from magnetospheres.

3.1. Tail reconnection and plasmoids

Magnetic reconnection in a planetary magnetotail is a key mechanism by which magnetic field lines stretch to instability and break, which then allows the release of parcels of mass and plasma called plasmoids, of varying sizes and shapes (*Hones, 1976; 1977*). Observations in the Earth’s magnetosphere have shown that plasmoids are typically about 1 to 10 R_E in diameter (*Ieda et al., 1998; Slavin et al., 2003*). Figure 12 shows a schematic of the formation of earthward and tailward-moving plasmoids following reconnection. Figure 13 shows the magnetic field signatures what would result from a spacecraft track through an idealized plasmoid. In situ observations of tail reconnection include observations of changes in magnetic field topology and plasma flows. In recent years the study of tail reconnection has been extended beyond Earth. Plasmoids have been observed in the magnetotails of Saturn (e.g. *Jackman et al., 2007; 2011; 2014b*), Jupiter (*Russell et al., 1998; Vogt et al., 2010, 2014*), and Mercury (*Slavin et al., 2009; 2012b; DiBraccio et al., 2014*).

In recent years several authors have sought to consider the role of tail reconnection as a loss mechanism for magnetospheric plasma (e.g. *Bagenal and Delamere, 2011*). At Jupiter, Bagenal (2007) highlighted the mismatch between the inferred mass input rate from Io of ~500-100 kg/s and the mass loss rate from plasmoids, estimated at ~30 kg/s. Kronberg et al. (2008) attempted a similar calculation (based on Galileo energetic particle measurements) and found that their inferred mass of $\sim 8 \times 10^5$ kg per plasmoid would require far more plasmoids than had been observed to account for the input. Vogt et al, (2014) completed the most comprehensive study to date at Jupiter, whereby they found that mass loss ranged from ~0.7-120 kg/s. They concluded that while tail reconnection is indeed an active process at Jupiter, it likely cannot account for the mass input from Io, suggesting that additional mass loss mechanisms may be significant. Jackman et al. (2014b) investigated the analogous picture at Saturn. They found an average mass loss

rate of ~ 2.59 kg/s, much less than the ~ 100 kg/s expected to be loaded into the magnetosphere by the volcanic moon Enceladus.

These studies raise the question: If large-scale reconnection is not sufficient to account for the required loss of material from the tails of Jupiter and Saturn, what other processes/new physics are required to balance the mass budgets? Other loss mechanisms are investigated in the sections below.

3.2. Charge exchange

In Earth's magnetosphere, there exist a region called the ring current, where high energetic ions and electrons with energy between hundreds of eV and hundreds of keV are trapped by Earth's dipole-dominated magnetic field (*Frank, 1967; Williams, 1981*). In the ring current, the ions (electrons) drift westward (eastward) due to the magnetic drift, and the ring current development causes the decrease in the horizontal magnetic field component at Earth's surface. Thus, the strength of the ring current is often measured by the Dst or SYM-H indices derived from ground-based magnetometer observations (*Sugiura, 1964; Wanliss and Showalter, 2006*). If the planetary magnetic field is strong enough and dominated by the dipole component as well as there is transportation and energization process to populate high-energy ions in the inner magnetosphere, the ring current is expected to exist in other planets.

One efficient loss mechanism for the terrestrial ring current particles is the charge exchange (see Equations (22) and (23)) of the ring current ions with the neutral hydrogen that makes up the geocorona. When the convection weakens, this becomes the dominant process by which ring current ions are removed from the system, depleting the inner magnetosphere of its energetic population. The geocorona is a halo-like extension of the exosphere out to several Earth radii, consisting of relatively cold (~ 1000 K), very tenuous neutral hydrogen atoms with densities ranging from thousands of atoms per cubic centimeter at the inner edge of the ring current to less than a hundred at geosynchronous orbit. This cold gas plays a critical role in the energy budget of the Earth's inner magnetosphere since the charge exchange reactions make the exosphere act as an energy sink for ring current particles, replacing a hot ion with a cold one. Singly charged ring current ions can be neutralized after collisions with thermal exospheric hydrogen atoms as described below:

$$H^+ + H_{cold} \rightarrow H + H_{cold}^+ \quad (41)$$

$$O^+ + H_{cold} \rightarrow O + H_{cold}^+ \quad (42)$$

$$He^+ + H_{cold} \rightarrow He + H_{cold}^+ \quad (43)$$

The incident ring current ion picks up the orbital electron of the cold geocoronal hydrogen atom resulting in the formation of an Energetic Neutral Atom (ENA). These particles are not affected by magnetic or electric field forces therefore they are no longer trapped in the geomagnetic field and leave the interaction region in ballistic orbits in the direction of the incident ion velocity at the time of the impact. If the resulting ENA's velocity exceeds the Earth's gravitational escape field, then it is lost into space or precipitates down into the ionosphere. On the other hand, the low energy ENAs populate the plasmasphere. Meinel (1951) first reported the existence of energetic neutral atoms, based on observations of precipitating energetic neutral hydrogen precipitating into the upper atmosphere during auroral substorms. A few years later, Dessler and Parker (1959) were the first to suggest that charge exchange between protons and neutral atmospheric hydrogen atoms would effectively contribute to the decay of the ring current, although the effectiveness of ion removal from the ring current through charge exchange processes was previously investigated by Stuart (1959) and Fite et al. (1958).

Multiply charged ions allow for multiple charge exchange reactions,

$$He^{++} + H_{cold} \rightarrow He^+ + H_{cold}^+ \quad (44)$$

and Spjeldvik and Friz (1978) showed that the higher charge states of helium and oxygen ions are increasingly important for energies above 100 keV, while at energies below this cutoff the lower charge states are dominant. Energetic neutral atoms generated in the main ring current traversing the inner magnetosphere can be re-ionized. This happens by converting ENAs back into ring current ions albeit on new L shells, undergoing subsequent charge-exchange collisions with geocoronal atoms and generating secondary ENA fluxes that can participate in further ionizing collisions (Bishop, 1996). This yields the formation of a secondary ring current close to the Earth, at L shell values of approximately 3, although this is not a large ring current population. Moreover, low pitch angle ions are subject to additional charge exchange collisions with the oxygen atoms in the upper atmosphere.

Solar far-ultraviolet light is reflected off this hydrogen gas (*Chamberlain*, 1963) and so its abundance has been quantified. It has been reported (*Fahr*, 1974; *Rairden et al.*, 1986; *Hodges*, 1994; *Østgaard et al.*, 2003; *Fuselier et al.*, 2010; *Zoennchen et al.*, 2010; *Bailey and Gruntman*, 2011; *Zoennchen et al.*, 2011) that the geocoronal hydrogen density decreases exponentially with radial distance. This means that at large altitudes down the magnetotail, the collisions with the neutral hydrogen become negligible. However, in the ring current region, these collisions become increasingly important and magnetospheric H⁺ can be easily removed by charge exchange with the neutral exospheric hydrogen.

The probability of collisions with neutral atoms from the exosphere depends strongly on the energy of the incident particles and is determined by the charge exchange cross sections. Charge exchange cross sections are both energy and species dependent and thus different ring current ion species have different charge exchange lifetimes. A compilation of charge exchange cross sections for various ring current ions can be found in *Spjeldvik* (1977), *Smith and Bewtra* (1978), and *Orsini and Milillo* (1999).

Numerous studies, both based on both observations and numerical modeling show that due to the strong species and energy dependence of the charge-exchange cross sections along with the temporal and spatial dependence of ring current composition, the charge exchange process strongly affects the ring current plasma. **Figure 14** shows the profile of charge exchange lifetime as a function of energy and species (*Liemohn and Kozyra*, 2005). Moreover, it is inferred that the charge exchange loss processes are predominantly important after the initial phase of the ring current decay.

The efficiency of ion removal from the ring current through charge exchange depends on several factors: the energy and the species of the ion population as well as the density of the neutral cloud. The latter depends on the changes in the atmospheric temperature and density, the radiation pressure exerted by the solar far ultra violet photons and the strengths of all these interactions determine the structure of the exosphere. Therefore reliable measurements of the geocoronal density are essential in determining the relative importance of charge exchange losses of ring current ions. The majority of geocoronal models report on vastly different densities in the inner magnetosphere (*Ilie et al.*, 2013) and therefore the decay rates and lifetimes for ring current ions are significantly different depending on the neutral density distribution, affecting the amount of ENAs emitted in a given region in space (See **Figure 15**).

Keika et al. (2003; 2006), based on measurements of energetic neutral atoms (ENAs) made by the High Energy Neutral Atom (HENA) imager on board the Imager for Magnetopause-to-Aurora Global Exploration (IMAGE) satellite, show that the rate of the charge exchange energy losses is comparable to the ring current decay rate for the intervals of the slow decay, while the loss rate is much smaller than the decay rate in the rapid decay phase, in particular for the early stage of a storm recovery. Similarly, Jorgensen et al. (2001) show that during the fast recovery the measured ENAs can only account for a small portion of the total energy loss and the lifetime of the trapped ions is significantly shorter during the fast recovery phase than during the late recovery phase, suggesting that different processes are operating during the two phases. Furthermore Kozyra et al. (2002) suggested that charge-exchange losses can be solely responsible for the decay of the ring current during the recovery phase only if IMF abruptly turns northward at the end of the main phase.

The neutral gases in the upper atmospheres of Jupiter and Saturn are molecular and atomic hydrogen and thus either as a result of direct ionization or dissociative ionization a significant number of H^+ ions are created. H^+ can only recombine directly via radiative recombination, which is an extremely slow process and thus there must be other ways to remove them otherwise very large ion densities would result. As explained in Subsection 1.2 as one of c) loss processes and ion chemistry, it was suggested some time ago (McElroy, 1973) that the following charge exchange would be important in removing H^+ :



H_2^+ is rapidly transformed to H_3^+ via the following reaction:



H_3^+ will most likely undergo dissociative recombination and thus this series of reactions removes ions relatively rapidly. There is another way that H^+ can be lost at Jupiter and Saturn (see Equation (25)), namely by reacting with water molecules, originating in the rings (Connerney and Waite, 1984).

3.3. Precipitations into planets

a) *High latitudes*

As seen in section 2.4, the atmospheric loss cone can be defined at any location by its half-angle $\sin \alpha_{lc} = (B/B_m)^{1/2}$ (see Equation (34)) where B is the magnetic field amplitude at the position considered and B_m its value at the ionospheric end of the magnetic field line. Charged particles with pitch angle $< \alpha_{lc}$ will precipitate into the planet and be lost for the magnetosphere. The loss cone is permanently fed by new particles resulting from processes such as pitch-angle scattering by electric and magnetic fluctuations (e.g. whistler waves; see Bolton et al., (2004) and references therein). Due to the converging field line geometry, most precipitations occur at relatively high magnetic latitude ($\sim 55^\circ$ - 75°).

a.i) Auroral ovals

Precipitations of electrons with energy ≥ 0.1 keV and of protons or ions with energy \geq a few keV produce auroras (*Birkeland*, 1910), seen from the ground as curtains of light, and from space as bright variable narrow circumpolar ring, arcs and spots. The precipitating electrons have energies in the range ~ 100 eV-10 keV for the Earth (*Feldstein et al.*, 2001) and Saturn (*Cowley et al.*, 2004), reaching more than 100 keV for Jupiter (*Prangé et al.*, 1998). This is well above their thermal energy in the magnetosphere or solar wind (≤ 1 eV), thus strong acceleration is required, as discussed in section 2.2.4. Total precipitated auroral power is up to $\sim 10^{11-12}$ W for the Earth and Saturn, $\sim 10^{13-14}$ W for Jupiter (*Clarke*, 2012).

X-ray to radio emissions are produced in the high altitude atmosphere (80-300 km on Earth, 10^{-5} - 10^{-9} bar at Jupiter) or in the precipitating beam (*Prangé*, 1992; *Bhardwaj and Gladstone*, 2000). The visible aurora is most spectacular on Earth, related to the excitation/deexcitation of O (red and green lines), N (blue line) and N₂ (purple), whereas H- α and H- β lines are very faint at Jupiter. The UV aurora, 10 \times to 100 \times more intense than visible ones, result from the collisional excitation (by electrons from a few to 100 keV) and then radiative deexcitation of N₂⁺, N, H at Earth, and H (Ly- α) and H₂ (Lyman and Werner bands) at Jupiter. The X-ray aurora on Earth is mainly generated via bremsstrahlung from precipitating electrons, and at Jupiter from the collisional excitation (followed by radiative deexcitation) of deep internal levels of O and S ions by precipitating heavy ions of energy > 100 MeV. The X and UV aurorae are often pulsed on

timescales of tens of minutes. The IR auroral emission is due to atmospheric Joule heating (followed by radiative cooling). It is emitted as nitrogen lines at Earth and H_3^+ and hydrocarbons lines at Jupiter. As UV absorption by hydrocarbons is strongly frequency-dependent, the comparison between auroral and laboratory H and H_2 UV spectra provides information to deduce the depth at which precipitated energy is deposited and, with an atmospheric model, to derive the nature and energy of precipitating particles. Coherent circularly polarized cyclotron radio emissions are generated below ~ 1 MHz (≤ 40 MHz at Jupiter) by the interaction of unstable precipitating (or mirrored) energetic (1-10 keV) electron populations with electromagnetic fluctuations, in a rarefied and magnetized plasma ($f_{pe}/f_{ce} \ll 1$) (Zarka, 1998). Their generation causes the diffusion of the electrons in velocity space (Pritchett, 1986) in particular into the loss cone, causing further precipitations. Imaging the auroral activity in UV (HST - Prangé *et al.*, 1998), IR (ground-based telescopes – Connerney *et al.*, 1993) and radio (via DE-1 (Huff *et al.*, 1988) or Cassini spacecraft (Cecconi *et al.*, 2009)) permits to map the precipitations and, by projection along the magnetic field, the magnetospheric activity.

a.ii) Polar cusps and satellite-magnetosphere interactions

In addition to the auroral ovals, at the limit between open and closed field lines at Earth or near the corotation breakdown region at Jupiter and Saturn, signatures of precipitations are also observed at the magnetic footprints of the polar cusps and of satellites embedded in the giant planets' magnetospheres (Waite *et al.*, 2001; Pallier and Prangé, 2004). Cusp signatures are around 12:00 LT and reveal sporadic dayside reconnections at timescales between 5 min. (at Earth) and 20 min. (at Jupiter), causing direct precipitation of accelerated particles in the polar cusps. They are more intense for a southern solar wind B_z at Earth (northern at Jupiter). The auroral input power into the cusp is only $\approx 1\%$ of the total auroral input power. The magnetic footprints of Io, Ganymede and Europa were detected in UV at Jupiter (Bonfond, 2012), as well as that of Enceladus at Saturn (Pryor *et al.*, 2011). Precipitation in the satellites magnetic flux tubes result from the imposed current across the satellite due to the electric field $\mathbf{E} = \mathbf{v} \times \mathbf{B}$ arising from the motion of the satellite (at velocity $\mathbf{v} = \mathbf{v}_{\text{Keplerian}} - \mathbf{v}_{\text{corotation}}$) across the planetary magnetic field lines. This current is carried by Alfvén waves accelerating electrons. In the Io-Jupiter case, the precipitated power reaches 10^{12} W, i.e., $\sim 10\text{-}15$ W/m² at the satellite ionospheric footprints. This power, within a factor 2 of the solar input, strongly heats the

local ionosphere and modifies its properties, such as conductivity (*Prangé et al.*, 1996). Satellite footprints have downstream tails related to currents reaccelerating the magnetospheric plasma downstream of the obstacle.

Magnetospheric particles also precipitate onto the surface of embedded satellites. If the latter possesses a magnetic field, precipitating particles are guided toward the magnetic poles of the satellite, generating satellite auroras as well as significant surface alterations, as for example, in the case of Ganymede's polar caps (*Khurana et al.*, 2007).

b) *Low latitudes*

b.i) Radiation belts and synchrotron losses

Radiation belts consist of electrons and ions accelerated to very high energies (0.1 to >10 MeV) and brought by radial inward diffusion close to the planet (typically between the surface and ~6 radii), where they bounce between their mirror points. Satellites and rings embedded in the belts cause strong collisional absorption of these energetic particles. Unabsorbed electrons can emit synchrotron radiation, a linearly polarized incoherent nonthermal radiation from high energy electrons in cyclotron motion in a magnetic field. This emission extends over a spectral range from <100 MHz to several GHz in the case of Jupiter, and can thus be imaged by ground-based radiotelescopes (*Bolton et al.*, 2004). Intensity is maximum near the equator (trapped population) and near the poles (mirror points, where the residence time is maximum due to low parallel velocity). The lifetime of an emitting electron is relatively short (10^8 to 10^9 s), during which the perpendicular energy of the particle is radiated away and finally causes precipitation onto the planet at low latitudes ($\leq 50^\circ$). At Earth and Saturn, synchrotron emission (yet undetected) may exist at much lower frequency and intensity. Saturn radiation belts are largely absent due to ring absorption, but a small belt was discovered by Cassini between the inner edge of the rings and the planet (<1.4 Rs - *Krimigis et al.*, 2005).

b.ii) Precipitations from the rings

Other precipitation into Saturn's ionosphere come from the rings' ionized atmosphere (*Luhmann et al.*, 2006). It is composed of O_2^+ and O^+ ions between ~1.4 and ~2.4 Rs near the equator, resulting from the ionization by sunlight and magnetospheric impacts of the neutral atmosphere due to sputtering, photo-desorption and meteoroid impacts. The ion motions in the planetary quasi-dipolar magnetic field, subject to the corotation electric

1606 field, gravitation and collisional scattering, lead to precipitation into the planet at mid-
1607 latitudes (30° - 40°) of ions created at radial distances within the corotation orbit at ~ 1.8
1608 R_s . Due to the slight North-South asymmetry of the magnetic field (stronger in the
1609 northern hemisphere), precipitation (of energy ≤ 100 eV) occurs mostly in the southern
1610 hemisphere.
1611

4. Basic equations and modeling methods

4.1. MHD (Magnetohydrodynamic) simulation

The basic equations of magnetohydrodynamics (MHD) are derived in numerous textbooks including those by Chen [1984] and Krall and Trivelpiece [1986] and are traditionally presented in terms of the primitive or state variables; density (ρ), velocity (u), thermal pressure (P), and magnetic field (B) as

$$\frac{\partial \rho}{\partial t} + \nabla \cdot (\rho \vec{u}) = 0, \quad (47)$$

$$\rho \frac{\partial \vec{u}}{\partial t} + \vec{u} \cdot \nabla \vec{u} + \nabla P - \frac{1}{\mu_o} \nabla \times \vec{B} \times \vec{B} = 0, \quad (48)$$

$$\frac{\partial P}{\partial t} + \gamma \nabla \cdot (P \vec{u}) - (\gamma - 1) \vec{u} \nabla \cdot P = 0, \quad (49)$$

$$\frac{\partial \vec{B}}{\partial t} - \nabla \times (\vec{u} \times \vec{B}) = 0. \quad (50)$$

The assumption of ideal gas law has been used to define the pressure Equation (49) and the fact that the current density (J) is the curl of the magnetic field has been used to simplify the equations. More importantly in the generalized Ohm's law,

$$\vec{E} = -(\vec{u} \times \vec{B}) + \eta \vec{J} + \frac{1}{en_e} \vec{J} \times \vec{B} - \frac{1}{en_e} \nabla P_e, \quad (51)$$

terms related to the finite resistivity (η), Hall effect ($J \times B$), and electron pressure (P_e) have been neglected to get to Equation (50). This formulation is commonly referred to as the equations of ideal MHD and it is important to point out that unless some term in the generalized Ohm's law is restored either analytically or numerically it is not possible for magnetic reconnection to occur in a system that obeys the equations of ideal MHD.

Numerical simulation of these equations usually involves discretization in space and time so it is common to formulate the ideal MHD equations in conservative form in order to allow for the direct application of advanced numerical techniques. The algorithm paper by (Tóth *et al.*, 2012) not only provides a description of the motivation for utilizing conservative formulation but it also provides a more detailed discussion of the Hall and multifluid formulations than can be covered here. The conservative formulation involves equations of the form,

$$\frac{\partial U}{\partial t} + \nabla \cdot \vec{F}(U) = 0, \quad (52)$$

so that on a discrete grid the change of a conserved quantity is simply the sum of fluxes entering and leaving that cell. Recasting the ideal MHD equations in conservative form results in,

$$\frac{\partial \rho}{\partial t} + \nabla \cdot (\rho \vec{u}) = 0, \quad (53)$$

$$\frac{\partial \rho \vec{u}}{\partial t} + \nabla \cdot \left(\rho \vec{u} \vec{u} + \left(P + \frac{B^2}{2\mu_o} \right) \vec{I} - \frac{\vec{B} \vec{B}}{\mu_o} \right) = 0, \quad (54)$$

$$\frac{\partial \mathcal{E}}{\partial t} + \nabla \cdot \left(\vec{u} \left(\mathcal{E} + P + \frac{B^2}{2\mu_o} \right) - \vec{u} \cdot \frac{\vec{B} \vec{B}}{\mu_o} \right) = 0, \quad (55)$$

$$\frac{\partial \vec{B}}{\partial t} + \nabla \cdot (\vec{u} \vec{B} - \vec{B} \vec{u}) = 0. \quad (56)$$

where

$$\mathcal{E} = \frac{P}{\gamma - 1} + \frac{\rho U^2}{2} + \frac{B^2}{2\mu_o} \quad (57)$$

is the total energy density of the plasma element. In this formulation it is clear that the change in momentum density in a given region or computational cell is the result of the momentum entering or leaving the cell combined with the effects of thermal and magnetic pressure forces as well as with magnetic tension. Along with these equations comes an important constraint from Maxwell's equations, namely, the fact that the magnetic field must be divergence free ($\nabla \cdot \vec{B} = 0$) throughout the entire computation domain for all times. In computational solvers this means using a simple projection scheme, a staggered type mesh (Yee, 1966) with the magnetic fluxes defined on the faces and the electric fields on the edges, or the constrained transport 8-wave scheme (Powell *et al.*, 1999). The staggered mesh approach is used by the OpenGGCM (Raeder *et al.*, 2008) and LFM (Lyon *et al.*, 2004) global simulations of the Earth's magnetosphere. The 8-wave solver is one of several methods available in the Space Weather Modeling Framework (SWMF), which has been used for a variety of problems throughout the heliosphere (Tóth *et al.*, 2005).

Huba (2005) presents an excellent discussion of the effects of including the Hall term in the MHD equations and the numerical techniques needed to solve them. In the notation of this chapter the inclusion of the Hall term in the generalized Ohm's law results in changes to the energy and induction equations,

$$\begin{aligned} \frac{\partial \mathcal{E}}{\partial t} + \nabla \cdot \left(\vec{u}(\mathcal{E} + P + \frac{B^2}{2\mu_o}) - \vec{u} \cdot \frac{\vec{B}\vec{B}}{\mu_o} \right) \\ + \nabla \cdot \left(\vec{u}_H \frac{B^2}{2\mu_o} - 2\frac{1}{\mu_o} \vec{B}(\vec{u}_H \cdot \vec{B}) \right) = 0, \end{aligned} \quad (58)$$

$$\frac{\partial \vec{B}}{\partial t} + \nabla \cdot \left((\vec{u} + \vec{u}_H)\vec{B} - \vec{B}(\vec{u} + \vec{u}_H) \right) = 0. \quad (59)$$

where the ‘‘Hall velocity’’,

$$\vec{u}_H = -\frac{\vec{J}}{ne}, \quad (60)$$

has been introduced to clearly illustrate how the Hall terms enter the system of equations. Since these terms are only present in the energy and induction equations it should be clear that the Hall term only transports the magnetic field and energy. To be clear, this means that the Hall effects are not a transport mechanism for mass or momentum. The inclusion of the Hall term introduces a new wave mode, the whistler mode, into the dynamics of the system. The whistler wave speed is significantly larger than the Alfvén speed. This introduces challenges into numerical computation. Since it is the largest wave speed that governs the time step that can be taken within a numerical solution this limitation can result in significant increases in the computational time to the solution. This can be addressed by sub-cycling the Hall physics on the shorter timescale and calculating the ideal MHD physics on the longer timescale.

Of course, the plasma in the Earth’s magnetotail and other plasmas throughout the heliosphere can contain more than one ion species so it is often necessary to utilize the multi fluid formulations of the MHD equations to simulate these plasmas. In the notation of this paper these equations are:

$$\frac{\partial \rho_\alpha}{\partial t} + \nabla \cdot \rho_\alpha \vec{u}_\alpha = 0, \quad (61)$$

$$\begin{aligned} \frac{\partial \rho_\alpha \vec{u}_\alpha}{\partial t} + \nabla \cdot (\rho_\alpha \vec{u}_\alpha \vec{u}_\alpha + IP_\alpha) = n_\alpha q_\alpha (\vec{u}_\alpha - \vec{u}_M) \times \vec{B} \\ + \frac{n_\alpha q_\alpha}{n_e e} \left(\vec{J} \times \vec{B} - \nabla P_e \right), \end{aligned} \quad (62)$$

$$\frac{\partial \mathcal{E}_\alpha}{\partial t} + \nabla \cdot [(\mathcal{E}_\alpha + P_\alpha) \vec{u}_\alpha] = \left[n_\alpha q_\alpha (\vec{u}_\alpha - \vec{u}_M) \times \vec{B} + \frac{\rho_\alpha q_\alpha}{n_e e} (\vec{J} \times \vec{B} - \nabla P_e) \right], \quad (63)$$

$$\frac{\partial \vec{B}}{\partial t} = \nabla \times (\vec{u}_M \times \vec{B}) \quad (64)$$

where the α subscript has been used for the ion species and the term q_α allows for the inclusion of higher charge state ions. Furthermore,

$$\vec{u}_M = \frac{1}{en_e} \sum_{\beta} n_{\beta} q_{\beta} \vec{u}_{\beta} \quad (65)$$

is the charge averaged ion velocity and

$$\vec{J} = en_e (\vec{u}_M - \vec{u}_e) \quad (66)$$

is the current density.

For the electrons, the quasi-neutrality assumption gives,

$$n_e = \sum_{\beta} n_{\beta}, \quad (67)$$

as the electron density. Using the definition of current density presented in Equation (66) we can obtain the electron velocity. The standard fluid equation,

$$\frac{\partial P_e}{\partial t} = -\gamma \nabla \cdot (P_e \vec{u}_e) + (\gamma - 1) \vec{u}_e \cdot \nabla P_e, \quad (68)$$

is used to solve for the electron pressure. As this formulation illustrates it is not mathematically possible to cast the multifluid equations in a purely conservative formulation. Numerical techniques used for single fluid have to be adjusted to deal with this situation (Tóth et al., 2012 discuss these issues in more detail). It is also worth noting that the energy equation is only true for the hydrodynamic energy density and not the total energy density. In this system to lowest order all the species move in the perpendicular directions with the $E \times B$ velocity. As the magnetic field changes momentum can be transferred between the species in the plasma.

4.2. Incorporation of internal plasma sources in global MHD models

In addition to the solar wind plasma, there are various other sources of plasma present in planetary magnetospheres. Plasma sources internal to a planetary magnetosphere may come from the atmosphere/ionosphere, such as the ionospheric outflows at Earth (*Chappell, 2015; Welling et al., 2015* this issue) and the planetary ions produced from the exosphere at Mercury (*Raines et al., 2015* this issue). In addition, plasma sources may originate from planetary moons and this is especially the case for the gas giants, Jupiter (*Bolton et al., 2015* this issue) and Saturn (*Blanc et al., 2015* this issue). Through processes like surface warming, active plumes or surface sputtering by magnetospheric particles, moons of the giant planets may possess significant sources of neutrals. The neutrals originating from the moons can become charged particles through various mass-loading processes, thereby supplying plasma to their parent magnetospheres. It is now well known that Io and Enceladus are the major plasma sources of the magnetospheres of Jupiter and Saturn, respectively. The presence of the internal plasma sources to some degree modifies the plasma distribution and composition within the magnetosphere, and in some cases can significantly affect the configuration and dynamics of the magnetosphere. It is, therefore, important to include the internal plasma sources in modeling the structure and dynamics of planetary magnetospheres. Here we provide an overview of the various approaches adopted to incorporate internal plasma sources in global MHD models.

a) *Impact of ionospheric outflows*

The Alfvén speed in the high-latitude, low-altitude region above the ionosphere is usually very high. Therefore, including this part of the magnetosphere in global magnetosphere simulations imposes severe constraints on the allowable time step that can be used in numerically solving the MHD equations. As a result, presently most global magnetosphere models exclude this region (“gap region”) by placing their simulation inner boundaries at altitudes between a couple of and several planetary radii. The ionosphere is conventionally modeled in a separate module as a two-dimensional spherical surface where the electric potential (thus the electric field) is solved for a given distribution of height-integrated conductivity and field-aligned currents (FACs). The FACs are obtained directly from the MHD model of the magnetosphere by first

calculating the currents at or near the simulation inner boundary and then mapping them along the dipole field line down to the ionosphere. The electric field obtained from the ionosphere solver is mapped back along the field lines to the magnetosphere boundary, where the $E \times B$ drift velocity is calculated and used to set the boundary condition for plasma velocity. Given the way in which the coupling between the magnetosphere and the ionosphere is treated in present global magnetosphere models, physical processes responsible for producing the ionospheric outflows usually are not directly included in those models. In such cases, the introduction of ionospheric plasma into magnetosphere simulations typically is enabled through prescription of boundary conditions at the low-altitude boundary of the magnetosphere model, similar to the way in which the solar wind plasma is injected into the simulation domain at the sunward boundary. It is worth noting that this type of treatment does not require significant modifications to the MHD equations and is, therefore, relatively convenient in terms of numerical implementation.

Several different approaches have been adopted for adding ionospheric outflows in global MHD models. A relatively simple method is to set the plasma density to relatively high values at the inner boundary and fix it throughout a simulation run. For example, the multi-fluid MHD model by Winglee et al. (2002) specified constant densities for the light (H^+) and heavy ionospheric species (O^+) at their simulation inner boundary. Pressure gradients and/or other effects (e.g., centrifugal acceleration and numerical diffusion) may drive the ionospheric plasma to flow from the low-altitude boundary into the magnetosphere domain. As such, the ionospheric plasma is added in the simulation in a passive manner in that the outflow parameters are not explicitly set and controlled.

In contrast to the passive method described above, some global models used methods in which the outflow parameters, such as the source location, outflow density and velocity, are explicitly specified at the low-altitude boundary of the magnetosphere model. Several global modeling studies (e.g., *Wiltberger et al.*, 2010; *Garcia et al.*, 2010; *Yu and Ridley*, 2013) performed controlled global simulations to examine the effects of the outflow source location and intensity on the global magnetospheric configuration and dynamics. In these studies, ion outflows were introduced in localized regions, such as the dayside cusp or the nightside auroral zone, and the outflow rates were specified by setting the plasma density and parallel velocity in the boundary conditions.

The choice of outflow parameters may also be made based on empirical outflow models. For example, Brambles et al. (2010) incorporated in the LFM global simulation a

driven outflow model based on the empirical model by Strangeway et al. (2005), which was built upon the FAST satellite observations. The empirical model provides a scaling relation between the average outflow flux and the average earthward-flowing Poynting flux, which is calculated directly from the MHD model near the inner boundary. This approach in effect enables a two-way coupling between the magnetosphere and the ionosphere, because the outflow source location and intensity may vary in time depending on the magnetospheric conditions.

More self-consistent implementation of ionospheric outflows may be achieved by coupling a global MHD model with a physics-based ionospheric outflow model. Gloer et al. (2009) coupled the Polar Wind Outflow Model (PWOM) into the SWMF to study the effects of polar wind type outflows on the coupled magnetosphere-ionosphere system. PWOM includes important physical processes responsible for the transport and acceleration of the ionospheric gap region between the magnetosphere and ionosphere. It takes inputs from both the magnetosphere model (FACs and plasma convection pattern) and the upper atmosphere model (neutral densities and neutral winds) to calculate the upwelling and outflowing of ionospheric plasma. In return, the outflow fluxes obtained at the top boundary of the PWOM model are used to set the inner boundary conditions of the magnetosphere model.

b) *Plasma sources associated with planetary satellites*

Different from the Earth's magnetosphere where the magnetospheric plasma comes either from the solar wind or the ionosphere, the bulk of the magnetospheric plasma in the giant planet magnetospheres originate predominantly from planetary satellites. At Jupiter, the major plasma source is the volcanic moon, Io, which supplies plasmas to the Jovian magnetosphere at a rate of 260-1400 kg/s (Bagenal and Delamere, 2011). At Saturn, the dominant source of magnetospheric plasma is the icy moon, Enceladus, which produces predominantly water-group ions to the magnetosphere at a rate of 12-250 kg/s (Bagenal and Delamere, 2011). At both planets, the presence of internal plasma sources plays a crucial role in shaping the magnetosphere. It is, therefore, essential to include the internal plasma sources associated with the moons in global models of the giant planet magnetospheres.

There are, in general, two types of approaches used for incorporating plasma sources associated with moons. One relies on prescription of boundary conditions, similar to the

approach outlined above for incorporating ionospheric outflows into Earth's magnetosphere models. For example, the global MHD model by Ogino et al. (1998) which was first applied to Jupiter and later adapted to Saturn (*Fukazawa et al.*, 2007a; 2007b), does not explicitly include in the simulation domain plasma sources associated with moons. Rather, the model included the internal plasma sources by fixing plasma density and pressure in time at the inner boundary, which was placed outside of the main regions in which moon-associated plasmas are added to the systems. Similarly, in the multi-fluid MHD model applied to Saturn's magnetosphere, Kidder et al. (2009) held the densities of various plasma fluids fixed near their simulation inner boundary to mimic the addition of new plasma from Enceladus.

The other approach used in the modeling of the giant planets' magnetospheres incorporates internal plasma sources associated with moons in an explicit manner. The neutral gases emanating from the moons in the Jovian and Saturnian magnetospheres are distributed in a broad region forming plasma and neutral tori, which mass-load newly created charged particles which then modify the plasma flow in the system via electromagnetic forces (see a review by Szegő et al. (2000)). This occurs not only near the vicinities of the moons, but also over extended regions of space. It is desirable to self-consistently take into account this effect in a global magnetosphere model. This can be done by incorporating appropriate source and loss terms into the MHD equations described above. One can derive the mass-loading source terms for MHD using first-principles from the Boltzman equation (*Cravens*, 1997; *Gombosi*, 1998). Terms describing the change of the plasma phase-space distribution due to collisional processes, including ionization, charge-exchange, recombination, and elastic collisions, can be included in the Boltzman equation. Appropriate velocity moments can then be taken to obtain the source terms associated with various mass-loading processes for the continuity, momentum and energy equations of MHD. One advantage of this method over the boundary condition method is that it describes in a self-consistent way the change of mass, momentum and energy of magnetospheric plasma due to mass-loading. This approach has been used in global models of the giant planets' magnetospheres, such as the SWMF applications to Saturn's magnetosphere by Hansen et al. (2005); Jia et al. (2012); Jia and Kivelson (2012) and the global MHD model of Jupiter's magnetosphere by Chané et al. (2013).

4.3. Hybrid Models

The most common hybrid approach used in simulating space plasmas treats the ions kinetically and the electrons as a massless charge neutralizing fluid. In the hybrid regime, the density, temperatures and magnetic field is such that the ions are essentially collisionless. On the other hand the electrons have relatively small gyroradii and may undergo an order of magnitude or more collisions. Thus the electrons are described as a massless collision-dominated thermal fluid. There are finite electron mass hybrid schemes in existence, which will not be discussed here. Hybrid schemes have been around for many years thus the interested reader should see the reviews by Brecht and Thomas (1988), Lipatov (2002), Winske et al., (2003), and the references therein for historical perspectives. The most recent review is that of Ledvina et al. (2008), where the following brief description is taken from.

The hybrid approach starts with the following assumptions.

i) Quasi-neutrality is assumed,

$$n_e = \sum_i n_i \quad (69)$$

Thus the displacement current is ignored in Ampere's law (Equation (74)). This assumption is valid on scales larger than the Debye length. The assumption breaks down when the grid resolution is finer than the Debye length. This also implies that $\nabla \cdot \mathbf{J} = 0$, and removes most electrostatic instabilities.

ii) The Darwin approximation is assumed.

This approximation splits the electric field into a longitudinal part \mathbf{E}_L and a solenoidal part \mathbf{E}_T . Then $\nabla \times \mathbf{E}_L = 0$ and $\nabla \cdot \mathbf{E}_T = 0$ and $\partial \mathbf{E}_T / \partial t$ is neglected in Ampere's law (Equation (74)). This allows the light waves to be ignored. It also removes relativistic phenomena.

iii) The mass of the electrons is taken to be zero.

iv) The electrons collectively act as a fluid.

Thus the electron plasma and gyrofrequencies are removed from the calculations. This means that high frequency modes are not present, such as the electron whistler. By using these last two assumptions there is no longer a physical mechanism to describe the system behavior at small scales. The Debye length and the magnetic skin depth are not

meaningful in this scheme. This sets the limit on the cell size that should be used to at least an order of magnitude larger than the electron skin depth c/ω_{pe} . It is possible to use cell sizes less than the ion skin depth but the results are meaningless. The chosen cell size should resolve the ion kinetic effects (e. g. gyroradius and ion skin depth). If the cell size is much larger than the kinetic scales all that is accomplished is the creation of the world's most expensive MHD simulation.

With these assumptions the hybrid scheme solves the following ion momentum and position equations for each particle:

$$\frac{dv}{dt} = \frac{q}{m_i} [\mathbf{E} + \mathbf{v} \times \mathbf{B}] - \eta \mathbf{J}_{total} \quad (70)$$

$$\frac{d\mathbf{x}}{dt} = \mathbf{v} \quad (71)$$

where \mathbf{J} is the total current density and η is the plasma resistivity. The electron momentum equation can be written as:

$$\mathbf{E} = \frac{1}{n_e e} \left[(\nabla \times \mathbf{B}) \times \mathbf{B} - \mathbf{J}_i \times \mathbf{B} - \nabla (n_e T_e) + \eta \mathbf{J}_{total} \right] \quad (72)$$

With the electron temperature given by:

$$\frac{\partial T_e}{\partial t} + \mathbf{u}_e \cdot \nabla T_e + \frac{3}{2} T_e \nabla \cdot \mathbf{u}_e = \frac{2}{3 n_e} \eta \mathbf{J}_{total}^2 \quad (73)$$

Here T_e is the electron temperature and \mathbf{u}_e is the electron velocity. Note that (73) does not include the effects of thermal conduction, but that can be added if appropriate. Ampere's law becomes:

$$\nabla \times \mathbf{H} = \mathbf{J}_i + \mathbf{J}_e \quad (74)$$

where \mathbf{J}_i and \mathbf{J}_e are the ion and electron current densities. The magnetic field is obtained from Faraday's law, given below:

$$\nabla \times \mathbf{E} + \frac{\partial \mathbf{B}}{\partial t} = 0 \quad (75)$$

The electric field contains contributions from the electron pressure gradient, resistive effects and Hall currents. The scheme correctly simulates electromagnetic plasma modes up to and including the lower portion of the whistler wave spectrum (well below the electron cyclotron frequency, $\omega \ll \omega_{ce}$). Shock formation physics is included, therefore no assumptions or shock capturing techniques are needed to capture a shock. The time step is determined by the ion cyclotron frequency. This comes at the price of the loss of electron particle effects and charge separation. Some small-scale electrostatic effects can be included through the resistivity terms. The resistivity terms can also be used to stabilize the numerical scheme used to solve the equations by adding it in as a small amount of artificial resistivity.

4.4. Magnetosphere-ionosphere coupling

The ionosphere-magnetosphere coupling is not a process in itself. It is rather a chain of processes that act as a control loop between the dynamics of the ionospheric and of the magnetospheric plasmas connected by conductive magnetic field lines as shown in Figure 8. A modification of the transport in one region has consequences on the transport in the conjugate region and that affects in turn the initial transport in the first region. For example, the convection in the magnetosphere results in convection in the ionosphere (see Figure 9). The plasma dynamics in one region is constrained by the dynamics in the other. For each region, the ionosphere-magnetosphere coupling could be assimilated to some kind of interactive boundary conditions (representing the interaction with the conjugate region) that need to be solved self-consistently with the dynamics of the region considered.

In a first approach, the ionospheric plasma exhibits local-time, latitudinal, seasonal variations but forms a continuous conductive shell embedded in the high-altitude planetary atmosphere. It lies at the footprints of conductive planetary magnetic field lines that connect it to different magnetospheric regions. The polar cap magnetic field lines are open with one footprint in the polar ionosphere and the other end extended to large distances downtail, in the so-called lobes. The lobe plasma is believed to be diluted and therefore does not develop significant couplings with the ionosphere. Near the equator, the magnetic field lines remain fully embedded in the topside ionosphere and do not

reach the magnetosphere. Between the polar cap and the equatorial strip, the magnetic field lines are closed with both footprints in the ionosphere and their apex reach the magnetosphere. Near the planet, a region called “plasmasphere” filled with cold plasma of ionospheric origin in corotation with the planet may exist, as well as radiation belts with very energetic particles trapped on closed orbits around the planet. The so-called “plasma sheet” represents the main plasma reservoir in the magnetospheres of Earth, Jupiter and Saturn. The transport mechanisms differ for each planet: they involve corotation, outward diffusion from inner plasma sources or earthward convection of plasma ultimately extracted from external sources (solar wind), but all result in the formation of a dense and hot plasma sheet, confined near the equatorial plane and extending up to large distances down tail. The conductive magnetic field lines allow electric field transmission, current circulation and particle exchanges. The effects of these magnetic-field-aligned processes are enhanced when they involve dense and dynamical regions such as the ionosphere and the plasma sheet, resulting in significant consequences on the dynamics of both regions at large scales as well as at local or transient scales.

The coupled ionosphere - magnetosphere system can be described by a feedback loop derived from various investigations in the terrestrial environment (*Vasyliunas, 1970; Wolf, 1975; Harel et al., 1981; Fontaine et al., 1985; Peymirat and Fontaine, 1994*) as illustrated in **Figure 16**, where the magnetospheric plasma is indicated in the top row. External sources such as the planetary rotation or the solar wind – magnetosphere dynamo contribute to produce large-scale electric fields in the magnetosphere, which combine with the magnetospheric magnetic field to drag this magnetospheric plasma into a large-scale motion. Smaller-scale processes, instabilities, phase space diffusion processes, etc. add smaller-scale motions and contribute to the global and local plasma distribution and current circulation in the magnetosphere.

Field-aligned processes are shown in the second row of **Figure 16**. On one hand, the current closure $\nabla \cdot \mathbf{j}_M = 0$ in the magnetosphere, where \mathbf{j}_M is the magnetospheric current density, implies a current circulation along magnetic field lines j_{\parallel} down to the ionosphere. On the other hand, particles with pitch-angles smaller than the atmospheric loss cone reach the ionosphere at the footprint of magnetic field lines: they contribute to the field-aligned currents. The mirror effect due to the magnetic field line convergence limits the particle fluxes that reach the ionosphere and thus the field-aligned current density

transmitted to the ionosphere. Current-voltage relations, such as those proposed by Knight (1973) (see Equations (39) and (40)), predict that parallel potentials can develop and increase the field-aligned current density when the available precipitating fluxes cannot match the current density required by the current closure in the magnetosphere. Ionospheric particles can also escape from the ionosphere, in particular electrons which are very mobile along magnetic field lines. They carry return currents due to a favorable effect of the mirror force from the ionosphere toward the magnetosphere. It is generally difficult to measure particle outflows of ionospheric origin due to their low energy, except if they are accelerated (see *Chappell*, 2015).

The UV and EUV solar radiation contribute to create an ionospheric layer in the high-altitude atmosphere. The dynamics of the ionosphere is governed by the ionospheric Ohm's law :

$$\mathbf{j}_I = \sigma(\mathbf{E} + \mathbf{V}_n \times \mathbf{B}) \quad (76)$$

and the ionospheric current closure equation:

$$\nabla \cdot \mathbf{j}_I = 0 \quad (77)$$

where \mathbf{j}_I is the ionospheric current density, σ the ionospheric conductivity tensor, \mathbf{E}_I the electric field at ionospheric altitudes, \mathbf{V}_n the velocity of the neutral wind, \mathbf{B} the magnetic field. In addition of this solar source, the fluxes of energetic magnetospheric precipitating particles into the ionosphere contribute to produce the well-known auroral light emissions and also ionization. The resulting conductivity enhancements and the presence of field-aligned currents modify the distribution of perpendicular electric currents and electric fields at the ionospheric level (bottom row of Figure 16). This modification is finally transmitted to the magnetosphere via magnetic field lines by taking into account the eventual presence of parallel electric fields. This new electric field distribution modifies in turn the plasma transport in the magnetosphere, which closes the feedback loop.

Finally, any modification / event at large or smaller scales that occurs in one region is transmitted to the other one where it modifies its own dynamics. However, the possibilities of exchanges of particles, momentum, and energy are limited by the plasma configuration in each region. A mismatch between both regions can be overcome by the set up of field-aligned electric fields and currents, in the limit of energy density available in each region. These effects result in parallel particle acceleration and thus in light emissions when accelerated particles precipitate into the ionosphere/upper atmosphere.

2018

2019 a) *Time-varying coupling*

2020 The above description does not only apply to quasi-steady ionosphere –
2021 magnetosphere coupling, but works similarly at smaller-scales (see Lysak et al., 1990 for
2022 a review). For example, time-varying fluctuations in the magnetosphere or wave –particle
2023 interactions occurring during plasma transport may generate Alfvén waves that carry
2024 field-aligned currents. These currents close similarly through the ionosphere. They result
2025 in fluctuating effects in the ionosphere that will affect auroras, conductivities, electric
2026 fields and currents. Fluctuating conditions in the ionosphere are in turn transmitted to the
2027 magnetosphere via magnetic field lines and produce fluctuating feedback effects. The
2028 superposition of initial and feedback fluctuations can stabilize or destabilize the plasma;
2029 it can also give rise to periodic effects as pulsations, formation of multiple arcs, etc.

2030 Small-scale processes such as magnetic reconnection imply a connectivity
2031 interruption and reconfiguration for a subset of magnetic field lines in a localized region.
2032 On the reconnection time scale, field-aligned processes cannot exist because of
2033 connectivity changes and the ionosphere and magnetosphere dynamics are disconnected.
2034 This is not the case for the time periods just before and after reconnection: important
2035 effects occur in both regions, resulting in enhanced field-aligned couplings, i. e. large
2036 field-aligned particle fluxes, electric fields and currents.

2037

2038 b) *Planet-Moon interactions*

2039 The interaction of magnetized planets with moons is another example of local
2040 feedback processes. It depends on the electrical properties of the moons, or rather of the
2041 obstacle, and on the flow characteristics (for a review, see for example Kivelson, 2004).
2042 The obstacle can be the magnetic field, the atmosphere and ionosphere or the body itself
2043 depending of the radial variation of the energy density. The magnetospheric flow is
2044 coupled to the planetary ionosphere via magnetic field lines and this coupling drags the
2045 magnetospheric plasma at a speed which may differ from the moons' orbital velocity. If
2046 the flow velocity in the rest frame of the moon were super-Alfvénic, it would produce a
2047 shock wave ahead of the obstacle as in the solar wind / magnetosphere interaction. Inside
2048 magnetospheres, the interaction velocity is usually sub-Alfvénic.

2049 In the case of an insulating body, the sub-Alfvénic magnetospheric flow is absorbed
2050 by the surface, an initially empty wake appears downstream and the magnetic field

exhibits only weak perturbations. Ions can be created from various interaction processes between the magnetospheric particles and the moon, and this so-called ion pickup source contributes to the mass-loading of the magnetospheric flow.

In the case of a conducting body, the sub-Alfvénic magnetospheric flow slows upstream of the body, the planetary magnetic field lines get bent and shear Alfvén waves are launched. These waves carry field-aligned currents and they generate perturbations in the field which are known as Alfvén wings. Alfvén wings form an angle Θ_A with the initial magnetospheric magnetic field:

$$\theta_A = \tan^{-1} \left(\frac{V_M}{V_A} \right) \quad (78)$$

where V_M is the velocity of the magnetospheric flow, and V_A the Alfvén velocity.

They extend down to the planetary ionosphere which allows the current closure. This localized ionosphere – magnetosphere coupling contributes to divert the magnetospheric plasma flow around the conducting body and all along the Alfvén wings. It modifies locally the properties in the magnetically conjugated ionosphere. For example, light emissions in the ionosphere at the magnetic footprints of the Galilean moons in the Jovian magnetosphere represent the signature of this localized ionosphere – magnetosphere coupling.

In the case of a magnetized body, the moon's magnetic field creates a small magnetosphere inside the planetary magnetosphere. Up to now, Ganymede is the only known magnetized moon in the solar system. Although very small, Ganymede's magnetosphere contains features similar to terrestrial and planetary magnetospheres (e.g., *Kivelson et al.*, 1998), as the presence of a magnetopause, innermost regions protected by the internal magnetic field, and auroras (*Jia et al.*, 2009). One of the differences is that polar magnetic field lines from Ganymede's polar region connect the Jovian ionosphere at their other end. They carry field-aligned currents and contribute to a local coupling between the planetary ionosphere and the moon's magnetosphere embedded in the magnetospheric flow.

5. Summary

In this paper, the basic and common processes, related to plasma supply to each region of the planetary magnetospheres in our solar system, were reviewed. In addition to major processes related to the source, transport, energization, loss of the magnetospheric plasmas, basic equations and modeling methods, with a focus on plasma supply processes for planetary magnetospheres, are also reviewed. The topics reviewed in this paper can be summarized as follows: Source Processes related to the surface (Subsection 1.1), ionosphere (1.2), and solar wind (1.3). Section 2 is dedicated to processes related to the transport and energization of plasma such as Axford/Hines cycle (2.1), Dungey cycle (2.2), rotational driven transport and Vasyliunas cycle (2.3), field-aligned potential drop (2.4), non-adiabatic acceleration (2.5), and pick-up acceleration and mass loading (2.6). In Section 3, loss processes related to the tail reconnection and plasmoids (3.1), charge exchange (3.2), and precipitations into planets (3.3) are reviewed. Section 4 contains an overview of basic equations and modeling methods, which includes MHD simulation (4.1), incorporation of internal plasma sources in global MHD models (4.2), hybrid models (4.3), and magnetosphere-ionosphere coupling (4.4). The review provides the basic knowledge to understand various phenomena in planetary magnetospheres described in the following chapters.

Acknowledgement:

This work was partially supported by Grant-In-Aid for Scientific Research (B) 24340118 from JSPS and MEXT of Japan. KS also thanks for supports from the GEMSIS project at STEL, Nagoya University. CMJ's work at Southampton was supported by a Royal Astronomical Society Fellowship and a Science and Technology Facilities Council Ernest Rutherford Fellowship. FC is funded by JPL contract 1467206. MW is supported by NASA grants NNH12AU10I and NNH11AR82I. The National Center for Atmospheric Research is sponsored by the National Science Foundation. XJ is supported by NASA grants NNX12AK34G and NNX12AM74G, and by NSF grant AGS 1203232.

2110 **Ethical Statement:**

2111 This manuscript is prepared to submit to SSR as a review article after discussion at
2112 the ISSI workshop in 2013 and never submitted to elsewhere. Contents of this manuscript
2113 have nothing to do with the following issues:

- 2114 ▪ Disclosure of potential conflicts of interest,
- 2115 ▪ Research involving Human Participants and/or Animals,
- 2116 ▪ Informed consent.

2117

2118 **References:**

- 2119 Abe, T., et al., Observations of polar wind and thermal ion outflow by Akebono/SMS,
2120 *J. Geomagn. Geoelectr.*, 48, 319, 1996.
- 2121 Akasofu, S-I., The roles of the north-south component of the interplanetary magnetic
2122 field on large-scale auroral dynamics observed by the DMSP satellite, *Planet.*
2123 *Space Sci.* 23, 1349, 1975.
- 2124 Andersen, H., H.L. Bay, in: R. Behrisch (Ed.), *Sputtering by Particle Bombardment*
2125 *I*, Chapter 4, Springer-Verlag, Berlin, 1981.
- 2126 Andre, M., and A. L. Yau, Theories and observations of ion energization and outflow in
2127 the high latitude magnetosphere, *Space Sci. Rev.*, 80, 27, 1997.
- 2128 Ashour-Abdalla, M., et al., The formation of the wall region - Consequences in the near-
2129 Earth magnetotail, *Geophys. Res. Lett.*, 19, 1739, 1992.
- 2130 Ashour-Abdalla, M., et al., Consequences of magnetotail ion dynamics, *J. Geophys. Res.*,
2131 99, 14891, 1994.
- 2132 Anicich, V. G., Evaluated bimolecular ion-molecule gas phase kinetics of positive ions
2133 for use in modeling planetary atmospheres, cometary comae, and interstellar clouds,
2134 *Journal of Physical and Chemical Reference Data*, 22:1469–1569, 1993.
- 2135 Axford, W. I., and C. O. Hines, A unifying theory of high-latitude geophysical
2136 phenomena and geomagnetic storms, *Can. J. Phys.*, 39, 1433, 1961.
- 2137 Axford, W. I., Viscous interaction between the solar wind and the Earth's magnetosphere,
2138 *Planet. Space Sci.*, 12, 45, 1964.
- 2139 Badman, S.V., and S.W.H. Cowley, Significance of Dungey-cycle flows in Jupiter's and
2140 Saturn's magnetospheres, and their identification on closed equatorial field lines, *Ann.*
2141 *Geophys.*, 25, 94, 2007.
- 2142 Bagenal, F. and J. D. Sullivan, Direct plasma measurements in the Io torus and inner
2143 magnetosphere of Jupiter, *J. Geophys. Res.*, 86, 8447, 1981.
- 2144 Bagenal, F., The magnetosphere of Jupiter: Coupling the equator to the poles, *J.*
2145 *Atmos. Sol. Terr. Phys.*, 69, 387, doi:10.1016/j.jastp.2006.08.012, 2007.
- 2146 Bagenal, F., and P. A. Delamere, Flow of mass and energy in the magnetospheres of
2147 Jupiter and Saturn, *J. Geophys. Res.*, 116, A05209, doi:10.1029/2010JA016294, 2001.
- 2148 Banks, P. M., and T. E. Holzer, High-latitude plasma transport: The polar wind, *J.*
2149 *Geophys. Res.*, 74, 6317, doi:10.1029/JA074i026p06317, 1969.
- 2150 Baragiola, R.A., et al., *Nucl. Instrum. Meth. Phys. Res., B* 209, 294, 2003.
- 2151 Behrisch, R., and W. Eckstein, *Sputtering by particle bombardment: experiments and*
2152 *computer calculations from threshold to MeV energies*, Springer, Berlin, 2007.
- 2153 Bhardwaj, A., and G. R. Gladstone, Auroral emissions of the giant planets, *Rev.*
2154 *Geophysics*, 38, 295, 2000.
- 2155 Biersack, J.P., and Eckstein, W, Sputtering of solids with the Monte Carlo
2156 program TRIM.SP. *Appl. Phys. A* 34, 73, 1984.
- 2157 Bird, G. A., *Molecular Gas Dynamics and the Direct Simulation of Gas Flows*,
2158 Clarendon Press, Oxford, 1994.
- 2159 Birkeland, K., Sur la déviabilité magnétique des rayons corpusculaires provenant du
2160 Soleil, *C.R. Acad. Sci.*, 150, 246, 1910.
- 2161 Bolton, S. J., Jupiter's inner radiation belts, in *"Jupiter : The Planet, Satellites,*
2162 *and Magnetosphere*, F. Bagenal et al. eds., Cambridge Univ. Press, Chapter 27, 671,
2163 2004.
- 2164 Bonfond, B., When Moons Create Aurora: The Satellite Footprints on Giant Planets,
2165 *in Auroral Phenomenology and Magnetospheric Processes: Earth and Other Planets*,

2166 AGU Geophysical Monograph Series 197, 133, 2012.
 2167 Boring, J. W., et al., Sputtering of solid SO₂. *Nucl. Instrum. Methods B 1*, 321, 1984.
 2168 Borovsky, J. E., M. F. Thomnsen, and R. C. Elphic, The driving of the plasma sheet by
 2169 the solar wind, *J. Geophys. Res.*, *103*(A8), 17,617, doi:10.1029/97JA02986, 1998.
 2170 Borovsky, J. E., et al., What determines the reconnection rate at the dayside
 2171 magnetosphere?, *J. Geophys. Res.*, *113*, A07210, doi:10.1029/2007JA012645, 2008.
 2172 Brambles, O. J., et al., Effects of causally driven cusp O⁺ outflow on the storm time
 2173 magnetosphere-ionosphere system using a multifluid global simulation, *J. Geophys.*
 2174 *Res.*, *115*, A00J04, doi:10.1029/2010JA015469, 2010.
 2175 Brecht, S. H., and V. A. Thomas, Multidimensional simulations using hybrid particle
 2176 codes, *Comput. Phys. Commun.* *48*, 135143, 1988.
 2177 Brice, N. M., and G. A. Ioannidis, The magnetospheres of Jupiter and Earth, *Icarus*, *13*,
 2178 173, 1970.
 2179 Brown, D. G., J. L. Horwitz, and G. R. Wilson, Synergistic effects of hot plasma-
 2180 driven potentials and wave-driven ion heating on auroral ionospheric plasma transport,
 2181 *J. Geophys. Res.*, *100*, 17,499, 1995.
 2182 Brown, W. L., and Johnson, R. E., Sputtering of Ices: A Review, *Nucl. Inst. and*
 2183 *Meth.*, *B13*, 295, 1986.
 2184 Brown, W. L., Augustyniak, W. M., Marcantonio, K. J., Simmons, E. N., Boring, J.
 2185 W., Johnson, R. E., and Reimann, C. T., Electronic sputtering of low temperature
 2186 molecular solids, *Nucl. Instrum. Methods Phys. Res.*, *B 1*, 307, 1984.
 2187 Bruno, M., G. Cremonese, and S. Marchi, Neutral sodium atoms release from the
 2188 surfaces of the Moon and Mercury induced by meteoroid impacts, *Plan. Space Sci.*,
 2189 *55*, 1494, 2007.
 2190 Burch, J. L., et al., Properties of local plasma injections in Saturn's magnetosphere,
 2191 *Geophys. Res. Lett.*, *32*, L14S02, doi:10.1029/2005GRL022611, 2005.
 2192 Büchner, J., and L. M. Zelenyi, Regular and chaotic charged particle motion in
 2193 magnetotaillike field reversals : 1. Basic theory of trapped motion, *J. Geophys. Res.*,
 2194 *94*, 11,821, 1989.
 2195 Burkhart, G. R., and J. Chen, Differential memory in the Earth's magnetotail, *J. Geophys.*
 2196 *Res.*, *96*, 14,033, 1991.
 2197 Burlaga, L.F., Magnetic fields and plasmas in the inner heliosphere: Helios results,
 2198 *Planet. Space Sci.*, *49* 1619, 2001.
 2199 Carlson C. W., R. F. Pfaff, J. G. Watzin, Fast Auroral Snapshot (FAST) mission,
 2200 *Geophys. Res. Let.*, *25*, 2013, 1998.
 2201 Cassidy, T.A., et al., , Radiolysis and photolysis of icy satellite surfaces: experiments and
 2202 theory, *Space Science Reviews*, *153* (1–4), 299, 2010.^[SEP]
 2203 Cassidy, T.A., et al., The spatial morphology of Europa's near-surface O₂ atmosphere,
 2204 *Icarus*, *191*, 755, 2007.
 2205 Cassidy, T.A., et al., Magnetospheric ion sputtering and water ice ^[SEP]grain size at Europa.
 2206 *Planet. Space Sci.* *77*, 64, 2013.
 2207 Cecconi, B., L., et al., Goniopolarimetric study of the Rev 29 perikrone using the
 2208 Cassini/RPWS/HFR radio receiver, *J. Geophys. Res.*, *114*, A03215, 2009.
 2209 Chan'é, E., J. Saur, and S. Poedts, Modeling Jupiter's magnetosphere: Influence of
 2210 the internal sources, *J. Geophys. Res.*, *118*, 2157, doi:10.1002/jgra.50258, 2013.
 2211 Chen, F. F., *Introduction to Plasma Physics and Controlled Fusion*, Boom Konin-
 2212 klijke Uitgevers, 1984.
 2213 Chen, J., and P. J. Palmadesso, Chaos and nonlinear dynamics of single-particle orbits
 2214 in magnetotaillike magnetic field, *J. Geophys. Res.*, *91*, 1499, 1986.

2215 Chiu Y. T. and M. Schulz, Self-consistent particle and parallel electrostatic electric
 2216 field distributions in the magnetospheric-ionospheric auroral region, *J. Geophys. Res.*,
 2217 83, 629, 1978.
 2218 Cintala, M. J., Impact induced thermal effects in the lunar and Mercurian regoliths, *J.*
 2219 *Geophys. Res.*, 97, 947, 1992.
 2220 Cladis, J. B., Parallel acceleration and transport of ions from polar ionosphere to plasma
 2221 sheet, *Geophys. Res. Lett.*, 13, 893, 1986.
 2222 Clarke, J. T., *Auroral Processes on Jupiter and Saturn*, in *Auroral Phenomenology and*
 2223 *Magnetospheric Processes: Earth and Other Planets*, AGU Geophysical Monograph
 2224 Series 197, 113, 2012.
 2225 Connerney, J. E. P., et al., Images of Excited H³⁺ at the Foot of the Io Flux Tube in
 2226 Jupiter's Atmosphere, *Science*, 262, 1035-1038, 1993.
 2227 Connerney, J. E. P. and J. H. Waite, New model of Saturn's ionosphere with an influx of
 2228 water, *Nature*, 312, 136, 1984.
 2229 Cooper, J.F., et al., Energetic ion and electron irradiation of the icy Galilean satellites,
 2230 *Icarus*, 149, 133, 2001.
 2231 Cowley, S. W. H., The causes of convection in the Earth's magnetosphere: A review
 2232 of developments during the IMS, *Rev. Geophys.*, 20(3), 531–
 2233 565, doi:10.1029/RG020i003p00531, 1982.
 2234 Cowley, S. W. H., E. J. Bunce, and R. Prangé, Saturn's polar ionospheric flows and their
 2235 relation to the main auroral oval, *Ann. Geophys.*, 22, 1379, 2004.
 2236 Cravens, T. E., *Physics of Solar System Plasmas*, *Camb. Univ. Press*, DOI:
 2237 10.1017/CBO9780511529467, 1997.
 2238 De Keyser J., R. Maggiolo, M. Echim, Monopolar and bipolar auroral electric fields and
 2239 their effects, *Ann. Geophys.*, 28, 2027, 2010.
 2240 De Vries, A.E., et al., Synthesis and sputtering of newly formed molecules by
 2241 kiloelectronvolt ions. *Journal of Physical Chemistry* 88, 4510, 1984.
 2242 Delamere, P. A., and F. Bagenal, Solar wind interaction with Jupiter's magnetosphere, *J.*
 2243 *Geophys. Res.*, 115, A10201, doi:10.1029/2010JA015347, 2010.
 2244 Delamere, P. A., et al., Magnetic signatures of Kelvin-Helmholtz vortices on Saturn's
 2245 magnetopause: Global survey, *J. Geophys. Res.*, 118, 393, 2013.
 2246 Delcourt, D. C., and J.-A. Sauvaud, Populating of the cusp and boundary layers by
 2247 energetic (hundreds of keV) equatorial particles, *J. Geophys. Res.*, 104, 22,635, 1999.
 2248 Delcourt, D. C., J.-A. Sauvaud, and A. Pedersen, Dynamics of single-particle orbits
 2249 during substorm expansion phase, *J. Geophys. Res.*, 95, 20,853 1990.
 2250 Delcourt, D. C., et al., On the nonadiabatic precipitation of ions from the near-Earth
 2251 plasma sheet, *J. Geophys. Res.*, 101, 17,409, 1996.
 2252 Delcourt, D. C., Particle acceleration by inductive electric fields in the inner
 2253 magnetosphere, *J. Atm. Solar Ter. Phys.*, 64, 551, 2002.
 2254 Delcourt, D. C., R. F. Martin Jr., and F. Alem, A simple model of magnetic moment
 2255 scattering in a field reversal, *Geophys. Res. Lett.*, 21, 1543, 1994.
 2256 DiBraccio, G. A., J. A. Slavin, S. A. Boardsen, B. J. Anderson, H. Korth, T. H.
 2257 Zurbuchen, J. M. Raines, D. N. Baker, R. L. McNutt Jr., and S. C. Solomon,
 2258 MESSENGER observations of magnetopause structure and dynamics at Mercury, *J.*
 2259 *Geophys. Res.*, 118, 997, doi:10.1002/jgra.50123, 2013.
 2260 Eckstein, W., and Urbassek, H.M., Computer simulation of the sputtering process, in
 2261 *Sputtering by particle bombardment: experiments and computer calculations from*
 2262 *threshold to MeV energies*, R. Behrisch, and W. Eckstein (edt.). Springer, Berlin,
 2263 pp. 21, 2007.

2264 Eichhorn, G., Heating and vaporization during hypervelocity particle impact, *Planet.*
 2265 *Space Sci.*, 26, 463, 1978a.
 2266 Eichhorn, G., Primary velocity dependence of impact ejecta param, S bursts and the
 2267 Jupiter ionospheric Alfvén resonator, *J. Geophys. Res.*, 111, A06212, 2006.
 2268 Ergun, R. E., et al., S bursts and the Jupiter ionospheric Alfvén resonator, *J. Geophys.*
 2269 *Res.*, 111, A06212, 2006.
 2270 Evans D. S., precipitation electron fluxes formed by magnetic-field-aligned potential
 2271 differences, *J. Geophys. Res.*, 79, 2853, 1974.
 2272 Famà, M., Shi, J., Baragiola, R.A., Sputtering of ice by low-energy ions. *Surf. Sci.*
 2273 602, 156, 2008.
 2274 Feldstein, Y. I., et al., Structure of the auroral precipitation region in the dawn
 2275 sector: relationship to convection reversal boundaries and field-aligned currents, *Ann.*
 2276 *Geophys.*, 19, 495, 2001.
 2277 Fok, M.-C., et al., *J. Geophys. Res.*, 111, doi:10.1029/2006JA011839, 2006.
 2278 Fontaine D., et al., Numerical simulation of the magnetospheric convection including the
 2279 effect of electron precipitation, *J. Geophys. Res.*, 90, 8343, 1985.
 2280 Forsyth, R. J., et al., The underlying Parker spiral structure in the Ulysses magnetic field
 2281 observations, 1990–1994, *J. Geophys. Res.*, 101, 395, 1996.
 2282 Frank, L. A., On the extraterrestrial ring current during geomagnetic storm, *J. Geophys.*
 2283 *Res.*, 72, 3753, 1967.
 2284 Frederick-Frost, K. M., et al., SERSIO: Svalbard EISCAT rocket study of ion outflows, *J.*
 2285 *Geophys. Res.*, 112, A08307, doi:10.1029/2006JA011942, 2007.
 2286 Fukazawa, K., T. Ogino, and R. J. Walker, Magnetospheric convection at Saturn as
 2287 a function of IMF Bz, *Geophys. Res. Lett.*, 34 (1), doi:10.1029/2006GL028373, 2007a.
 2288 Fukazawa, K., T. Ogino, and R. J. Walker, Vortex-associated reconnection for northward
 2289 IMF in the Kronian magnetosphere, *Geophys. Res. Lett.*, 34, doi:
 2290 10.1029/2007GL031784, 2007b.
 2291 Galopeau, P., P. Zarka, and D. Le Quéau, Source location of SKR : the Kelvin-
 2292 Helmholtz instability hypothesis, *J. Geophys. Res.*, 100, 26397, 1995.
 2293 Ganguli, S. B., The polar wind, *Rev. Geophys.*, 34, 311, 1996.
 2294 Garcia, K. S., V. G. Merkin, and W. J. Hughes, Effects of nightside O⁺ outflow
 2295 on magnetospheric dynamics: Results of multifluid MHD modeling, *J. Geophys. Res.*,
 2296 115, A00J09, doi:10.1029/2010JA015730, 2010.
 2297 Glocer, A., G. Tóth, T. Gombosi, and D. Welling, Modeling ionospheric outflows and
 2298 their impact on the magnetosphere, initial results, *J. Geophys. Res.*, 114 (A), 05,216,
 2299 doi:10.1029/2009JA014053, 2009.
 2300 Gombosi, T. I., *Physics of the Space Environment*, Cambridge University Press, 1998.
 2301 Gosling, J. T., et al., The electron edge of the low latitude boundary layer during
 2302 accelerated flow events, *Geophys. Res. Lett.*, 17(11), 1833, 1990a.
 2303 Grocott, A., et al., Magnetosonic Mach number dependence of the efficiency of
 2304 reconnection between planetary and interplanetary magnetic fields, *J. Geophys. Res.*
 2305 114, A07219. doi:10.1029/2009JA014330, 2009.
 2306 Grocott, A., S. W. H. Cowley, and J. B. Sigwarth, Ionospheric flow during extended
 2307 intervals of northward but By-dominated IMF, *Ann. Geophys.*, 21, 509, 2003.
 2308 Hamilton, D. C., et al., Ring current development during the great geomagnetic storm of
 2309 February 1986, *J. Geophys. Res.*, 93, 14,343, 1988.
 2310 Hansen, K. C., et al., Global MHD simulations of Saturn’s magnetosphere at the time of
 2311 Cassini approach, *Geophys. Res. Lett.*, 32, L20S06, doi:10.1029/2005GL022835, 2005.
 2312 Jia, X., and M. G. Kivelson, Driving Saturn’s magnetospheric periodicities from the

2313 upper atmosphere/ionosphere: Magnetotail response to dual sources, *J. Geophys. Res.*,
 2314 117, A11219, doi:10.1029/2012JA018183, 2012.
 2315 Harel M., et al., Quantitative simulations of a magnetospheric substorm, 1. Model logic
 2316 and overview, *J. Geophys. Res.*, 86, 2217-2241, 1981.
 2317 Haring, R.A., et al., Reactive sputtering of simple condensed gases by keV ions. III.
 2318 Kinetic energy distributions, *Nucl. Instrum. Methods B* 5, 483, 1984.
 2319 Harris, E.G., On a plasma sheath separating regions of oppositely directed magnetic
 2320 fields, *Nuovo Cimento*, 23, 115, 1962.
 2321 Hasegawa, H., et al., Transport of solar wind into Earth's magnetosphere through rolled-
 2322 up Kelvin-Helmholtz vortices, *Nature*, 430(7001), 755, doi: 10.1038/nature02799,
 2323 2004.
 2324 Hasegawa, H., et al., Kelvin-Helmholtz waves at the Earth's magnetopause:
 2325 Multiscale development and associated reconnection, *J. Geophys. Res.*, 114, A12207,
 2326 2009.
 2327 Heikkila, W. J., and R. J. Pellinen, Localized induced electric field within the magnetotail,
 2328 *J. Geophys. Res.*, 82, 1610, 1977.
 2329 Hess, S., P. Zarka, and F. Mottez, Io-Jupiter interaction, millisecond bursts and field
 2330 aligned potentials, *Planet. Space Sci.*, 55, 89, 2007.
 2331 Hess, S., P., et al., Electric potential jumps in the Io-Jupiter Flux tube, *Planet. Space Sci.*,
 2332 57, 23, 2009.
 2333 Hill, T. W. and F. C. Michel, Heavy ions from the Galilean satellites and the
 2334 centrifugal distortion of the Jovian magnetosphere, *J. Geophys. Res.*, 81, 4561, 1976.
 2335 Hill, T. W., et al., Evidence for rotationally-driven plasma transport in Saturn's
 2336 magnetosphere. *Geophys. Res. Lett.* 32, L41S10, 2005.
 2337 Hill, T. W., A. J. Dessler, F. C. Michel, Configuration of the Jovian magnetosphere,
 2338 *Geophys. Res. Lett.*, 1., doi: 10.1029/GL001i001p00003, 1974.
 2339 Hofer, W.O., Angular, energy, and mass distribution of sputtered particles. In:
 2340 Behrisch, R., Wittmaack, K. (Eds.), *Sputtering by Particle Bombardment*,
 2341 Springer, Berlin, pp. 15, 1991.
 2342 Hones, E.W., Jr., The magnetotail: Its generation and dissipation, in *Physics of Solar*
 2343 *Planetary Environments*, ed. by D.J. Williams, pp. 559-571, AGU, Washington, D.C.,
 2344 1976.
 2345 Hones, E.W., Jr., Substorm processes in the magnetotail: comments on "On hot tenuous
 2346 plasma, fireballs, and boundary layers in the Earth's magnetotail" by L.A. Frank et al.,
 2347 *J. Geophys. Res.* 82, 5633, 1977.
 2348 Horwitz, J. L., et al., Centrifugal acceleration of the polar wind, *J. Geophys. Res.*, 99,
 2349 15,051, 1994.
 2350 Huang, T. S. and T. J. Birmingham, The polarization electric field and its effects in an
 2351 anisotropic, rotating magnetospheric plasma, *J. Geophys. Res.*, 97, 1511, 1992.
 2352 Huba, J. D., *Numerical Methods: Ideal and Hall MHD*, 7, 26, 2005.
 2353 Huff, R. L., et al., Mapping of Auroral Kilometric Radiation Sources to the Aurora, *J.*
 2354 *Geophys. Res.*, 93, 11445, 1988.
 2355 Ieda, A., et al., Statistical analysis of the plasmoid evolution with Geotail observations, *J.*
 2356 *Geophys. Res.*, 103(A3), 4453, doi:10.1029/97JA03240, 1998.
 2357 Imber, S. M., et al., MESSENGER Observations of Large Dayside Flux Transfer Events:
 2358 Do They Drive Mercury's Substorm Cycle?, submitted to *J. Geophys. Res.*, 2014.
 2359 Ipavich, F. M., et al., Energetic (greater than 100 keV) O(+) ions in the plasma sheet,
 2360 *Geophys. Res. Lett.*, 11, 504, 1984.
 2361 Jackman, C. M., J. A. Slavin, and S. W. H. Cowley, Cassini observations of

2362 plasmoid structure and dynamics: Implications for the role of magnetic reconnection
 2363 in magnetospheric circulation at Saturn, *J. Geophys. Res.*, *116*,
 2364 A10212, doi:10.1029/2011JA016682, 2011.

2365 Jackman, C. M., et al., Interplanetary magnetic field at ~9 AU during the declining phase
 2366 of the solar cycle and its implications for Saturn's magnetospheric dynamics, *J.*
 2367 *Geophys. Res.*, *109*, A11203, doi:10.1029/2004JA010614, 2004.

2368 Jackman, C. M., R. J. Forsyth, and M. K. Dougherty, The overall configuration of
 2369 the interplanetary magnetic field upstream of Saturn as revealed by
 2370 Cassini observations, *J. Geophys. Res.*, *113*, A08114, doi:10.1029/2008JA013083,
 2371 2008.

2372 Jackman, C.M., et al., Strong rapid dipolarizations in Saturn's magnetotail: In
 2373 situ evidence of reconnection, *Geophys. Res. Lett.*, *34*, (11). L11203, 2007.

2374 Jackman, C.M., et al., Large-scale structure and dynamics of the magnetotails of Mercury,
 2375 Earth, Jupiter and Saturn, *Space Sci. Rev.*, *182*, 1, 85-154, Doi: 10.1007/s11214-014-
 2376 0060-8, 2014a.

2377 Jackman, C.M., et al., Saturn's dynamic magnetotail: A comprehensive magnetic field
 2378 and plasma survey of plasmoids and travelling compression regions, and their role in
 2379 global magnetospheric dynamics, *J. Geophys. Res.*, *119*, 5465–5494,
 2380 doi:10.1002/2013JA019388, 2014b.

2381 Jia, X. Z., et al., Properties of Ganymede's magnetosphere inferred from improved three-
 2382 dimensional MHD simulations, *J. Geophys. Res.*, *114*, A09209, doi :
 2383 10.1029/2009JA014375, 2009.

2384 Jia, X., et al., Magnetospheric configuration and dynamics of Saturn's magnetosphere: A
 2385 global MHD simulation, *J. Geophys. Res.*, *117*, A05225, doi:10.1029/2012JA017575,
 2386 2012.

2387 Jia, X. and M. G. Kivelson, Driving Saturn's magnetospheric periodicities from the
 2388 atmosphere/ionosphere: Magnetotail response to dual sources, *J. Geophys. Res.*, *117*,
 2389 A11219, doi:10.1029/2012JA018183, 2012.

2390 Kidder, A., R. M. Winglee, and E. M. Harnett, Regulation of the centrifugal interchange
 2391 cycle in Saturn's inner magnetosphere, *J. Geophys. Res.*, *114*, A02205,
 2392 doi:10.1029/2008JA013100, 2009.

2393 Johnson, R.E. 1998. Sputtering and Desorption from Icy Surfaces, in *Solar System^[1] Ices*,
 2394 ed, B. Schmitt and C. beBergh, Kluwer Acad. Pub., Netherlands,. 303, 1998.

2395 Johnson, R.E., Energetic charged-particle interactions with atmospheres and
 2396 surfaces. *Energetic Charged-Particle Interactions with Atmospheres and Surfaces*,
 2397 vol. X. Springer-Verlag, Berlin, Heidelberg, New York, *Phys. Chem. Space*, *19*, 1990.

2398 Johnson, R.E., Surface chemistry in the Jovian magnetosphere radiation environment.
 2399 In: Dessler, R. (Ed.), *Chemical Dynamics in Extreme Environments*, *Adv. Ser.*
 2400 *Phys. Chem.*, World Scientific, Singapore 11, pp. 390, Chapter 8, 2001.

2401 Johnson, R.E., M.H. Burger, T.A. Cassidy, F. Leblanc, M. Marconi, W.H. Smyth. 2009.
 2402 Composition and detection of Europa's sutter-induced atmosphere, in . *Europa*, eds.
 2403 Pappalardo, R.T. McKinnon, W.B., Khurana, K.K. U. of , Interaction of Mercury with
 2404 the solar wind, *Icarus*, *143*, 2, 397, 2000.

2405 Kabin, K., et al., Interaction of Mercury with the solar wind, *Icarus*, *143*, 2, 397, 2000.

2406 Keiling, A., et al., Transient ion beamlet injections into spatially separated PSBL flux
 2407 tubes observed by Cluster-CIS, *Geophys. Res. Lett.*, *31*, 2004.

2408 Khurana, K. K., et al., The origin of Ganymede's polar caps, *Icarus*, *191*, 193, 2007.

2409 Kidder, A., R. M. Winglee, and E. M. Harnett, Regulation of the centrifugal interchange
 2410 cycle in Saturn's inner magnetosphere, *J. Geophys. Res.*, *114*, A02205,

doi:10.1029/2008JA013100, 2009.

Killen, R., and Ip, ???

Killen, R., et al., Processes that Promote and Deplete the Exosphere of Mercury, *Space Sci. Rev.*, *132*, 433, 2007

Kim, Y. H., et al., Hydrocarbon ions in the lower ionosphere of Saturn, *J. Geophys. Res.*, *119*, 384, 2014.

Kitamura, N., et al., Photoelectron flows in the polar wind during geomagnetically quiet periods, *J. Geophys. Res.*, *117*, A07214, doi:10.1029/2011JA017459, 2012.

Kivelson, M. G., et al., Intermittent short-duration magnetic field anomalies in the Io torus: Evidence for plasma interchange? *Geophys. Res. Lett.*, *24*, 2127, 1997.

Kivelson, M. G., et al., Ganymede's magnetosphere: Magnetometer overview, *J. Geophys. Res.*, *103*, 19963, 1998.

Kivelson M. G., et al., Moon-magnetosphere interaction: a tutorial, *Adv. Space Res.*, *33*, 2061, 2004.

Knight S., Parallel electric fields, *Planet. Space. Sci.*, *21*, 741, 1973.

Krall, N. A., and A. W. Trivelpiece, *Principles of Plasma Physics*, San Francisco Press, Incorporated, San Francisco, 1986.

Krimigis, S. M., et al., Dynamics of Saturn's Magnetosphere from MIMI During Cassini's Orbital Insertion, *Science*, *307*, 1270, 2005.

Kronberg, E. A., et al., Comparison of periodic substorms at Jupiter and Earth, *J. Geophys. Res.*, *113*, A04212, doi:10.1029/2007JA012880, 2008.

Krupp, N. A., et al., Global flows of energetic ions in Jupiter's equatorial plane: First-order approximation, *J. Geophys. Res.* *106*, 26,017, doi:10.1029/2000JA900138, 2001.

Krupp, N. A., et al., Dynamics of the Jovian Magnetosphere , in *Jupiter : The Planet, Satellites, and Magnetosphere*, F. Bagenal et al. eds., Cambridge Univ. Press, Chapter 25, 617, 2004.

Lagg, A., et al., In situ observations of a neutral gas torus at Europa, *Geophys. Res. Lett.* *30*, 110000, 2003.

Lai, H. R., et al., Reconnection at the magnetopause of Saturn: Perspective from FTE occurrence and magnetosphere size, *J. Geophys. Res.* *117*, A05222, doi:10.1029/2011JA017263, 2012.

Ledvina, S. A., Y. -J. Ma, and E. Kallio, Modeling and Simulating Flowing Plasmas and Related Phenomena, *Space Sci. Rev.*, *139*, 143189, doi:10.1007/s11214-008-9384-6, 2008.

Lipatov, A., *The Hybrid Multiscale Simulation Technology*, Springer, Berlin, 2002.

Louarn, P., et al., Trapped electrons as a free energy source for auroral kilometric radiation, *J. Geophys. Res.*, *95*, 5983, 1990.

Luhmann, J. G., et al., A model of the ionosphere of Saturn's rings and its implications, *Icarus*, *181*, 465, 2006.

Lyon, J. G., J. A. Fedder, and C. M. Mobarry, The Lyon-Fedder-Mobarry (LFM) global MHD magnetospheric simulation code, *J. Atmos. Solar Terr. Phys.*, *66*, 1333, doi:10.1016/j.jastp.2004.03.020, 2004.

Lyons L. R. , Generation of large-scale regions of auroral currents, electric potentials, and precipitation by the divergence of the convection electric field, *J. Geophys. Res.*, *85*, 17, 1980.

Lysak R., Electrodynamic couplig of the ionosphere and magnetosphere, *Space Sci. Review*, *52*, 33, 1990.

Majeed, T., and J. C. McConnell, Voyager electron density measurements on Saturn: Analysis with a time dependent ionospheric model, *J. Geophys. Res.*, *101*, 7589,

2460 DOI:10.1029/96JE00115, 1996.
 2461 Mangano, V., et al., The contribution of impact-generated vapour to the hermean
 2462 atmosphere, *Planet. Space Sci.* 55(11) 1541, 2007.
 2463 Marconi, M.L., A kinetic model of Ganymede's atmosphere, *Icarus*, 190 155, 2007.
 2464 Marklund G. T., Electric fields and plasma processes in the auroral downward current
 2465 region, below, within, and above the acceleration region, *Space Sci. Rev.*, 142, 1,
 2466 doi 10.1007/s11214-008-9373-9, 2009.
 2467 Masters, A., et al., Surface waves on Saturn's dawn flank magnetopause driven by
 2468 the Kelvin-Helmholtz instability, *Planet. Space Sci.*, 57,
 2469 1769, doi:10.1016/j.pss.2009.02.010, 2009.
 2470 Masters, A., et al., Cassini observations of a Kelvin-Helmholtz vortex in Saturn's
 2471 outer magnetosphere, *J. Geophys. Res.*, 115(A7), A07225, doi:10.1029/2010JA015351,
 2472 2010.
 2473 Masters, A., et al., The importance of plasma b conditions for magnetic reconnection at
 2474 Saturn's magnetopause, *Geophys. Res. Lett.*, 39, L08103, doi:10.1029/2012GL051372,
 2475 2012.
 2476 Masters, A., et al., The importance of plasma b conditions for magnetic reconnection at
 2477 Saturn's magnetopause, *Geophys. Res. Lett.*, 39, L08103, doi:10.1029/2012GL051372,
 2478 2012.
 2479 Matsumoto, Y., and K. Seki, Formation of a broad plasma turbulent layer by forward
 2480 and inverse energy cascades of the Kelvin-Helmholtz instability, *J. Geophys. Res.*,
 2481 115, A10231, doi:10.1029/2009JA014637, 2010.
 2482 Matsumoto, Y., and M. Hoshino, Turbulent mixing and transport of collisionless
 2483 plasmas across a stratified velocity shear layer, *J. Geophys. Res.*, 111,
 2484 A05213, doi:10.1029/2004JA010988, 2006.
 2485 Mauk, B.H., et al., Energetic neutral atoms from a trans-Europa gas torus at Jupiter,
 2486 *Nature*, 421 920, 2003.
 2487 Mauk, B.H., Quantitative modeling of the "convection surge" mechanism of
 2488 ion acceleration, *J. Geophys. Res.*, 91, 13,423, 1986.
 2489 McAndrews, H. J., et al., Evidence for reconnection at Saturn's magnetopause, *J.*
 2490 *Geophys. Res.*, 113, A04210, doi:10.1029/2007JA012581, 2008.
 2491 McAndrews, H. J., et al., Evidence for reconnection at Saturn's magnetopause, *J.*
 2492 *Geophys. Res.*, 113, A04210, doi:10.1029/2007JA012581, 2008.
 2493 McElroy, M. B., The ionospheres of the major planets, *Space Sci. Rev.*, 14, 460, 1973.
 2494 McFadden, J., C. Carlson and R. Ergun, Microstructure of the auroral acceleration region
 2495 as observed by FAST, *J. Geophys. Res.*, 104(A7), 14453, doi:10.1029/1998JA900167,
 2496 1999.
 2497 McNutt, R. L. Jr., et al., Departure from rigid co-rotation of plasma in Jupiter's dayside
 2498 magnetosphere, *Nature*, 280, 803, 1979.
 2499 Meyer-Vernet, N., M. Moncuquet and S. Hoang, Temperature inversion in the Io plasma
 2500 torus, *Icarus* 116, 202, 1995.
 2501 Michel, F. C., and P. A. Sturrock, Centrifugal instability of the Jovian magnetosphere and
 2502 its interaction with the solar wind, *Planet. Space Sci.*, 22, 1501, 1974.
 2503 Mitchell, D. G., et al., Current carriers in the near-earth cross-tail current sheet during
 2504 substorm growth phase, *Geophys. Res. Lett.*, 17, 583-586, 1990.
 2505 Mitchell, D. G., et al., Global imaging of O+ from IMAGE HENA, *Space Sci. Rev.*, 109,
 2506 63, 2003.
 2507 Moore, T. E., and J. L. Horwitz, Stellar ablation of planetary atmospheres, *Rev.*
 2508 *Geophys.*, 45, RG3002, doi:10.1029/2005RG000194, 2007.

2509 Mottez, F. and V. Génot, Electron acceleration by an Alfvénic pulse propagating in an
 2510 auroral plasma cavity, *J. Geophys. Res.*, *116*, A00K15, 2011.
 2511 Mozer F. S. and A. Hull, Origin and geometry of upward parallel electric fields in the
 2512 auroral acceleration region, *J. Geophys. Res.*, *106*, 5763, 2001.
 2513 Mozer F. S., et al., Satellite measurements and theories of low altitude auroral particle
 2514 acceleration, *Space Sci. Rev.*, *27*, 155, 1980.
 2515 Mozer, F. S., et al., Observations of paired electrostatic shocks in the
 2516 polar magnetosphere, *Phys. Rev. Lett.*, *38*, 292, 1977.
 2517 Müller, M., et al., Estimation of the dust flux near Mercury. *Planet. Space. Sci.*, *50*, 1101,
 2518 2002.
 2519 Mura, A., et al., The sodium exosphere of Mercury: Comparison between observations
 2520 during Mercury's transit and model results, *Icarus* *200*, 1, 2009.
 2521 Nagy, A. F., T. E. Cravens, S. G. Smith, H. A. Taylor Jr., and H. C. Brinton, Model
 2522 calculations of the dayside ionosphere of Venus: Ionic composition, *J. Geophys. Res.*,
 2523 *85*, 7795–7801, 1980.
 2524 Nakamura, T. K. M., M. Fujimoto, and A. Otto, Structure of an MHD-scale Kelvin–
 2525 Helmholtz vortex: Two-dimensional two-fluid simulations including finite electron
 2526 inertial effects, *J. Geophys. Res.*, *113*, A09204, doi:10.1029/2007JA012803, 2008.
 2527 Neishtadt, A. I., On the change in the adiabatic invariant on crossing a separatrix in
 2528 systems with two degrees of freedom, *J. Appl. Math.*, *51*, 586, 1987.
 2529 Newell, P. T., et al., Characterizing the state of the magnetosphere: Testing the ion
 2530 precipitation maxima latitude (b2i) and the ion isotropy boundary, *J. Geophys. Res.*,
 2531 *103*, 4739, 1998.
 2532 Nichols, J.D., S.W.H. Cowley, D.J. McComas, Magnetopause reconnection rate estimates
 2533 for Jupiter's magnetosphere based on interplanetary measurements at ~5AU,
 2534 *Ann. Geophys.*, *24*, 393, 2006.
 2535 Norqvist, P., et al., Ion cyclotron heating in the dayside magnetosphere, *J. Geophys. Res.*,
 2536 *101*, 13,179, 1996.
 2537 Northrop, T. G. and J. R. Hill, Stability of negatively charged dust grains in Saturn's ring
 2538 plane, *J. Geophys. Res.* *87*, 6045, 1983.
 2539 Northrop, T. G., *The Adiabatic Motion of Charged Particles*, Wiley Interscience, New
 2540 York, 1963.
 2541 Nosé, M., et al., Acceleration of oxygen ions of ionospheric origin in the near-
 2542 Earth magnetotail during substorms, *J. Geophys. Res.*, *105*, 7669, 2000.
 2543 Nykyri, K., et al., Cluster observations of reconnection due to the Kelvin-Helmholtz
 2544 instability at the dawnside magnetospheric flank, *Ann. Geophys.*, *24*, 2619, 2006.
 2545 Nykyri, K., and A. Otto, Plasma transport at the magnetospheric boundary due
 2546 to reconnection in Kelvin–Helmholtz vortices, *Geophys. Res. Lett.*, *28*(18), 3565,
 2547 doi:10.1029/2001GL013239, 2001.
 2548 Ogawa, Y., K. Seki, M. Hirahara, et al., Coordinated EISCAT Svalbard radar and
 2549 Reimei satellite observations of ion upflows and suprathermal ions, *J. Geophys. Res.*,
 2550 *113*, A05306, doi:10.1029/2007JA012791, 2008.
 2551 Ogino, T. R., R. J. Walker, and M. G. Kivelson, A global magnetohydrodynamic
 2552 simulation of the Jovian magnetosphere, *J. Geophys. Res.*, *84*, 47, 1998.
 2553 Øieroset, M., et al., A statistical study of ion beams and conics from the dayside
 2554 ionosphere during different phases of a substorm, *J. Geophys. Res.*, *104*, 6987, 1999.
 2555 Ono, Y., M., et al., The role of magnetic field fluctuations in nonadiabatic acceleration of
 2556 ions during dipolarization, *J. Geophys. Res.*, *114*, doi:10.1029/2008JA013918, 2009.

2557 Orsini, S., and A. Milillo, Magnetospheric Plasma Loss Processes and Energetic Neutral
 2558 Atoms, *Il Nuovo Cimento*, 22 C, N 5, 633, 1999.
 2559 Pallier, L., and R. Prangé, Detection of the southern counterpart of the north FUV polar
 2560 cusp. Shared properties, *Geophys. Res. Lett.*, 31, L06701, 2004.
 2561 Paranicas, C., et al., The ion environment near Europa and its role in surface energetics,
 2562 *Geophys. Res. Lett.* 29 (5), 1074 doi:10.1029/2001GL014127, 2002.
 2563 Parker, E. N., Dynamics of the interplanetary magnetic field, *Astrophys. J.*, 128, 664,
 2564 1958.
 2565 Paschmann G. S., Recent in-situ observations of magnetic reconnection in near-Earth
 2566 space, *Geophys. Res. Lett.*, 35, L19109, doi:10.1029/2008GL035297, 2008.
 2567 Paschmann G., S. Haaland, and R. Treumann, Eds *Auroral plasma physics*, Kluwer
 2568 Academic Publishers, 2003.
 2569 Paschmann, G., M. Øieroset and T. Phan, In-situ observations of reconnection in space,
 2570 *Space Sci. Rev.*, 178, 385-417, doi:10.1007/s11214-012-9957-2, 2013.
 2571 Pellinen, R. J., and W. J. Heikkila, Energization of charged particles to high energies by
 2572 an induced substorm electric field within the magnetotail, *J. Geophys. Res.*, 83, 1544,
 2573 1978.
 2574 Peymirat C. and D. Fontaine, Numerical simulation of the magnetospheric convection
 2575 including the effect of field-aligned currents and electron precipitation, *J.*
 2576 *Geophys. Res.*, 99, 11155, 1994.
 2577 Plainaki, C., et al., Exospheric O₂ densities at Europa during different orbital phases,
 2578 *Planet. Space Sci.*, 88, 42, 2013.
 2579 Plainaki, C., et al., Neutral particle release from Europa's surface. *Icarus* 210, 385, 2010.
 2580 Plainaki, C., et al., The role of sputtering and radiolysis in the generation of Europa
 2581 exosphere. *Icarus* 218 (2), 956, doi.org/10.1016/j.icarus.2012.01.023, 2012.
 2582 Pontius, D. H., Coriolis influences on the interchange instability, *Geophys. Res. Lett.*, 24,
 2583 2961, 1997.
 2584 Potter, A.E., Chemical sputtering could produce sodium vapour and ice on Mercury,
 2585 *Geophys. Res. Lett.* 22 (23), 3289, 1995.
 2586 Powell, K. G., et al., A Solution-Adaptive Upwind Scheme for Ideal
 2587 Magnetohydrodynamics, *J. Comp. Phys.*, 154 (2), 284, doi:10.1006/jcph.1999.6299,
 2588 1999.
 2589 Prangé, R., et al., Rapid energy dissipation and variability of the Io-Jupiter
 2590 electrodynamic circuit, *Nature*, 379, 323, 1996.
 2591 Prangé, R., et al., Detailed study of FUV Jovian auroral features with the post COSTAR
 2592 Hubble Faint Object Camera, *J. Geophys. Res.*, 103, 20195, 1998.
 2593 Prangé, R., The UV and IR Jovian aurorae, *Adv. Space Res.*, 12(8), 379, 1992.
 2594 Pritchett, P. L., Electron-cyclotron maser instability in relativistic plasmas, *Phys.*
 2595 *Fluids*, 29, 2919, 1986.
 2596 Pryor, W. R., et al., The auroral footprint of Enceladus on Saturn, *Nature*, 472, 331, 2011.
 2597 Raeder, J., D., et al., Open GGCM Simulations for the THEMIS Mission, *Space Sci Rev*,
 2598 141, 535, doi:10.1007/s11214-008-9421-5, 2008.
 2599 Ray, L. C., et al., Current-voltage relation of a centrifugally confined plasma, *J. Geophys.*
 2600 *Res.*, 114, A04214, doi:10.1029/2008JA013969, 2009.
 2601 Reimann, C.T., et al., Ion-induced molecular ejection from D₂O ice. *Surface Science*
 2602 147, 227, 1984.
 2603 Roosendaal, H.E., Hating, R.A., Sanders, J.B. Surface disruption as an observable
 2604 factor in the energy distribution of sputtered particles, *Nucl. Instrum. Methods* 194,
 2605 579, 1982

2606 Roux, A., A., et al., Auroral kilometric radiation sources: in situ and remote sensing
 2607 observations from Viking, *J. Geophys. Res.*, 98, 11657, 1993.
 2608 Russell, C. T., et al., Localized Reconnection in the near Jovian magnetotail, *Science*, 280,
 2609 1061, doi:10.1126/science.280.5366.1061, 1998.
 2610 Sandholt, P. E., et al., Dayside auroral configurations: Responses to southward and
 2611 northward rotations of the interplanetary magnetic field, *J. Geophys. Res.*, 103, 20,
 2612 279, 1998.
 2613 Schunk, R.W. and J. J. Sojka, J.J., Global ionosphere–polar wind system during
 2614 changing magnetic activity. *J. Geophys. Res.* 102, 11625, 1997.
 2615 Schunk, R. W. and A. F. Nagy, *Ionospheres*, 2nd Ed., Cambridge University Press, 2009.
 2616 Schunk, R.W., and A. F. Nagy, Ionospheres of the terrestrial planets, *Rev. Geophys.*, 18,
 2617 813–852, 1980.
 2618 Scurry, L. and C. T. Russell, Proxy studies of energy transfer to the magnetosphere.
 2619 *J. Geophys. Res.* 96, 9541, 1991.
 2620 Sergeev, V. A., et al., Pitch-angle scattering of energetic protons in the magnetotail
 2621 current sheet as the dominant source of their isotropic precipitation into the
 2622 nightside ionosphere, *Planet. Space Sci.*, 31, 1147, 1983.
 2623 Sergeev, V. A., M. Malkov, and K. Mursula, Testing the isotropic boundary algorithm
 2624 to evaluate the magnetic field configuration of the tail, *J. Geophys. Res.*, 98,
 2625 7609, 1993.
 2626 Shabansky, V. P., Some processes in the magnetosphere, *Space Sci. Rev.*, 12, 299, 1971.
 2627 Shematovich, V. I., et al., Surface-bounded atmosphere of Europa. *Icarus* 173, 480, 2005.
 2628 Sigmund, P., Theory of Sputtering. I. Sputtering Yield of Amorphous and Polycrystalline,
 2629 1969.
 2630 Siscoe, G., and L. Christopher, Variations in the solar wind stand-off distance at
 2631 Mercury, *Geophys. Res. Lett.*, 2, 158, 1975.
 2632 Siscoe, G. L., On the equatorial confinement and velocity space distribution of satellite
 2633 ions in Jupiter’s magnetosphere, *J. Geophys. Res.*, 82, 1641, 1977.
 2634 Slavin, J. A., et al., MESSENGER and Mariner 10 flyby observations of magnetotail
 2635 structure and dynamics at Mercury, *J. Geophys. Res.*, 117,
 2636 A01215, doi:10.1029/2011JA016900, 2012a.
 2637 Slavin, J. A., et al., MESSENGER Observations of Flux Transfer Events at Mercury, *J.*
 2638 *Geophys. Res.*, 117, A00M06, doi:10.1029/2012JA017926, 2012b.
 2639 Slavin, J. A., et al., MESSENGER Observations of Mercury’s Dayside Magnetosphere
 2640 Under Extreme Solar Wind Conditions, *J. Geophys. Res.*, 119, 8087–8116, 2014.
 2641 Slavin, J. A., et al., CDAW-8 observations of plasmoid signatures in the geomagnetic tail:
 2642 An assessment, *J. Geophys. Res.*, 94, 15153, 1989.
 2643 Slavin, J. A., et al., Geotail observations of magnetic flux ropes in the plasma sheet, *J.*
 2644 *Geophys. Res.*, 108(A1), 1015, doi:10.1029/2002JA009557, 2003.
 2645 Smyth, W.H. and M. L. Marconi, Europa’s atmosphere, gas tori, and magnetospheric
 2646 implications. *Icarus*, 181, 510, 2006.
 2647 Solomon, S. C., Auroral electron transport using the Monte Carlo method, *Geophys. Res.*
 2648 *Lett.*, 20, 185, 1993.
 2649 Sonnerup, B. U. O., Adiabatic particle orbits in a magnetic null sheet, *J. Geophys. Res.*,
 2650 76, 8211, 1971.
 2651 Sonnerup, B. U. O., The magnetopause reconnection rate, *J. Geophys. Res.*, 79, 1546,
 2652 doi:10.1029/JA079i010p01546, 1974.
 2653 Speiser, T. W., Particle trajectory in model current sheets, 1, Analytical solutions,
 2654 *J. Geophys. Res.*, 70, 4219, 1965.

2655 Strangeway, R. J., et al., Factors controlling ionospheric outflows as observed at
 2656 intermediate altitudes, *J. Geophys. Res.*, *110*, A03221, doi:10.1029/2004JA010829,
 2657 2005.
 2658 Sugiura, M., Hourly values of equatorial Dst for the IGY, *Ann. Int. Geophys. Year*, *35*, 9,
 2659 Pergamon Press, Oxford, 1964.
 2660 Sundberg, T., S. et al., MESSENGER orbital observations of large-amplitude Kelvin-
 2661 Helmholtz waves at Mercury's magnetopause, *J. Geophys. Res.*, *117*, A04216, 2012.
 2662 Szegő, K., et al., Physics of Mass Loaded Plasmas, *Space Sci. Rev.*, *94*, 429, 2000.
 2663 Toth, G., et al., Adaptive numerical algorithms in space weather modeling, *J. Comp.*
 2664 *Phys.*, *231* (3), 870–903, doi:10.1016/j.jcp.2011.02.006, 2012.
 2665 Toth, G., et al., Space Weather Modeling Framework: A new tool for the space science
 2666 community, *J. Geophys. Res.*, *110*, 12,226, doi:10.1029/2005JA011126, 2005.
 2667 Tam, S. W. Y., T. Chang, and V. Pierrard, Kinetic modeling of the polar wind, *J.*
 2668 *Atmos. Sol. Terr. Phys.*, *69*, 1984, 2007.
 2669 Teolis, B.D., R.A.Vidal, J. Shi, Baragiola, R.A. 2005. Mechanisms of O2 sputtering from
 2670 water ice by keV ions. *Phys. Rev. B* *72*, 245422, doi:10.1103/PhysRevB.72.245422,
 2671 2005.
 2672 Terada, N., H. Shinagawa, T. Tanaka, K. Murawski, and K. Terada, A three-dimensional,
 2673 multispecies, comprehensive MHD model of the solar wind interaction with the planet
 2674 Venus, *J. Geophys. Res.*, *114*, A09208, doi:10.1029/2008JA013937, 2009.
 2675 Terasawa, T., et al., Solar wind control of density and temperature in the near-Earth
 2676 plasma sheet: WIND/GEOTAIL collaboration, *Geophys. Res. Lett.*, *24*(8),
 2677 935, doi:10.1029/96GL04018, 1997.
 2678 Thomas, B. T., and E. J. Smith The Parker spiral configuration of the interplanetary
 2679 magnetic field between 1 and 8.5 AU, *J. Geophys. Res.*, *85*, 6861, 1980.
 2680 Thomas, N., F. Bagenal, T. W. Hill and J. K. Wilson, The Io neutral cloud and plasma
 2681 torus, in *Jupiter : The Planet, Satellites, and Magnetosphere*, F. Bagenal et al. eds.,
 2682 Cambridge Univ. Press, Chapter 23, 560, 2004.
 2683 Thorne, R. M., et al., Galileo evidence for rapid interchange transport in the Io torus.
 2684 *Geophys. Res. Lett.*, *24*, 2131, 1997.
 2685 Treumann, R.A., The electron-cyclotron maser for astrophysical application,
 2686 *Astron. Astrophys. Rev.*, *13*, 229, 2006.
 2687 Thomsen, M. F., et al., Survey of ion plasma parameters in Saturn's magnetosphere, *J.*
 2688 *Geophys. Res.*, *115*, A10220, doi:10.1029/2010JA015267, 2010.
 2689 Vasyliunas V., Mathematical models of magnetospheric convection and its coupling to
 2690 the ionosphere, in *Particles and Fields in the Magnetosphere*, ed. by B. McCormac,
 2691 Reidel, Hingham, Mass., 1970.
 2692 Vasyliunas, V. M., Plasma distribution and flow, in *Physics of the Jovian*
 2693 *Magnetosphere*, ed. Dessler, A. J., pp. 395, Cambridge Univ. Press, Cambridge
 2694 and New York, 1983.
 2695 Vogt, M. F., et al., Reconnection and flows in the Jovian magnetotail as inferred from
 2696 magnetometer observations, *J. Geophys. Res.*, *115*, A06219,
 2697 doi:10.1029/2009JA015098, 2010.
 2698 Vogt, M. F., et al., Structure and statistical properties of plasmoids in Jupiter's
 2699 magnetotail, *J. Geophys. Res.*, *119*, 821, doi:10.1002/2013JA019393, 2014.
 2700 Waite, J. H., et al. An auroral flare at Jupiter, *Nature*, *410*, 787, 2001.
 2701 Wanliss, J. A., and K. M. Showalter, High-resolution global storm index: Dst versus
 2702 SYM-H, *J. Geophys. Res.*, *111*, A2, A02202, DOI:10.1029/2005JA011034, 2006.

- Westley, M.S., et al., Photodesorption from low-temperature water ice in interstellar and circumstellar grains. *Nature* 373, 405, 1995.
- Williams, D. J., Ring current composition and sources: An update, *Planet. Space Sci.*, 29, 1195, 1981.
- Wilosn, R. J., R. L. Tokar and M. G. Henderson, Thermal ion flow in Saturn's inner magnetosphere measured by the Cassini plasma spectrometer: A signature of the Enceladus torus? *Geophys. Res. Lett.* 36, L23104, doi:10.1029/2009GRL040225, 2009.
- Wiltberger, M., et al., Influence of cusp O⁺ outflow on magnetotail dynamics in a multifluid MHD model of the magnetosphere, *J. Geophys. Res.*, 115, A00J05, doi:10.1029/2010JA015579, 2010.
- Wing, S., and P. T. Newell, 2D plasma sheet ion density and temperature profiles for northward and southward IMF, *Geophys. Res. Lett.*, 29(9), 1307, doi:10.1029/2001GL013950, 2002.
- Winglee, R. M., et al., Global impact of ionospheric outflows on the dynamics of the magnetosphere and cross-polar cap potential, *J. Geophys. Res.*, 107, 1237, doi:10.1029/2001JA000214, 2002.
- Winske, D., L. Yin, N. Omid, H. Karimabadi, K. Quest, Hybrid simulation codes: Past, present and future – A tutorial. Space Plasma Simulation. Edited by J. Büchner, C. Dum, M. Scholer. Lect. Notes Phys. 615, 136165, 2003.
- Wolf R. A., Ionosphere-magnetosphere coupling, *Space Sci. Rev.*, 17, 535, 1979.
- Wu, C. S., and L. C. Lee, A theory of the terrestrial kilometric radiation, *Astrophys. J.*, 230, 621, 1979.
- Wu, X.-Y., J. L. Horwitz, and J.-N. Tu, Dynamic fluid kinetic (DyFK) simulation of auroral ion transport: Synergistic effects of parallel potentials, transverse ion heating, and soft electron precipitation, *J. Geophys. Res.*, 107(A10), 1283, doi:10.1029/2000JA000190, 2002.
- Wurz, P., et al., Self-consistent modelling of Mercury's exosphere by sputtering, micro-meteorite impact and photon-stimulated desorption, *Planet. Space Science*, 58, 1599, 2010.
- Wurz, P., et al., The Lunar Exosphere: The Sputtering Contribution, *Icarus* 191, 486-496, DOI:10.1016/j.icarus.2007.04.034, 2007.
- Yakshinskiy B.V. and T.E. Madey, Temperature-dependent DIET of alkalis from SiO₂ films: Comparison with a lunar sample, *Surf. Science*, 593, 202, 2005.
- Yakshinskiy, B.V. and Madey, T.E., Electron- and photon-stimulated desorption of K from ice surfaces, *J. Geophys. Res.* 106, 33303, 2001.
- Yakshinskiy, B.V., and Madey, T.E., Photon-stimulated desorption as a substantial source of sodium in the lunar atmosphere, *Nature*, 400, 642, 1999.
- Yau, A. W., and M. Andre, Sources of ion outflow in the high latitude ionosphere, *Space Sci. Rev.*, 80, 1, doi:10.1023/A:1004947203046, 1997.
- Yau, A. W., T. Abe, and W. K. Peterson, The polar wind: Recent observations, *J. Atmos. Sol. Terr. Phys.*, 69, 1936, 2007.
- Yee, K. S., Numerical solution of initial boundary value problems involving Maxwell's equations in isotropic media, *IEEE Trans. Antenn. Propagat.*, 14, 302, 1966.
- Yu, Y., and A. J. Ridley, Exploring the influence of ionospheric O⁺ outflow on magnetospheric dynamics: dependence on the source location, *J. Geophys. Res.*, 118, 1711, doi:10.1029/2012JA018411, 2013.
- Zarka, P., Auroral radio emissions at the outer planets : observations and theories, *J.*

2751 *Geophys. Res.*, 103, 20159, 1998.
2752 Ziegler, J.F., Biersack, and J.P, Littmark, U., The Stopping and Range of Ions in Solids,
2753 vol. 1 of series *Stopping and Ranges of Ions in Matter*, Pergamon Press, New York,
2754 1984.
2755 Ziegler, J.F., SRIM-2003, *Nucl. Instr. Meth. B* 219, 1027, 2004.
2756
2757

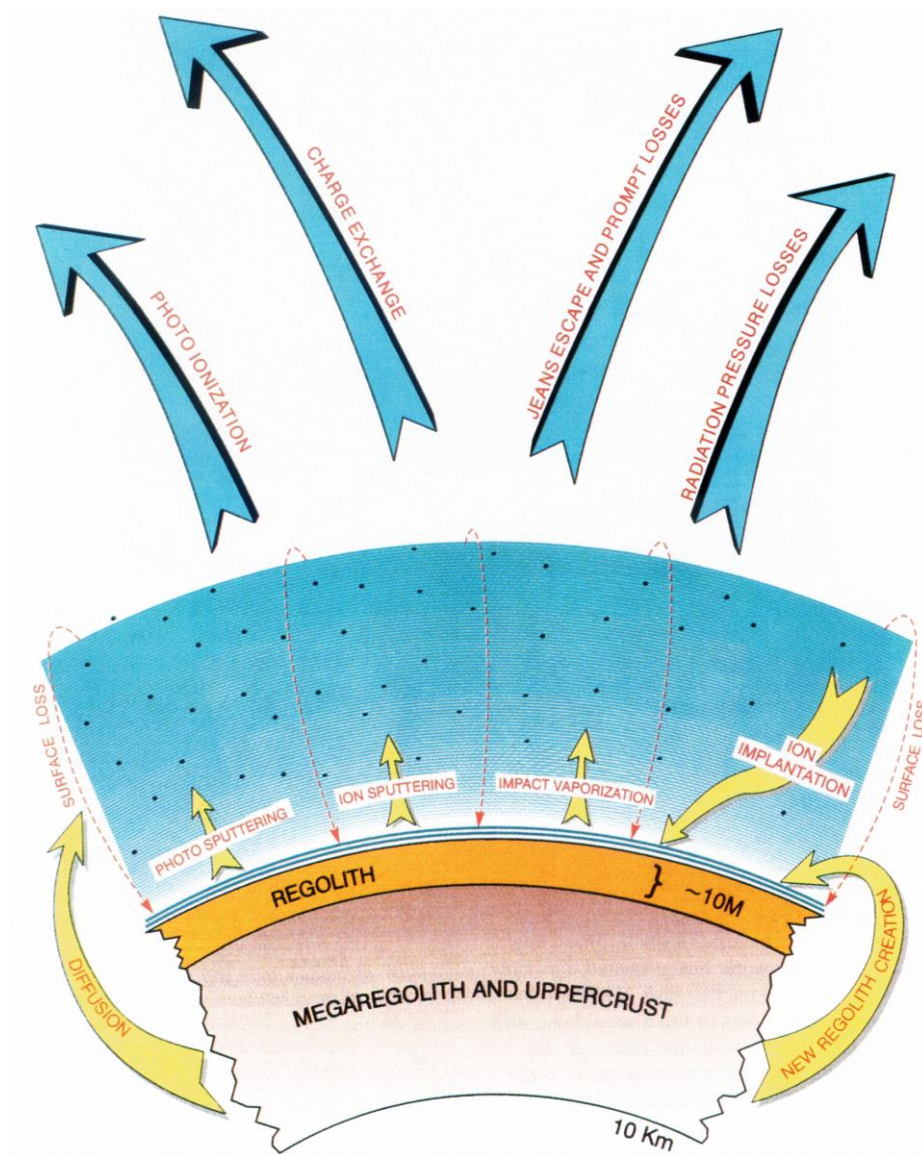


Figure 1: A schematic illustration of the surface sources and sinks for the exosphere (from Killen and Ip, 1999).

2759
2760
2761

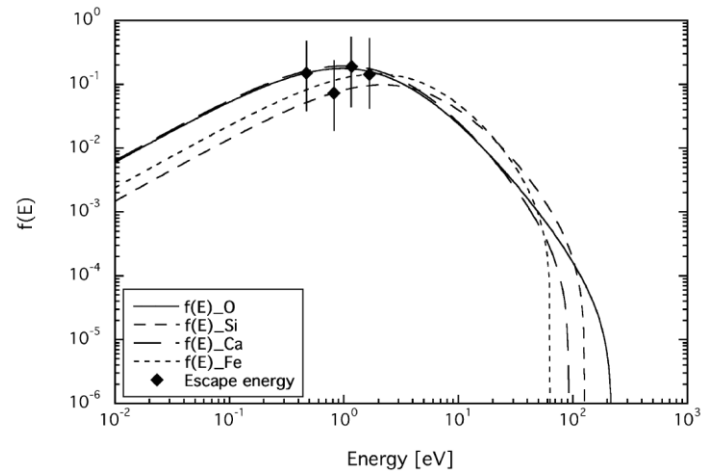


Figure 2: Energy distribution for sputtered O, Si, Ca, and Fe atoms according to Equation (1) using incident protons of 1 keV energy (from Wurz et al., 2007).

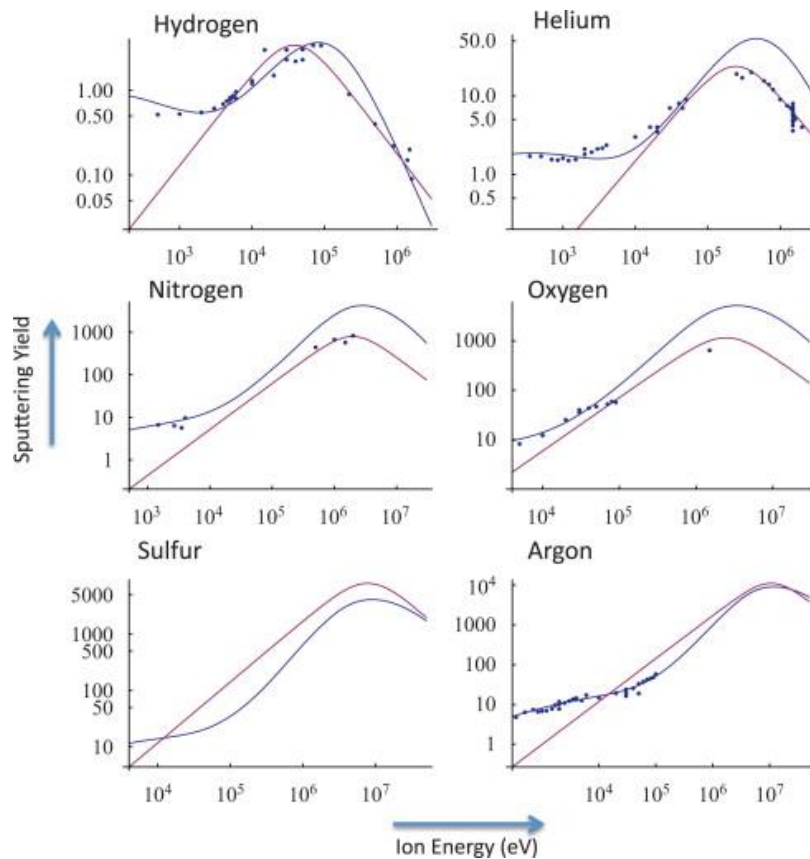


Figure 3: Yields for the released molecules as a function of energy and impact ion species. Empirical derived functions by Famà et al. (2008) (blue) / by Johnson et al. (2009) (red) reproduce low/high energies (Cassidy et al., 2013).

2764

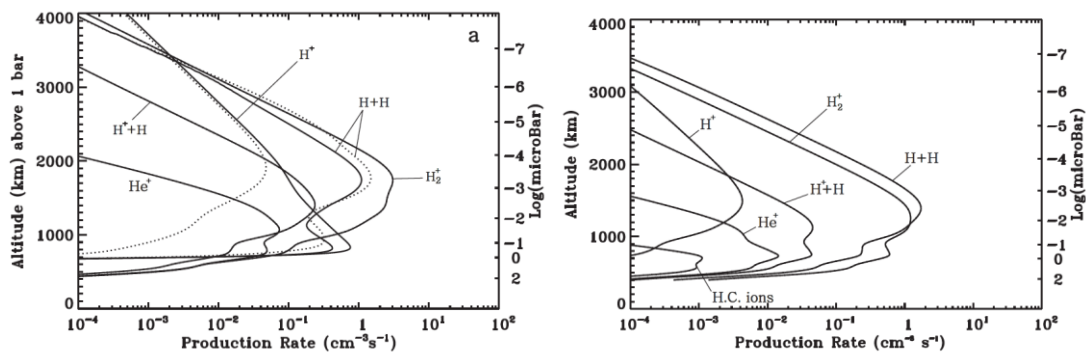


Figure 4: Calculated production rates for Saturn for a solar zenith angle of 27°. Panel a shows the direct photo-production rates and b shows the secondary production rates by the resulting photoelectrons. Note that the electron impact ionization rates are very significant at the lower altitudes. (from *Kim et al.*, 2014)

2765

2766

2767

2768

2769

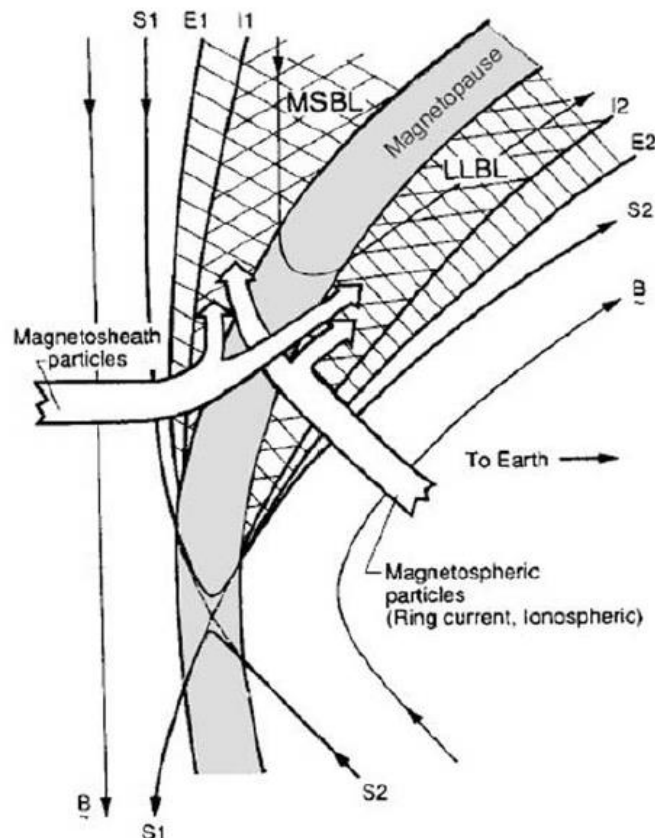


Figure 5. Reconnection geometry for Earth from Gosling et al. (1990). The left-hand side shows a southward magnetosheath field and the right-hand side the northward magnetospheric field. The current layer is shown as the shaded boundary in the center of these two regions. As the fields reconnect (where the two separatrices, S1 and S2 cross) and thread the magnetopause, a region of “open” field allows the entry of magnetosheath particles into the magnetosphere. Additionally, a portion of the population is reflected. Both populations are energized by the process of interacting with the current sheet. On the right the magnetospheric counterpart is transmitted through the boundary and a population is again reflected, again both are energized. As the reconnection continues the fields convect away from the site (up and down in this figure), carrying the plasma with them. Owing to the velocity filter effect a layer of electrons is seen further away from the magnetopause on both sides (between E1 and I1 and I2 and E2). Once the ions “catch up,” a layer of both electrons and ions is then seen (within I1 and I2). (Caption from McAndrews et al., 2008)

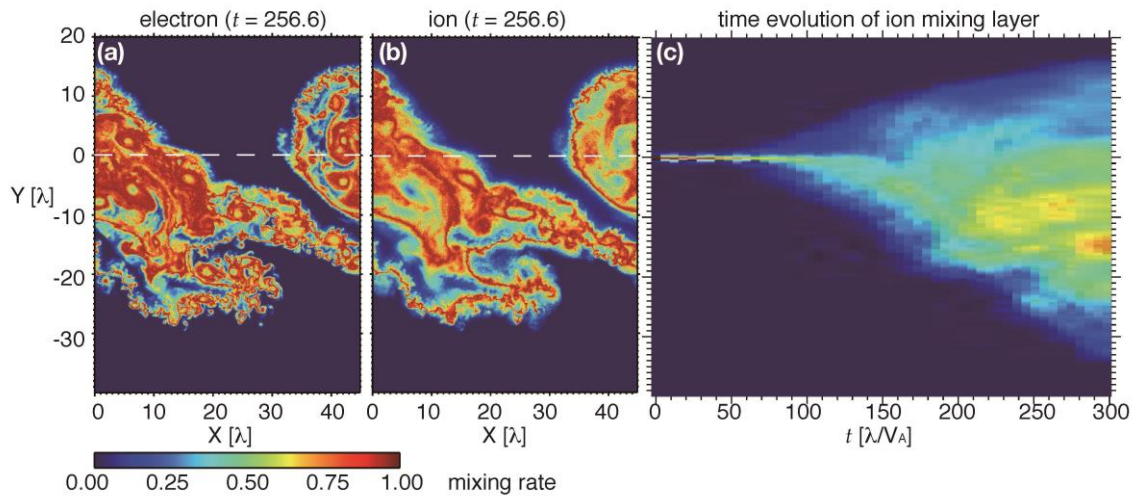


Figure 6. An example of PIC (particle in cell) simulations of KHI for inhomogeneous density case with the density ratio of 0.1. The initial velocity shear layer was located at $Y=0$, whose width was set to λ . Color codes show the mixing rate of magnetosheath particles. The mixing rate is defined so that it is maximized ($=1$) when the magnetosheath-origin particles from $Y > 0$ at $t=0$ occupy the simulation cell equally with the magnetospheric population from $Y \leq 0$. Snapshots of spatial distribution of the mixing rate at $t=256.6$ for electrons and ions are shown in panels (a) and (b), respectively. Panel (c) presents the time evolution of the mixing layer. (Adopted and modified from Matsumoto and Seki, 2010.)

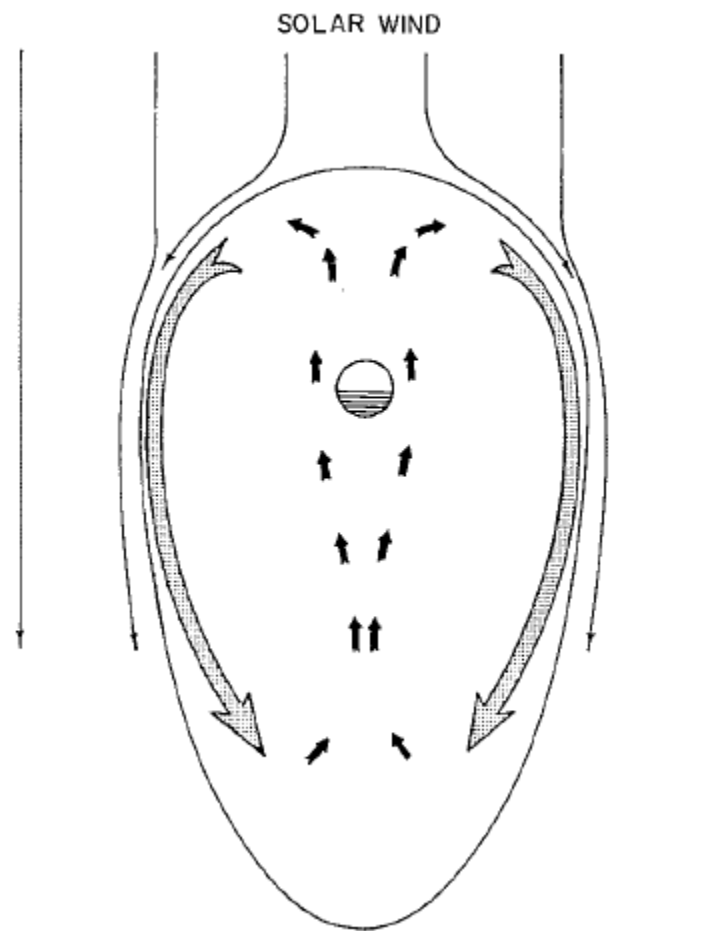


Figure 7. Schematic of the viscous cycle (From Axford and Hines, 1961). This is a view down on to the equatorial plane with the solar wind blowing from top to bottom of the diagram.

2793

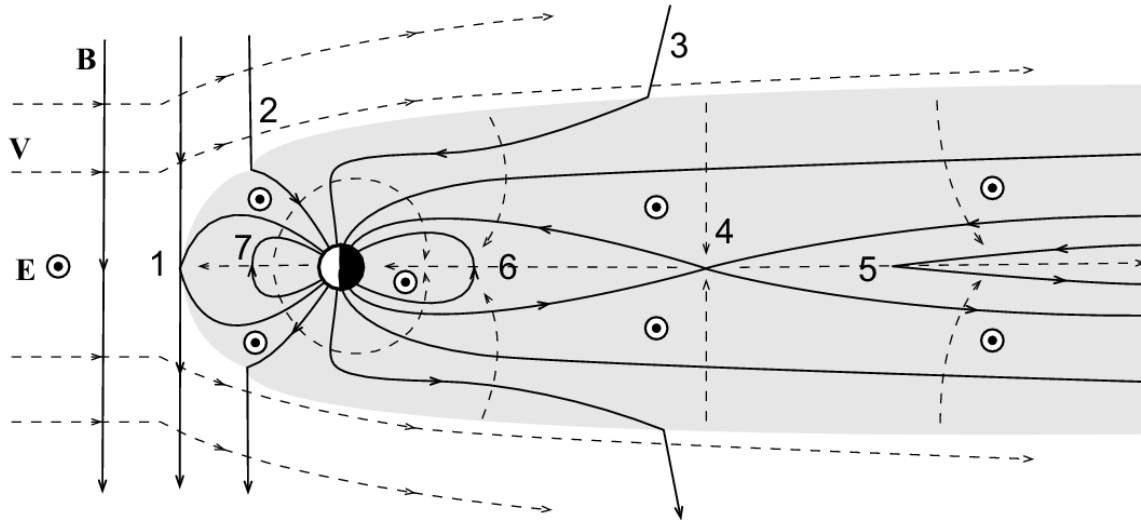


Figure 8. Schematic diagram showing the stages of the Dungey cycle for the case of Earth's magnetosphere (courtesy Steve Milan).

2794

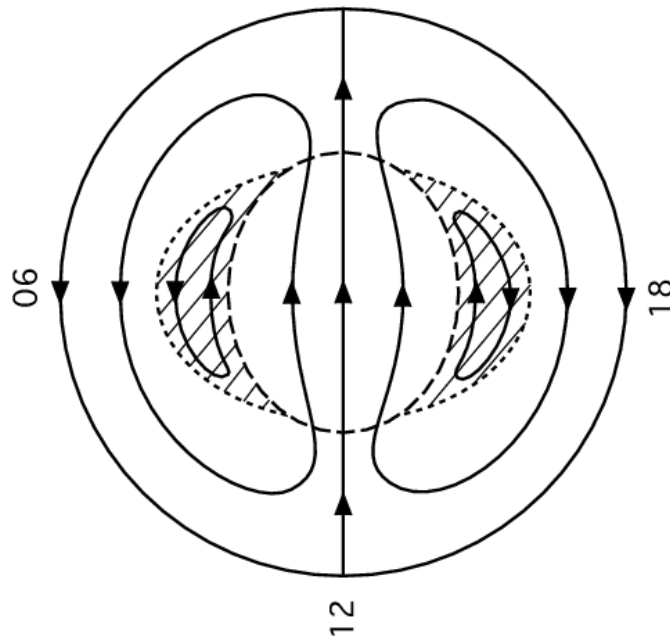


Figure 9. Northern high-latitude ionospheric flow associated with a combination of Dungey and viscous cycle (after Cowley, 1982). The hatched region indicates convection driven by the boundary layers in which magnetic flux tubes remain closed during the cycle, while the remainder of the flow is associated with the reconnection process.

2795

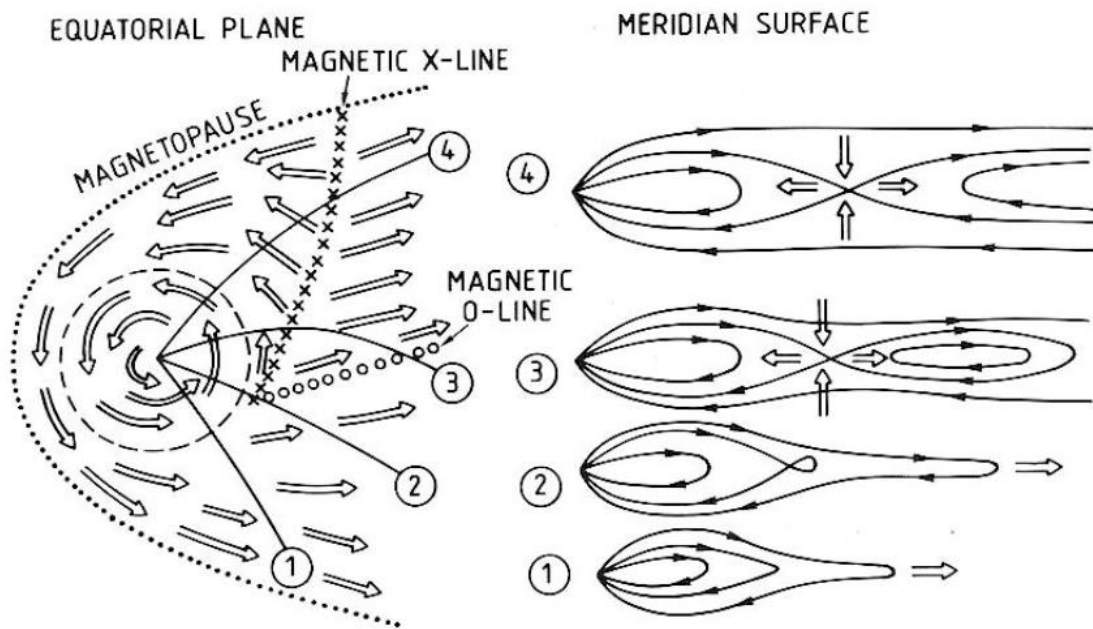


Figure 10. Flow pattern (left) and field configuration (right) expected for a steady-state planetary wind, first proposed for Jupiter by Vasyliunas (1983).

2796

2797

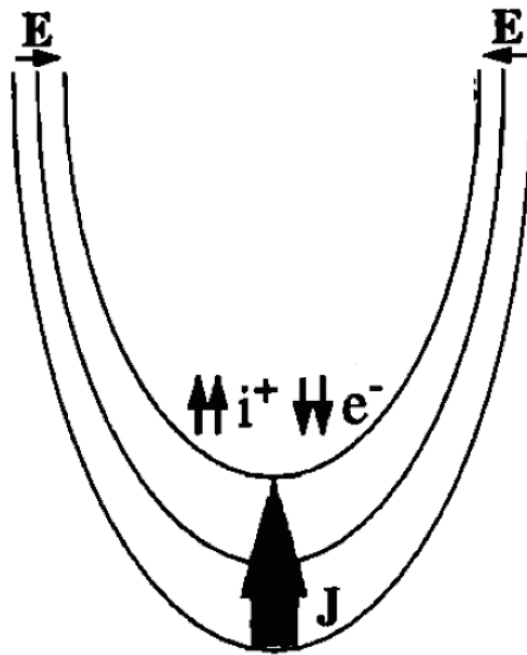


Figure 11. A schematic illustration of the upward current region adapted from Carlson (1998).

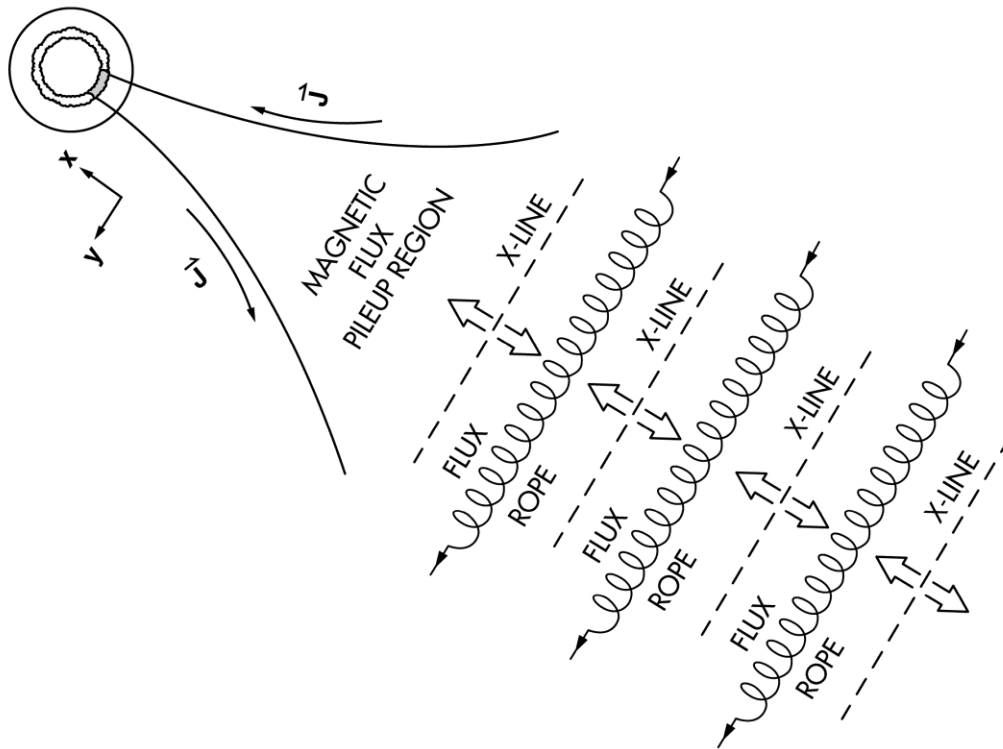


Figure 12. A schematic diagram of the formation of earthward and tailward moving plasmoids following reconnection; after Slavin et al. (2003).

2799
2800

2801

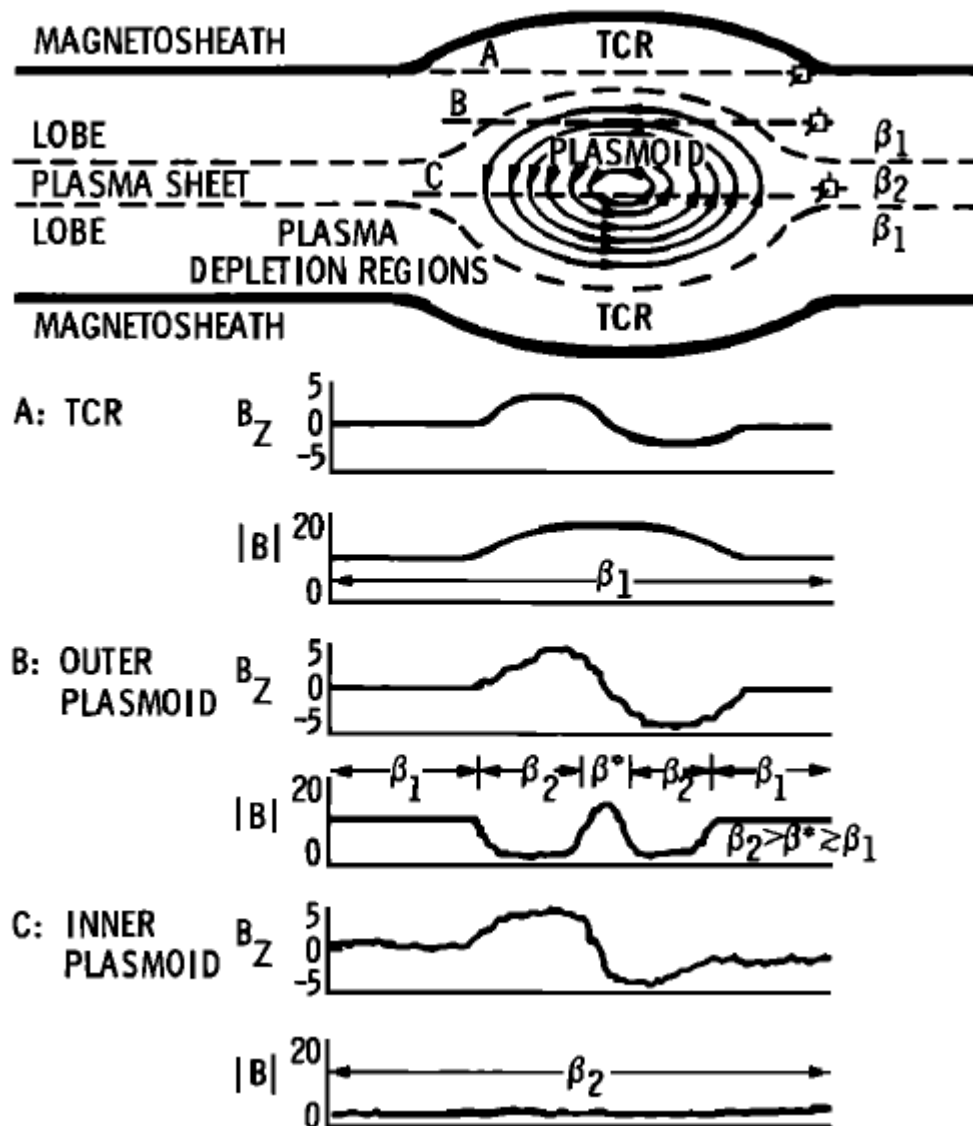


Figure 13. Schematic illustration showing the magnetic field signatures that would arise following a spacecraft track through and near an idealised plasmoid. After Slavin et al. (1989).

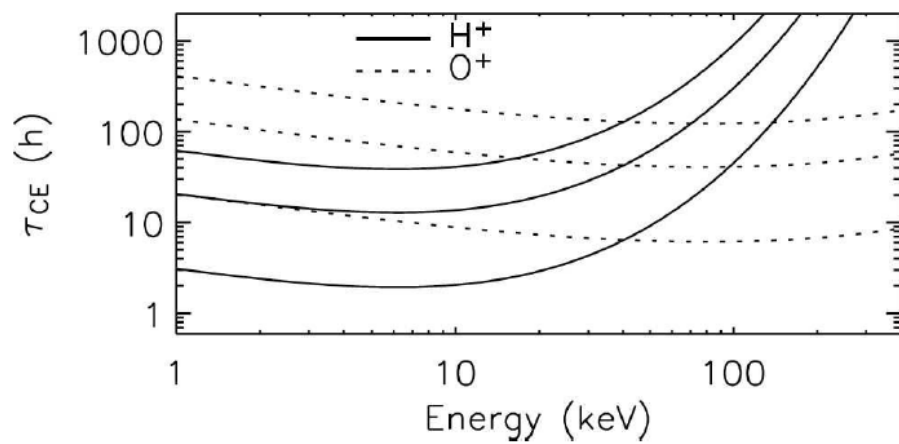


Figure 14. The mean lifetime for charge exchange decay as a function of energy for O^+ and H^+ species. Figure adopted from Liemohn and Kozyra (2005).

2803

2804

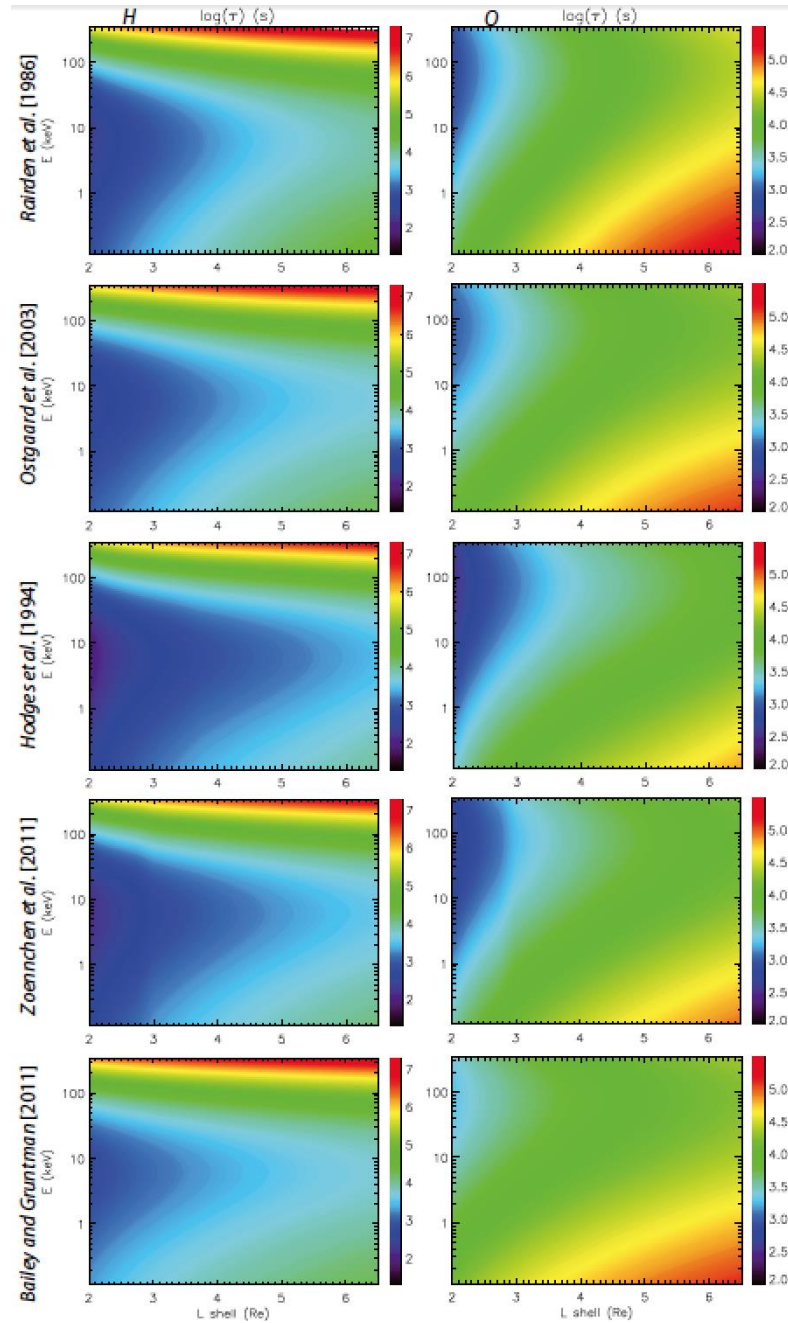


Figure 15. Color contours of lifetimes of H^+ (left column) and O^+ (right column) as a function of energy and radial distance from the Earth. From top to bottom are shown the lifetime predictions from Rairden et al. (1986) , Østgaard et al. (2003) , Hodges (1994), Zoenchen et al. (2011) and Bailey and Gruntman (2011). The color scale is logarithmic and lifetimes are in seconds. Figure from Ilie et al. (2013).

2807
2808
2809

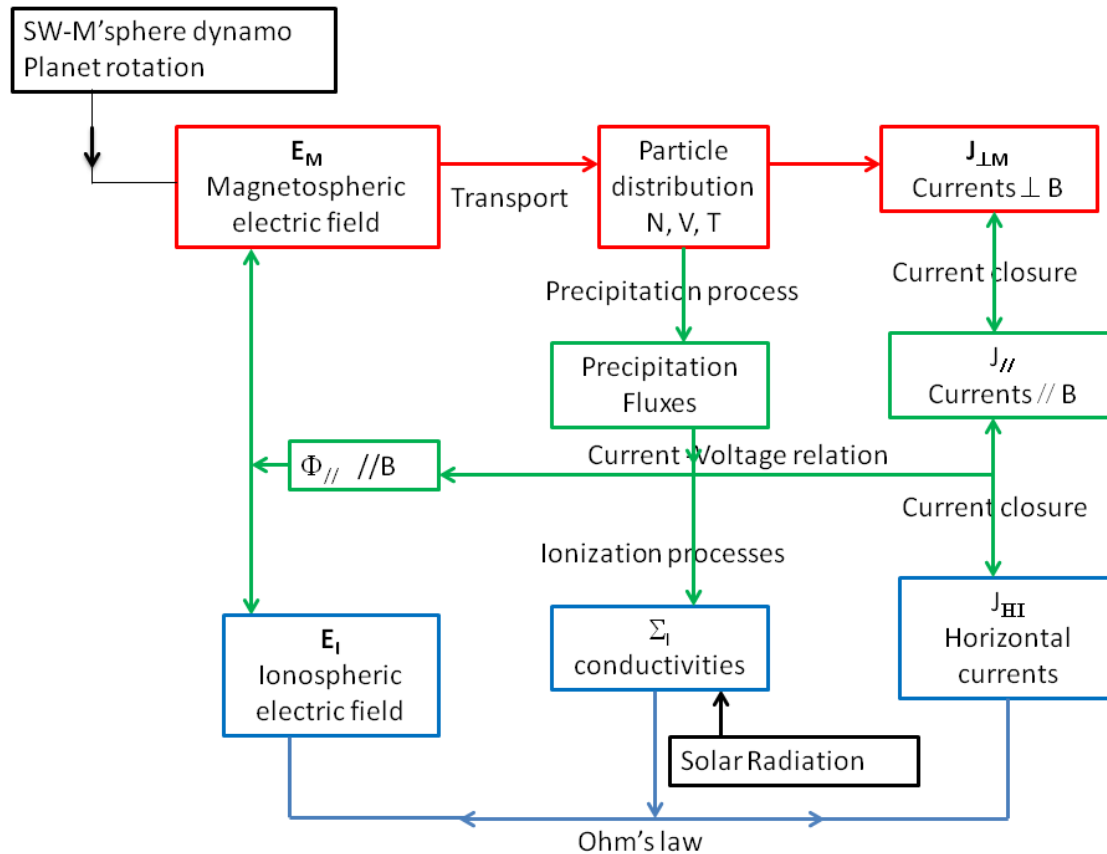


Figure 16. Feedback loop illustrating the ionosphere-magnetosphere coupling with magnetospheric (red), ionospheric (blue) and field-aligned (green) electrodynamic parameters and processes. Black rectangles represent external sources.